

KATHMANDU UNIVERSITY
SCHOOL OF ENGINEERING
DEPARTMENT OF GEOMATICS ENGINEERING



A PROJECT REPORT ON
**INUNDATION MODELLING AND FLOOD HAZARD MAPPING: A CASE
STUDY OF BAGMATI-NAKKHU CONFLUENCE**

In Partial Fulfilment of the Requirements for the Bachelor's Degree in Geomatics Engineering

Prepared By:

Pragyan Baral (027987-20)
Abhinav Chand (027995-20)
Shisir Kharel (028007-20)
Rishav Khatiwada (028009-20)
Saurav Nepal (028016-20)

Supervisors:

Prof. Dr-Ing Ramesh Kumar Maskey
Associate Prof. Dr. Reshma Shrestha

May 2025

KATHMANDU UNIVERSITY
SCHOOL OF ENGINEERING
DEPARTMENT OF GEOMATICS ENGINEERING



A PROJECT REPORT ON
**INUNDATION MODELLING AND FLOOD HAZARD MAPPING: A CASE
STUDY OF BAGMATI-NAKKHU CONFLUENCE**

In Partial Fulfilment of the Requirements for the Bachelor's Degree in Geomatics Engineering

Prepared By:

Pragyan Baral (027987-20)
Abhinav Chand (027995-20)
Shisir Kharel (028007-20)
Rishav Khatiwada (028009-20)
Saurav Nepal (028016-20)

Supervisors:

Prof. Dr-Ing Ramesh Kumar Maskey
Associate Prof. Dr. Reshma Shrestha
Er. Narayan Thapa (Advisor)

May 2025

AUTHORIZATION

We, hereby declare that Pragyan Baral, Abhinav Chand, Shisir Kharel, Rishav Khatiwada, and Saurav Nepal are the authors of this project. We authorize Kathmandu University to lend this project report to other institutions or individuals for scholarly research. We further authorize Kathmandu University to reproduce this project report by photocopying or by other means, in total or in part, at the request of other institutions or individuals for scholarly research.

Pragyan Baral (027987-20)

Abhinav Chand (027995-20)

Shisir Kharel (028007-20)

Rishav Khatiwada (028009-20)

Saurav Nepal (028016-20)

May 2025

PROJECT EVALUATION

INUNDATION MODELLING AND FLOOD HAZARD MAPPING: A CASE STUDY OF BAGMATI-NAKKHU CONFLUENCE

By: Pragyan Baral, Abhinav Chand, Shisir Kharel, Rishav Khatiwada, Saurav Nepal

This is to certify that I have examined the above project and have found that it is complete and satisfactory in all respects, and that any revisions required by the thesis examination committee have been made.

Prof. Dr.-Ing. Ramesh Kumar Maskey
Supervisor

Associate Prof. Dr. Reshma Shrestha
Supervisor

External Examiner
Til Prasad Pangali Sharma, Ph.D
Faculty Member, Nepal Open University

Associate Prof. Dr. Reshma Shrestha
Head of Department
Department of Geomatics Engineering

Date: May 25, 2025

ACKNOWLEDGEMENT

We would like to express our heartfelt gratitude to everyone who supported us in completing this project, *Inundation Modelling and Flood Hazard Mapping: A Case Study of Bagmati-Nakkhu Confluence*.

First of all, we are deeply thankful to our supervisors, **Dr. Ramesh Kumar Maskey** and **Dr. Reshma Shrestha**, for their continuous guidance, encouragement, and insightful feedback throughout the entire process. Their support helped us stay focused and motivated, and their experience was invaluable in shaping the outcome of our study.

We would also like to sincerely thank our advisors, **Mr. Narayan Thapa** from ICIMOD and **Mr. Sujan Subedi** from the Department of Geomatics Engineering, for their technical guidance and helpful suggestions. Their advice and support gave us clarity at important stages of our work.

We are truly grateful to all the faculty members of the **Department of Geomatics Engineering** for sharing their knowledge, offering helpful feedback, and always being ready to assist us whenever we faced challenges.

A special thank you goes to **Er. Yogesh Regmi** from **APAC Geospatial** for kindly providing access to licensed ENVI software and for helping us with the technical aspects of remote sensing analysis. Also, **ESRI India** for ArcGIS Pro Licensing. We also appreciate **Er. Ashok Thakulla**, an alumnus of Kathmandu University and drone pilot at Geo 3D Modelling, for assisting us with drone flights and processing. We are also thankful to **Mr. Hasta Raj Pandey**, Surveyor at Geo3D Modelling, for his continuous technical support and assistance with equipment during fieldwork.

We sincerely acknowledge the Technical Team from **Antariksha Pratisthan Nepal**, especially **Mr. Alison Shilpkar** and his team, for providing us with valuable training on HEC-RAS and HEC-HMS. Their guidance played an important role in our hydrological and hydraulic modelling efforts. We would also like to thank **Er. Deepa Neupane**, Environmental Engineer, for her technical assistance in part of this study.

We would like to thank the **Nepal Police, Jawlakhel**, and the **District Administration Office, Lalitpur**, for granting us the necessary permissions and ensuring a smooth and safe drone operation during our data collection phase.

Finally, we express our sincere appreciation to everyone who contributed to this project in any way, from the local communities to technical experts and friends. Your support, directly or indirectly, made this project possible, and we are genuinely thankful for your help.

Thank you all.

EXECUTIVE SUMMARY

In the final week of September 2024, severe flooding in the Bagmati-Nakkhu confluence area of the Kathmandu Valley caused significant disruption to daily life. Within 24 hours, rainfall ranging from 240 to 322.2 millimetres raised the water levels of the Bagmati and Nakkhu rivers above danger levels, resulting in severe flooding in the southern parts of Kathmandu. The flood led to substantial loss of life and property across the Valley, with thousands of people needing rescue and hundreds of homes being damaged.

This devastating event highlighted the urgent need to improve flood risk assessment in the Kathmandu Valley. In response, our academic project employed modern technologies to develop high-resolution flood hazard maps for the Bagmati-Nakkhu confluence area.

We used drones to capture detailed imagery of the area and generated a Digital Elevation Model (DEM) with a precision of 0.5 meters. This allowed us to identify land elevation changes, drainage paths, and potential water accumulation zones. We then simulated flood behaviour under various rainfall scenarios using the HEC-HMS and HEC-RAS models. These simulations were verified using satellite imagery and field data from the September 27, 2024 flood event.

The final flood maps show water depth, flow direction, velocity, and areas of high flood risk. They also reveal hydraulic behaviours such as water accumulation at river confluences, which can increase flood risk not only at the confluence point but also in surrounding areas.

This project effectively translates complex scientific data into practical, usable information. These maps provide clear insights into flood risks, supporting safer construction, more effective drainage design, and improved emergency preparedness. They also help communities understand the risks in their surroundings and take early action to stay safe.

In the context of climate change and rapid urbanisation, such technology-driven flood assessment tools are not optional they are essential. This project contributes to the development of a safer and more resilient urban future in the Kathmandu Valley.

कार्यकारी सारांश

२०२४ सेप्टेम्बरको अन्तिम साता, काठमाडौं उपत्यकाको बागमती-नखबु संगम क्षेत्रमा आएको भीषण बाढीले जनजीवनमा गम्भीर असर पुऱ्यायो। २४ घण्टामा २४० देखि ३२२.२ मिलिमिटर वर्षा भएपछि बागमती र नखबु खोलामा पानीको सतह खतराको सीमाभन्दा माथि पुग्यो, जसले काठमाडौंको दक्षिणी भागमा गम्भीर बाढी त्यायो। यस बाढीमा उपत्यकामा जनधनको ठूलो क्षति भयो, हजारौं मानिसहरूलाई उद्धार गर्नुपर्यो, र सयौं घरहरू क्षतिग्रस्त भए।

यस विनाशकारी घटनाले काठमाडौं उपत्यकाको बाढी जोखिम मूल्यांकनमा सुधार आवश्यक रहेको देखायो। यस सन्दर्भमा, हाम्रो शैक्षिक परियोजनाले बागमती-नखबु संगम क्षेत्रको उच्च-रिजोल्युसन बाढी जोखिम नक्सा तयार पार्न आधुनिक प्रविधिहरू प्रयोग गयौं।

हामीले ड्रोनमार्फत क्षेत्रको विस्तृत फोटोहरू संकलन गरी ०.५ मिटर सटीकता सहितको डिजिटल एलिभेसन मोडेल (DEM) निर्माण गयौं। यसले जमिनको उतार-चढाव, जल निकास मार्गहरू, र सम्भावित पानी जम्मे स्थानहरू स्पष्ट रूपमा देखायो। त्यसपछि, HEC-HMS र HEC-RAS मोडेलहरू प्रयोग गरेर विभिन्न वर्षा परिदृश्यहरूमा बाढीको व्यवहारको वैज्ञानिक परिकल्पना (सिमुलेशन) गयौं। यी सिमुलेशनहरूलाई २०२४ सेप्टेम्बर २७ को बाढीका स्याटेलाइट फोटो र फिल्ड डेटा प्रयोग गरेर प्रमाणीकरण गयौं।

अन्तिमका बाढीका नक्साहरूले पानीको गहिराइ, प्रवाह दिशा, वेग, र उच्च जोखिम भएका क्षेत्रहरू देखाउँछन्। यी नक्साहरूले नदी संगमहरूमा पानी जम्मे जस्ता व्यवहारहरू पनि देखाउँछन्, जसले संगम का साथै संगम ओर-परका केही क्षेत्रहरूलाई बढी जोखिममा पार्न सक्ने सम्भावना देखाउँछ।

यो कार्यले जटिल वैज्ञानिक जानकारीलाई उपयोगी र व्यावहारिक रूपमा रूपान्तरण गरेको छ। यी नक्साहरूले बाढी जोखिममा स्पष्ट जानकारी प्रदान गर्छन्, जसले सुरक्षित निर्माण, प्रभावकारी ढल निकास प्रणाली, र आपतकालीन तयारीमा मद्दत पुऱ्याउँछ। यसले समुदाय र सरोकारवाला निकाय हरूलाई वरपरका जोखिमहरू बुझ्न र सुरक्षित रहन प्रारम्भिक कदम चाल्न मद्दत गर्छ।

जलवायु परिवर्तन र तीव्र शहरीकरणको सन्दर्भमा, यस्ता प्रविधिमैत्री बाढी मूल्यांकन उपकरणहरू अब वैकल्पिक होइनन्, आवश्यक छन्। यो परियोजनाले काठमाडौं उपत्यकामा सुरक्षित शहर निर्माणमा योगदान पुऱ्याउनेछ।

ABSTRACT

This study investigates flood hazard dynamics at the confluence of the Bagmati and Nakkhu rivers in the Kathmandu Valley, a region increasingly vulnerable to flooding due to rapid urbanization, unregulated land use changes, and limited hydraulic infrastructure. Despite the growing frequency and severity of urban floods in Nepal, most existing hazard assessments rely on low-resolution data and lack empirical validation, limiting their utility for effective planning and risk mitigation. To address this critical gap, this research develops a high-resolution, field-calibrated flood hazard mapping framework that integrates hydrological modeling (using HEC-HMS), hydraulic simulation (using HEC-RAS), sub-meter UAV-based topographic mapping, satellite-based flood detection, and GIS-based spatial analysis.

Hydrological modeling using HEC-HMS was conducted to estimate peak discharges for the Nakkhu River from 2000 to 2024, which were used to compute design discharges for return periods ranging from 5 to 150 years based on Gumbel distribution. For the Bagmati River, observed peak discharges were used to estimate return period flows accordingly. These discharge estimates were input into HEC-RAS to simulate flood inundation extents and depths. A high-resolution Digital Elevation Model (DEM), with a spatial resolution of 0.5 meters, was generated through UAV photogrammetry to enhance terrain representation and improve hydraulic accuracy. Flood extents from the extreme rainfall event on 27 September 2024 were extracted from Sentinel-2 imagery using supervised classification and used to validate model outputs. The hydraulic model was calibrated and validated using ground-truth field data, including surveyed flood marks and high-water level observations.

Land use and land cover (LULC) data were derived from detailed UAV surveys, enabling spatial analysis of flood impacts across residential, forest, and bare soil zones. Results indicate that although a significant portion of the inundated area falls under the low hazard category, residential areas are consistently exposed to moderate to high hazard levels under longer return period scenarios. The model effectively captures the influence of local topography and hydraulic dynamics in shaping flood behavior. Overall, the study presents a replicable, data-driven methodology that bridges remote sensing, field validation, and hydrologic-hydraulic modeling to support evidence-based flood risk assessment and urban resilience planning in flood-prone urban settings.

TABLE OF CONTENTS

ACKNOWLEDGEMENT	i
EXECUTIVE SUMMARY	ii
कार्यकारी सारांश	iii
ABSTRACT	iv
TABLE OF CONTENTS	v
LIST OF FIGURES	viii
LIST OF TABLES	x
LIST OF ABBREVIATIONS	xi
LIST OF EQUATIONS.....	xii
1 INTRODUCTION	1
1.1 Background	1
1.2 Statement of the problem	4
1.3 Objectives.....	4
1.4 Scope of Work	4
2 LITERATURE REVIEW	5
2.1 Flood Hazard Mapping.....	5
2.2 Hydrologic Engineering Center - River Analysis System (HEC-RAS)	6
2.2.1 Manning's Coefficient (n).....	8
2.2.2 Boundary Condition.....	9
2.2.3 Flood Frequency Analysis.....	10
2.3 Hydrologic Engineering Center - Hydrologic Modeling System (HEC-HMS)	12
2.3.1 Loss Model (SCS Curve Number).....	13
2.3.2 Transform Model (SCS Unit Hydrograph)	14
2.3.3 Routing (Muskingum).....	15
2.3.4 The Nash–Sutcliffe Efficiency (NSE).....	16
2.4 Integration of Hydrologic and Hydraulic Models	16
2.5 Usage of Unmanned Aerial Vehicle (UAV) for DEM Generation	17
2.6 Supervised Classification for Flood Extent Mapping	18
2.6.1 Maximum Likelihood Classification	20
2.7 Calibration of Hydraulic Model Using Field Observation Data	20

2.8	Catchment Area Ratio (CAR) Method	21
2.9	Research Gap and Rationale for Integrated Approach	23
3	METHODOLOGY	25
3.1	Study Area.....	25
3.2	Instrument Used	25
3.3	Softwares Used.....	25
3.4	Data Used	26
3.5	Conceptual Framework	27
3.6	Methodological Workflow	28
3.6.1	Supervised Classification.....	29
3.6.2	DEM and Orthomosaic Generation from UAV Survey	34
3.6.3	Hydrologic Modeling Using HEC-HMS and the Catchment Area Ratio (CAR) Method	39
3.6.4	Hydrologic Modelling Using HEC-RAS	48
3.6.5	Preparation of Hazard Map	60
4	PROJECT MANAGEMENT.....	61
4.1	Gantt Chart	62
5	BUDGET	63
6	RESULTS AND DISCUSSIONS	64
6.1	Flood Inundation Modelling	64
6.1.1	5 Year Return Period	64
6.1.2	10 Years Return Period	66
6.1.3	25 Years Return Period	68
6.1.4	50 Years Return Period	70
6.1.5	100 Years Return Period	72
6.1.6	150 Years Return Period	74
6.1.7	Inundation Map of 27 th September	76
6.1.8	Backwater effect at the Bagmati-Nakkhu Confluence.....	79
6.2	Flood Hazard Mapping.....	85
6.2.1	5 Years Return Period	85
6.2.2	10 Years Return Period	85
6.2.3	25 Years Return Period	86
6.2.4	50 Years Return Period	87

6.2.5	100 Years Return Period	88
6.2.6	150 Years Return Period	89
6.2.7	27 th September Flood Hazard Map	90
6.3	Validation	91
6.3.1	Validation of HEC-RAS Flood Simulation Using Supervised Classification of Sentinel-2 Imagery	91
7	LIMITATIONS AND RECOMMENDATIONS.....	93
7.1	Limitations	93
7.2	Policy Recommendations.....	93
7.3	Future Works	93
8	CONCLUSION	94
9	REFERENCES	95
10	ANNEX.....	107

LIST OF FIGURES

Figure 1: Study Area	25
Figure 2: Conceptual Framework Workflow	27
Figure 3: Methodological Workflow.....	28
Figure 4: Flood Delineation Using Supervised Classification Workflow.....	29
Figure 5: Copernicus Browser	29
Figure 6: Sentinel imagery of Confluence area	30
Figure 7: Flood Delineation and Validation.....	33
Figure 8: Flood Extent Map.....	34
Figure 9: Ortho mosaic of Study Area	36
Figure 10: Point Cloud Classification.....	37
Figure 11: Digital Terrain Model	38
Figure 12: Digital Surface Model	38
Figure 13: Land Cover of Study Area.....	39
Figure 14: Methodological Flowchart for HEC-HMS.....	40
Figure 15: ALOS PALSAR DEM of the Study Area.....	41
Figure 16: Delineated Elements for Nakkhu Breakpoint.....	42
Figure 17: Nash-Sutcliffe Efficiency (Before Calibration).....	44
Figure 18: Nash-Sutcliffe Efficiency (After Calibration)	44
Figure 19: Observed vs Simulated Flow (After Calibration).....	45
Figure 20: Validation on 2020 Observed Data.....	45
Figure 21: Break Points (Bagmati and Nakkhu).....	47
Figure 22: Methodological flowchart for HEC-RAS.....	48
Figure 23: Terrain and River Geometry used for the modelling the flood return periods	52
Figure 24: Assigning steady flow data for each profile (return year)	53
Figure 25: Determining slope using Reaches Profile	54
Figure 26: Input for Reach Boundary Condition	54
Figure 27: Calibrating the extent of September 27, 2024 flood using the surveyed points.....	55
Figure 28: Comparison Between Observed Depth and Simulated Depth.....	58
Figure 29: Comparison between Observed Elevation and Simulated Elevation	58
Figure 30: RMSE for each Manning's Coefficient for range (0.03-0.07) in increasing order	59
Figure 31: Inundation map of 27 th September flood using manning's coefficient (0.03-0.07)....	60
Figure 32: Cross Sections along Nakkhu River.....	64
Figure 33: Inundation map for 5 year return period	65
Figure 34: Cross section of upstream part of Nakkhu for 5 year return period	65
Figure 35: Cross section of mid-nakkhu for 5 year return period.....	66
Figure 36: Cross section around Bagmati-Nakkhu confluence for 5 year return period	66
Figure 37: Inundation map for 10 year return period	67
Figure 38: Cross section of upstream part of Nakkhu for 10 year return period	67
Figure 39: Cross section of mid-nakkhu for 10 year return period.....	68
Figure 40: Cross section around Bagmati-Nakkhu confluence for 10 year return period	68
Figure 41: Inundation map for 25 year return period	69
Figure 42: Cross section of upstream part of Nakkhu for 25 year return period	69

Figure 43: Cross section of mid-nakkhu for 25 year return period.....	70
Figure 44: Cross section around Bagmati-Nakkhu confluence for 25 year return period	70
Figure 45: Inundation map for 50 year return period	71
Figure 46: Cross section of upstream part of Nakkhu for 50 year return period	71
Figure 47: Cross section of mid-nakkhu for 50 year return period.....	72
Figure 48: Cross section around Bagmati-Nakkhu confluence for 50 year return period	72
Figure 49: Inundation map for 100 year return period	73
Figure 50: Cross section of upstream part of Nakkhu for 100 year return period	73
Figure 51: Cross section around Bagmati-Nakkhu confluence for 100 year return period	74
Figure 52: Inundation map for 150 year return period	75
Figure 53: Cross section of upstream part of Nakkhu for 150 year return period	75
Figure 54: Cross section of mid-nakkhu for 150 year return period.....	76
Figure 55: Cross section around Bagmati-Nakkhu confluence for 150 year return period	76
Figure 56: Inundation map of 27th September flood.....	77
Figure 57: Cross section of upstream part of Nakkhu	78
Figure 58: Cross section for mid-nakkhu.....	78
Figure 59: Cross section for Bagmati-Nakkhu Confluence.....	78
Figure 60: Cross section of Bagmati before confluence	79
Figure 61: Cross section of Bagmati after confluence.....	79
Figure 62: Flood Velocity map for 5 year return period	80
Figure 63: Flood Velocity map for 10 year return perio	80
Figure 64: Flood Velocity map for 25 year return period	81
Figure 65: Flood Velocity map for 50 year return period	82
Figure 66: Flood Velocity map for 100 year return period	83
Figure 67: Flood Velocity map for 150 year return period	83
Figure 68: Flood Velocity map for 27 September 2024.....	84
Figure 69: Flood Hazard Map for 5 year return period	85
Figure 70: Flood Hazard Map for 10 year return period	86
Figure 71: Flood Hazard Map for 25 year return period	87
Figure 72: Flood Hazard Map for 50 year return period	88
Figure 73: Flood Hazard Map for 100 year return period	89
Figure 74: Flood Hazard Map for 150 year return period	90
Figure 75: Flood Hazard Map of 27th September	91
Figure 76: Validation Flowchart	91
Figure 77: HEC-RAS Simulation overlayed over Supervised Classification Map	92

LIST OF TABLES

Table 1: Data used and its sources	26
Table 2: Confusion Matrix	31
Table 3: UAV Flight Specification.....	35
Table 4: Geolocation Error Table.....	35
Table 5: Simulated Peak Discharge for Nakkhu Break Point	46
Table 6: Catchment Area for Break Points	47
Table 7:Return Period Discharge of Nakkhu River obtained using Gumbel's Distribution	48
Table 8: Annual Peak Discharge of Khokana Station obtained from DHM	49
Table 9: Return Period Discharge of Khokana River obtained using Gumbel's Distribution.....	50
Table 10: Return Period Discharge before and after Confluence obtained using CAR.....	50
Table 11: Return Period Discharge of all required river for integrating to HEC-RAS.....	51
Table 12: Comparison of depth for different manning's coefficient with the observed depth.....	57
Table 13: Comparison of elevation for different manning's coefficient with the observed elevation.....	57
Table 14: RMSE Value for different Manning's Coefficient.....	59
Table 15: Project Management Table.....	61
Table 16: Project Schedule.....	62
Table 17: Budget Table	63
Table 18: Area Covered by different land cover in 27th september flood.....	90

LIST OF ABBREVIATIONS

Abbreviation	Full Form
ALOS PALSAR	Advanced Land Observing Satellite - Phased Array type L-band Synthetic Aperture Radar
ANN	Artificial Neural Network
APAC	Asia Pacific Academic Consortium
ASF DAAC	Alaska Satellite Facility Distributed Active Archive Center
ASTER	Advanced Spaceborne Thermal Emission and Reflection Radiometer
CAR	Catchment Area Ratio
CN	Curve Number
DEM	Digital Elevation Model
DGPS	Differential Global Positioning System
DHM	Department of Hydrology and Meteorology
DJI	Da-Jiang Innovations
DSM	Digital Surface Model
ENVI	Environment for Visualizing Images
GCP	Ground Control Point
GIS	Geographic Information System
GNSS	Global Navigation Satellite System
HEC-HMS	Hydrologic Engineering Center - Hydrologic Modeling System
HEC-RAS	Hydrologic Engineering Center - River Analysis System
HFL	High Flood Level
HWM	High Water Mark
ICIMOD	International Centre for Integrated Mountain Development
KVW	Kathmandu Valley Watershed
LULC	Land Use and Land Cover
LiDAR	Light Detection and Ranging
ML	Machine Learning
MLC	Maximum Likelihood Classification
NASA POWER	NASA Prediction of Worldwide Energy Resources
NNDRMA	National Disaster Risk Reduction and Management Authority
NDWI	Normalized Difference Water Index
NIR	Near-Infrared
NLCD	National Land Cover Dataset
NSE	Nash–Sutcliffe Efficiency
ROI	Region of Interest
RSR	Root Mean Square Standardized Residual
RTK	Real-Time Kinematic
SAR	Synthetic Aperture Radar
SCS	Soil Conservation Service
SWMM	Storm Water Management Model
TIN	Triangulated Irregular Network
UAV	Unmanned Aerial Vehicle
UN-SPIDER	United Nations Platform for Space-based Information for Disaster Management and Emergency Response

LIST OF EQUATIONS

Equation 1	7
Equation 2	7
Equation 3	10
Equation 4	11
Equation 5	11
Equation 6	11
Equation 7	13
Equation 8	14
Equation 9	14
Equation 10	15
Equation 11	15
Equation 12	20
Equation 13	22

1 INTRODUCTION

1.1 Background

One of the most destructive natural calamities that puts people and property at risk is flooding. The flooding events can be attributed to various factors, including rising urbanization, increased developmental and economic activities in flood plains, and global warming. Recent studies have also demonstrated that widespread human disruption of the natural order, such as deforestation, accelerated river channel sedimentation, encroachment of human settlement along riverbanks, etc., increases the likelihood of flooding (Kumar & Singh, 2021; A. Malik & Abdalla, 2016). In the present time, global warming has led flood to become more severe and unpredictable due to the occurrence of frequent and extreme precipitation, placing millions of people at risk (Thapa et al., 2024). Floods are among the most destructive natural disasters, causing significant loss of life and economic damage. In 2023, around 7,600 people died due to floods, far fewer than the 35,000 deaths recorded in 1999. That same year, over 30 million people were affected globally, through injury, displacement, or other impacts. In 2010, this number reached nearly 200 million. Floods also devastate infrastructure and property, with countries like Bangladesh, Vietnam, and Egypt among the most exposed to river flooding as of 2024 (Salas, 2024).

In Nepal, flood causes huge loss of life and damage in property throughout the monsoon season. Particularly, from June to September, there has been significant devastation due to continuous rainfall causing flood. As per study by UNDP, Nepal is ranked as 30th country with respect to vulnerability of flood (Shreevastav, 2019). In Nepal, flooding mostly occurs in the valleys of the Himalayan Mountains, caused by the erratic monsoon rainfall (Malla et al., 2020). Above-normal rainfall caused 144 floods in 2021, a significant increase over the 91 that were recorded in 2020. The same year, western Nepal saw extreme rains and flooding, destroying thousands of hectares of rice fields and threatening local livelihoods and food security (Gauchan, 2023). In the northeastern regions of Nepal, recent major flooding events in June 2023 resulted in significant loss of life and damage to infrastructure, livelihoods, property, and crops. Over the course of the preceding year, 153 flood and 173 heavy rainfall incidents were recorded nationwide (A. Aryal et al., 2022).

Urban areas are more susceptible to the destructive effects of flooding, especially those situated in flood-prone zones. This issue is particularly pertinent to rapidly urbanizing regions like the Kathmandu Valley Watershed (KVV), where numerous studies have demonstrated that the water balance has been upset by rapid urbanization, leading to increased runoff, increased vulnerability to flood inundation, and decreased groundwater recharge (S. Acharya et al., 2023; Danegulu et al., 2024). Due to impermeable surfaces and urbanization into floodplains, the KVV's water absorption has been hindered, increasing the risk of flooding and causing excessive runoff (Tingsanchali, 2012). According to KC et al. (2021), Due to high population density and widespread development, the Kathmandu Valley has seen numerous flooding disasters that have caused significant damage. Rapid urbanizations and land use and land cover change in the KVV region in recent years might have altered the dynamics of river catchments and floodplains and resulted in extreme flooding in the valley (Lamichhane & Shakya, 2021).

The KVW has experienced several notable flood events over the years. The 1954 flood caused extensive damage to agriculture and infrastructure (Nepal et al., 2018), while the 1981 flood, triggered by intense monsoon rains, exposed the risks of unplanned urban expansion (ICIMOD, 2009). The devastating 1993 flood resulted in over 130 deaths and widespread destruction (Dahal, 2012). In 2002, heavy rainfall and poor drainage led to severe inundation in low-lying areas (MoHA, 2004), and the 2008 flood, though less severe, disrupted communities and highlighted the need for resilient infrastructure (ICIMOD, 2010). The unprecedented rainfall that occurred in central Nepal from September 26 to 28, 2024, set record-breaking 24-hour rainfall totals at 25 weather stations across the country (DHM, 2024). The Kathmandu Valley and adjacent areas suffered greatly as a result of the several landslides and debris flows caused by the 60-hour continuous downpour. The 2024 disaster affected 2.59 million people across 518,403 households, resulting in 250 fatalities, 18 missing persons, and numerous injuries. Economic losses surpassed USD 340.74 million, exceeding 1% of Nepal's GDP, with widespread damage to infrastructures (NDDRMA, 2024).

Flood inundation mapping provides valuable information for decision-makers and authorities to develop flood mitigation strategies and resource allocation (Vashist & Singh, 2023). Urban flooding, which is made worse by urbanization and climate change, is the flooding of urban areas as a result of either insufficient drainage systems, heavy rainfall, or a combination of the two. It poses significant risks to infrastructure, public health, and the environment (Alves et al., 2024). Various hydraulic and hydrologic models are used to simulate the flooding events to support the decision-making process regarding the prediction and prevention of floods. Flood modeling has grown even more important as the risk to life and property has increased. Numerous studies have been carried out for flood modeling that has left significant impacts in a number of areas, including early warning system development, urban flood risk management, vulnerability and flood hazard analysis, and flood risk prediction mapping (N. Dangol, 2021; Shreevastav et al., 2022; Shrestha et al., 2023). Existing researches about flood modelling has primarily focused on two modelling programs for hydrologic and hydraulic modelling. In particular, HEC-HMS or SWAT may be used to perform hydrologic calculations and generate hydrograph that serves as an input for hydraulic modelling in HEC-RAS (Qaiser-Yuan, 2011). Unmanned Aerial Vehicles (UAVs) can be used for obtaining the Digital Elevation Model (DEM) of the study area, which if available in high resolution aids to the accurate flood modelling and inundation mapping (Parizi et al., 2022a; Peker et al., 2024a).

Recent literatures further emphasize that most flood hazard studies in Nepal, including those focusing on the Kathmandu Valley Watershed (KVW), rely heavily on coarse-resolution DEMs and limited empirical calibration, which undermines the precision of flood extent predictions (Adhikari & Panthee, 2020; Upadhyaya et al., 2023). While HEC-RAS and HEC-HMS are widely used modeling platforms, their effectiveness is significantly enhanced when integrated with high-resolution topographic inputs and validated against field data, which are often missing in regional applications. This gap is especially critical in urban environments like KVW, where micro-topographic and land use variations exert substantial influence on flood dynamics.

Systematic flood studies are extremely rare, and only a small number of scientific articles have been published recently, despite the fact that flooding events and their effects in the KV are frequently covered in gray literature (Chaulagain et al., 2023a). The literatures also indicate a lack of flood modeling systems that combine hydrological, hydraulic and remote sensing approaches for assessing urban flooding in the KVV. While more than one paper has suggested the advantages of linking HEC-HMS and HEC-RAS and including UAV imagery generated DEM or land cover informed roughness parameters (Bohara et al., 2024; Knebl et al., 2005; Peker et al., 2024a), few have been field-calibrated with measured extent of flood or high-water marks. There is potential use of flood models with calibrated parameters or outputs for disaster preparedness and urban planning, but these adequacies become limited due to lack of validation with high-resolution field calibration and with ground observations in flood hazard mapping. A need has therefore emerged for the development of high-resolution, field-calibrated flood hazard mapping which is validated with both satellite and ground-based observations comparing the extent of flooding.

In response to these limitations, this study integrates hydrologic and hydraulic modeling using HEC-HMS and HEC-RAS, supported by high-resolution UAV-derived DEMs and ground-calibrated discharge data for the Bagmati-Nakkhu confluence. In this study, the Digital Elevation Model (DEM) of Bagmati-Nakkhu confluence was obtained using UAV, and the water discharge data obtained from Department of Hydrology and Meteorology (DHM) for Bagmati river (1992-2024) and the water discharge data derived from HEC-HMS for Nakkhu river (2000-2024) were used for flood modelling and simulation in HEC-RAS software, from which flood inundation mapping and hazard mapping of the study area is done for different return periods of 5 year, 10 year, 25 year, 50 year, 100 year and 150 year. In addition to hydraulic and hydrologic modeling, this study employs supervised classification on Sentinel-2 satellite imagery to map the spatial extent of flood-affected areas. This satellite-derived flood extent will be used to validate the inundation boundaries generated by the HEC-RAS model, ensuring spatial consistency between modeled and observed flood extents. Furthermore, field data which are flood extent points and observed flood levels have been collected and utilized for the calibration of the HEC-RAS model. These ground-based observations help refine model parameters and improve the accuracy of simulated flood depths and extents, thereby enhancing the reliability of flood hazard mapping for the Bagmati-Nakkhu confluence region.

Further, while a number of studies have successfully utilized Sentinel-1 SAR data, or UAV-based mapping (drones) for flood detection, in many cases in Nepal, studies face constraints from cloud cover, low satellite revisit times, and lack of training data for supervised classification, all of which are challenges that were faced in part due to the heavy rain that fell during the Joint Flood Studies (Albertini et al., 2024; Palomba et al., 2020). All of these restrictions indicate the value of using Sentinel-2 optical data in conjunction with field observations to validate flood boundary prediction although hybrid studies significantly utilizing field data are seen elsewhere, there are still much fewer undertaken, particularly at the confluences of rapidly flowing flood rivers like the Bagmati-Nakkhu, thereby highlighting the novelty and importance of the present wrapped study.

1.2 Statement of the problem

The Bagmati-Nakkhu confluence area in Kathmandu Valley experiences severe flooding due to record-breaking monsoon rains, leading to significant displacement and infrastructure damage. There is a lack of detailed, site-specific flood hazard assessments grounded in primary data, hindering effective flood risk management and infrastructure planning.

This study addresses these challenges by integrating primary field data collection with hydrological modeling (HEC-HMS) to estimate discharge of Nakkhu, hydraulic modeling (HEC-RAS) to simulate flood inundation scenarios, and supervised classification of satellite imagery to delineate the spatial extent of flood-prone areas.

Each component of the analysis will be rigorously validated against field observations and ground-truth data to ensure accuracy and reliability, to produce high-resolution flood hazard maps that reflect the actual conditions of the Bagmati-Nakkhu confluence area.

1.3 Objectives

The main objective of our study is to simulate flood inundation using hydraulic modeling (HEC-RAS) and develop spatial flood hazard maps for the Bagmati-Nakkhu confluence area.

And the following are the sub objectives developed to achieve the main objective:

1. To collect and preprocess topographical and land use data using DGPS and Unmanned Aerial Vehicle for the Bagmati-Nakkhu basin to support flood modeling and hazard mapping.
2. To map the spatial extent of flooded areas using supervised classification on Sentinel-2 satellite imagery.
3. To estimate the discharge of Nakkhu river using the HEC-HMS hydrological model.
4. To prepare flood hazard maps for different return periods for the study area (5-year, 10-year, 15-year, 50-year, 100-year, 150-year).
5. To validate the flood extent map derived from supervised classification and HEC-RAS modeling of the 27th September 2024 event.

1.4 Scope of Work

This study involves collecting field data, remote sensing imagery, and topographic inputs to support hydrological and hydraulic modeling.

It involves estimation of peak discharge using HEC-HMS, and simulation of flood inundation in HEC-RAS to develop flood hazard maps of Bagmati-Nakkhu Confluence and carry out the use of satellite-based supervised classification and field validation to delineate actual flood extents and assess accuracy.

2 LITERATURE REVIEW

2.1 Flood Hazard Mapping

Hydrological modeling for urban flood hazard and inundation mapping has increasingly incorporated Land Use/Land Cover (LULC) data to enhance the realism and spatial accuracy of simulations. HEC-RAS software has become a widely adopted tool for these applications. Minywach et al. (2024) used HEC-RAS in the upper Awash Basin, Ethiopia, to model flood extents under different LULC scenarios. They performed flood frequency analysis to simulate events with return periods ranging from 25 to 100 years, assigning Manning's n coefficients based on LULC classes such as annual crops, built-up areas, and forests. The results revealed significant differences in inundation extent between land cover types, emphasizing the sensitivity of flood hazard mapping to surface characteristics.

Jean-François et al. (2025) further demonstrated the importance of integrating LULC and climate change projections in flood modeling. In their study of the Mojo River, Ethiopia, they combined Sentinel-1 SAR data processed in Google Earth Engine with HEC-RAS 2D to simulate present and future inundation patterns. The LULC map for 2019 informed the spatial variability of surface roughness, while rainfall projections were incorporated to assess future flood risks. Their findings showed a 16.5–27.2% increase in inundated areas under projected land cover and climate scenarios, underlining the compounding effects of urban expansion and climate variability.

Mustafa et al. (2023) modeled urban flooding in Erbil, Iraq, using HEC-RAS 2D, with LULC and soil data informing terrain resistance and runoff characteristics. They compared two modeling approaches such as building-block and building-resistance representations and highlighted the role of impervious surfaces and microtopography in flood propagation. The calibrated model accurately reproduced historical flood events, reinforcing the validity of incorporating LULC for urban flood risk assessment. Other regional studies, such as Getahun and Gebre SL (2015) worked on Ethiopia's Awash River and Tenzin and Bhaskar's (2017) modeling of flash floods in Bhutan, used HEC-GeoRAS and LULC-derived Manning's n values to produce depth-based hazard maps in rapidly urbanizing basins.

At a more technical level, Jung and Ma (2024) demonstrated how regulatory flood maps could be enhanced using HEC-RAS 2D and land cover-based roughness parameters. Their comparative study with SWMM illustrated that assigning roughness from detailed land cover datasets improves floodplain delineation for FEMA mapping. Similarly, Hejazi, (2023) introduced the FIRM 2D methodology in Baltimore, Maryland, combining HEC-RAS 2D, HEC-HMS hydrology, and LULC-informed Manning's n to generate urban flood extents suitable for regulatory applications.

Integrating Land Use/Land Cover (LULC) data into HEC-RAS modeling is pivotal for generating accurate flood hazard maps, particularly in urban settings where surface characteristics significantly influence flood dynamics. The process typically begins with the preparation of a high-resolution Digital Elevation Model (DEM) to represent the terrain. Subsequently, LULC maps are utilized to assign Manning's roughness coefficients (n) to different land cover types, reflecting their resistance to flow. For instance, in the Pathariya Khola study in Nepal, researchers assigned varying n values to land cover classes such as barren land, cultivated areas, and forests, based on

established hydraulic references (Upadhyaya et al., 2023). The coefficients were then incorporated into the HEC-RAS model to simulate flood scenarios across different return periods, resulting in detailed inundation extents and depth maps (Adhikari & Panthee, 2020). The integration of LULC data extends beyond roughness coefficients. In the Bishnumati River study in Nepal, the HEC-GeoRAS extension was employed alongside HEC-RAS to process spatial data within a GIS environment. This approach facilitated the delineation of floodplains by combining hydraulic modeling results with LULC information, enabling the identification of vulnerable urban areas and the assessment of potential impacts on different land use types (Dangol & Bormudoi, 2015). Collectively, these studies reinforce the value of integrating LULC into flood hazard mapping using HEC-RAS. They demonstrate that spatial variability in land cover significantly influences flood depth, velocity, and extent, particularly in urban environments. From regional applications in South Asia and Africa to regulatory modeling in the U.S., LULC data has emerged as a critical input for simulating realistic flood scenarios, guiding both risk assessment and floodplain management.

Knowing the dynamics of flood hazards entails more than understanding the risks; it requires the ability to model and simulate how those flood hazards will behave under different conditions. Application maps may indicate those areas known to be prone to flooding, the evidence for mapping needs to be supported by tools capable of simulating how water behaves in a natural and built environment (Marina & Oana, 2015). One of the most commonly used simulation tools used in flood hazard analysis is the HEC-RAS. HEC-RAS allows researchers and planners to model flood depth, extent, and velocity based solely upon several hydraulic conditions of the river and site's topography. The next section will elaborate on HEC-RAS and how they can be informative to flood hazard assessments.

2.2 Hydrologic Engineering Center - River Analysis System (HEC-RAS)

HEC-RAS (Hydrologic Engineering Center - River Analysis System) is a software program developed to simulate the hydraulics of water flow through natural streams and engineered channel networks. It is widely used for modeling river hydrodynamics, including water surface profiles, flow velocities, and flood extents (Lad & Shah, 2021). HEC-RAS is easily accessible and commonly employed model for one-dimensional analysis of steady flow, making it suitable for floodplain mapping (Basnet et al., 2018). With the help of HEC-RAS, the flood hazard maps for various return period floods can be created (Aryal et al., 2020).

HEC-RAS is a widely recognized and extensively tested model that is often used as a benchmark for comparing the performance of other hydrodynamic simulation software. HEC-RAS allows users to estimate water surface profile along a river in a steady and unsteady flow river hydraulic calculation including sediment transport modelling (Marina & Oana, 2015). The energy and momentum equations (Eqs. 1 and 2) are used to derive the one-dimensional Saint-Venant equations, which are employed in HEC-RAS to simulate steady and unsteady flow water surface profiles using the implicit finite difference method (Zainalfikry et al., 2020a).

The one-dimensional Saint-Venant equations govern unsteady open channel flow. They consist of the continuity equation and the momentum equation:

Continuity Equation:

$$\frac{\partial A}{\partial t} + \frac{\partial S}{\partial t} + \frac{\partial Q}{\partial x} - q = 0 \quad (1)$$

Momentum Equation:

$$\frac{\partial Q}{\partial t} + \frac{\partial(VQ)}{\partial x} + gA \left(\frac{\partial z}{\partial x} + S_f \right) = 0 \quad (2)$$

Where,

A = Cross-sectional flow area (m^2)

S = Ineffective flow area (m^2)

Q = Discharge or flow rate (m^3/s)

q = Lateral inflow per unit length (m^2/s)

t = Time (s)

x = Distance along the channel (m)

V = Flow velocity (m/s)

z = Bed elevation (m)

S_f = Friction slope (dimensionless)

g = Gravitational acceleration (9.81 m/s^2)

The challenge of urban floods lies in the unpredictable flow conditions in urban areas, caused by rapid changes in the landscape and the lack of extensive data. Thus, modeling of urban floods becomes a complex process. In recent years, numerous numerical models have emerged, each capable of flood mapping. Many of these models are commercially available, highly accurate, and require extensive datasets to produce precise results (Rangari et al., 2019). According to Prafulkumar et al. (2011), with rapid advancement in computer technology and research in numerical techniques, various 1-D hydrodynamic models, based on hydraulic routing, have been developed in the past for flood forecasting and inundation mapping. Hutanu et al. (2020) found that the 1D HEC-RAS provides a more realistic perspective about the possible flood threats within Jijia floodplain and improves the accuracy of the official flood hazard maps obtained according to Flood Directive 2007/60/EC. Diedhiou et al. (2020) proposed that results given by HEC-RAS simulations are the variations of the water levels, the temporal variations of the flow rates for each section, the maximum flow velocities and the propagation times of the flood waves. His thorough analysis and comparisons of his findings strongly indicate that HEC-RAS issues can be effectively utilized as a decision-making tool to manage floods during times of crisis.

Bohara et al. (2024) utilized HEC-RAS to generate 1D flood maps for multiple return periods and employed ArcGIS for flood hazard and risk assessment. Their study has analyzed long-term precipitation using Hazen, California, and Weibull methods, while flood frequency was estimated using Gumbel, Weibull, and Log Pearson Type III distributions. Acharya et al. (2011) explored HEC-RAS to model steady flow based on calculated discharge values, integrating TIN and river geometry generated through HEC-GeoRAS. They have further delineated floodplains and developed hazard, vulnerability, and risk maps at multiple scales and return periods using ArcGIS. Bhargav and Suresh (2025) explored the Karjan river's flood dynamics by integrating HEC-RAS 1d unsteady flow modeling with geospatial techniques, derived river features from ALOS PALSAR data, and validated flood depth outputs against historical events to ensure model accuracy. Lad and Shah (2021) demonstrated the use of ArcGIS and HEC-RAS for 1D flood modeling of the Damanganga River, developed a hydrodynamic model to determine water levels from the Arabian Sea, and assessed flood control measures by simulating peak discharge scenarios across historically flood-prone years. Niraula and Shakya (2020) conducted 2D flood modeling of Ratuwa Khola and Mauwa Khola in Eastern Nepal using HEC-RAS, generated flood hydrographs with Snyder's Unit Hydrograph and Gumbel's distribution, and validated inundation extents against satellite-based data from the Rastrapati Chure Conservation Program. Aryal et al. (2020) also conducted flood hazard and risk assessments for a 38 km stretch of the Karnali River using HEC-RAS, simulated floods for multiple return periods using Gumbel's distribution, and evaluated impacts on infrastructure and agriculture, highlighting significant risks to livelihoods and food security. Vashist and Singh (2023) demonstrated the use of HEC-RAS 2D for flood inundation mapping in the Krishna River Basin, employed high-resolution DEMs to assess flood extents, and examined the influence of upstream boundary variations, with outcomes aligning well with existing validation data.

2.2.1 Manning's Coefficient (n)

Key inputs to HEC-RAS include channel geometry (cross sections), surface roughness, and boundary conditions. Ahmad et al. (2016) mentioned steady-component module calculates water surface profiles from steady input discharge data at an upstream cross-section, from river geometry as well as surface roughness data for the river section under examination. The main output variables of his analysis are the water surface elevation above a base altitude for the defined river cross-sections as well as the flow velocity. According to Zainalfikry et al. (2020b), the spatial input data includes a DEM of the watershed, cross-section river geometry, channel and floodplain surface roughness in terms of Manning's roughness coefficient. The river profiles were assigned with specific Manning's roughness coefficient (n). The n value describes the resistance to flow and was assigned based on standard reference suggested by Chow, (1959). Manning's n for 1D HEC-RAS model is limited to one value for channel and two values for floodplain.

Choosing the right value for the manning coefficient (n) is crucial, as it directly affects the precision of water surface profile calculations. The value of the Manning coefficient is highly variable and depends on a number of factors including: bed roughness in a channel, vegetation, channel meandering, scour and deposition, the shape of the channel, seasonal changes, and suspended material. The Manning coefficient value can be calibrated when information on the observed water surface profile is available. If these measured data are not available, values of

Manning's n computed for identical stream conditions or values extracted from experimental data can be used as guides in the selection of n values (Iosub et al., 2015). The roughness coefficient varies seasonally, and identical stage conditions may result from different discharges. While traditionally linked to riverbed characteristics, accurately measuring and capturing its spatial-temporal variation remains challenging, introducing significant uncertainty in hydraulic modeling (Balta, 2024).

Roughness values (Manning's n) are often derived from land cover or obtained via calibration. Many studies apply spatially variable n based on land use or field judgment. For example, Hutanu et al. (2020) computed Manning's n for each cross section from land-cover classes (e.g. $n=0.3$ for built-up, 0.05 for vegetation, 0.025 for crops, 0.04 for open water). In Jordan, field surveys and aerial photos similarly informed n -values for channels and floodplains (Al Kuisi et al., 2024a). Arcement and Schneider (1989) provided a foundational guide linking various LULC types such as forests, agricultural lands, and urban surfaces to typical n -values, which has since been widely adopted. Integration of LULC-derived Manning's values into hydraulic models has been facilitated through Geographic Information Systems (GIS), allowing for spatially variable roughness assignment. Patel & Srivastava (2013) applied this approach in the Koshi River Basin, India, where CORINE and National Land Cover Dataset (NLCD) classifications were reclassified to match typical roughness values for floodplain modeling. Similarly, Choudhury and Ojha (2013) demonstrated how LULC-based roughness maps enhanced model precision in the Brahmaputra floodplains, resulting in more reliable flood extents. In more recent studies, satellite-derived LULC products, including those from Landsat and Sentinel imagery, have been classified using supervised algorithms and linked with standard Manning's tables to generate high-resolution n -value maps (Ghimire et al., 2020). Such methods enable dynamic updates to hydraulic models in response to land use change, making them particularly valuable for climate resilience planning and long-term flood risk assessment. The combined effect of roughness and cross-sectional shape controls conveyance; thus, careful assignment of n is critical, as many authors note its high impact on flood levels.

2.2.2 Boundary Condition

Boundary conditions specify upstream flows and downstream tailwater. For steady simulations, upstream flow is a peak discharge (for the given return period) and downstream water surface is set by normal depth or a stage. For instance, Kim et al. (2020) set a normal depth boundary at the downstream end of the Cambodian reach. For unsteady modeling, time-varying hydrographs are used. Standard practice (per UN-SPIDER guidance) is to apply an upstream flow hydrograph and a downstream stage hydrograph at gauge points (UN-SPIDER, 2010). In Jordan, peak flows from HEC-HMS were input as steady flows at the upstream ends, with the downstream flow assumed as normal depth (Kuisi et al., 2024b). Across the literature, boundary conditions are chosen to reflect known conditions: either extrapolated water surface or recorded stage at downstream gauges, and estimated peak flows (from frequency analysis or hydrologic modeling) upstream.

To carry out steady flow analyses, it is necessary to define boundary conditions that determine the water surface elevation at the beginning and end of each river reach. HEC-RAS can then start to calculate the 1d water surface profile. To comprehend the significance of boundary conditions,

work in HEC-RAS, it is crucial to have a clear understanding of how water surface profile calculations are carried out in HEC-RAS. In HEC-RAS, one-dimensional (1D) steady-state flow computations are based on the energy equation shown below:

$$Z_2 + Y_2 + \frac{a_2 V_2^2}{2g} = Z_1 + Y_1 + \frac{a_1 V_1^2}{2g} + h_e \quad (3)$$

Where,

Z_1, Z_2 = Elevation of the main channel inverts at sections 1 and 2 (m)

Y_1, Y_2 = Depth of water at cross sections 1 and 2 (m)

V_1, V_2 = Average velocities at sections 1 and 2 (m/s), calculated as total discharge divided by flow area

a_1, a_2 = Velocity weighting coefficients (dimensionless)

g = Gravitational acceleration (9.81 m/s^2)

h_e = Energy head loss between the two sections (m)

Different boundary conditions are available for steady flow analyses and unsteady flow analyses: Normal Depth, Critical Depth, Rating Curve, Known Water Surface Elevation and many more. The most commonly employed boundary condition for steady and unsteady analyses is the normal depth. The user is obliged to provide an energy gradient. HEC-RAS will use that value to compute depth using Manning's equation. We can approximate the energy slope by measuring the slope of the reach downstream of your modeled reach. The normal depth of water in hydraulic modeling can be calculated using the Manning's equation (Brue, 2022).

2.2.3 Flood Frequency Analysis

Generating flood hazard maps requires simulating floods for multiple return periods. Researchers perform flood frequency analysis using gauge records or regional methods to estimate design flows (e.g. 10-, 50-, 100-year discharges). The chosen flows (peak or hydrograph) are then imposed in HEC-RAS. According to Aryal and Regmi (2022), the estimation of the occurrence of the flood in the future is very important for quantitative analysis of extreme flood events. There is no such method that computes the precise value of streamflow or precipitation responsible for the flooding. Mostly there are three types of empirical and probabilistic approach which are used for the analysis of flood. Gumbel's, Log Normal and Log Pearson III type, etc. are the methods which are based on probability theory. In most of the studies, the most commonly used probability distribution function proposed by Gumbel was employed for predicting peak flow and maximum precipitation. Also, according to Parhi (2018), the Gumbel's distribution, initially proposed by Gumbel, is the most frequently employed method for extreme value analysis. It is extensively utilized for predicting flood peaks, maximum rainfall, maximum wind speed, and other extreme events. In his study Gumbel's extreme value distribution function was used to estimate the peak floods for return periods of 10, 25, 50 and 100 years for Mahanadi River.

Bhagat (2017) noted that while various statistical distributions have been used to estimate flood likelihood and intensity, no single method has achieved universal acceptance. To support hydrologic design in the Lower Mahi River catchment, the Gumbel distribution was applied to model annual peak discharge data from 1989 to 2009. Kim et al. (2020) analyzed 30 years of peak-discharge data at Kampong Cham (Mekong River) to derive 10, 20, 50, and 100-year floods from Gumbel distribution, then ran steady HEC-RAS with those flows. Basnet et al. (2018) used the catchment-area ratio method and Gumbel's distribution to estimate 20-, 50-, 100-year peaks for the ungauged Seti River. Al Kuisi et al. (2024a) used HEC-HMS to produce hydrographs for 2-, 10-, 25-, 50-, 100-, and 1000-year events, then ran HEC-RAS (steady) for each scenario. The model outputs water surface elevations and flood depths for each scenario; these are exported to GIS to delineate hazard zones. Typically, depth and extent layers are classified (e.g. low/medium/high hazard) for each return period. Many studies explicitly prepare maps for multiple floods (e.g. 10-, 20-, 50-, 100-year) to show increasing inundation with rarity (Kim et al., 2020).

According to Malik & Pal (2021), Extreme Value Type that is Gumbel's method distributions are generally modelled for storm rainfall events, and this model can be used for river flow also. The Gumbel's distribution method of frequency analysis needs minimum ten years annual maximum historical data to assume the probabilistic future prediction. According to (Bhagat, 2017), the equation for Gumbel's distribution as well as to the procedure with a return period 'T' is given as:

$$X_T = \bar{X} + K \cdot \sigma_x \quad (4)$$

Where,

σ_x = Standard deviation of the Sample Size

K = Frequency Factor, which is expressed as,

$$K = \frac{Y_T - \bar{Y}_n}{S_n} \quad (5)$$

In which, Y_T = Reduced Variate,

$$Y_T = - \left[\ln \left(\ln \left(\frac{T}{T-1} \right) \right) \right] \quad (6)$$

The values of \bar{Y}_n and S_n are selected from Gumbel's Extreme Value Distribution considered depending on the sample size.

While HEC-RAS offers the hydraulic modeling framework to examine flows through river systems and floodplains, it ultimately depends on sound upstream flow information. This flow information typically originates from hydrologic models that simulate the conversion of rainfall as runoff to form hydrographs illustrating the timing and volume of water actually entering the system (Khan et al., 2024). One of the most widely used tools in this regard is the Hydrologic Engineering Center's Hydrology Modeling System (HEC-HMS). If we are to expect the results from HEC-

RAS to be meaningful, we need to understand the role HEC-HMS plays in producing acceptable, realistic, and dependable hydrologic inputs.

2.3 Hydrologic Engineering Center - Hydrologic Modeling System (HEC-HMS)

HEC-HMS is a computer program that simulates precipitation runoff processes in dendritic drainage basins. The Hydrologic Engineering Center of the U.S. Army Corps of Engineers has developed a hydrological set of mathematical models known as the HEC-HMS, which is used to simulate the precipitation runoff-routing processes of dendritic watershed systems (Sampath et al., 2015). It is a generalized modeling system that is used to represent diverse watersheds by breaking down the hydrologic cycle into components and defining watershed boundaries. Key parameters such as initial loss, curve number, impervious area, lag time, and initial discharge are calibrated to closely match observed and simulated hydrographs (Tahmasbinejad et al., 2015). According to Khélifa & Mosbahi (2022), the HEC-HMS software consists of four sub-models: a basin model, meteorological model, control specifications, and time-series data. It offers the possibility to use numerous routing, hydrographs and infiltrations methods. It comprises various sub-processes for the loss of rainfall, direct runoff, and the path of water flow. HEC-HMS has gained widespread popularity and has been widely adopted in hydrological studies due to its capability in simulating runoff for both short and long-term events, its ease of operation, and utilization of commonly used methods (Oleyiblo & Li, 2010).

The model can operate in both event-based and continuous modes to generate watershed hydrographs and peak flow estimates across diverse environments. In practice, HEC-HMS output (runoff volumes and peak discharges) is often routed into hydraulic models or GIS tools to delineate inundation and hazard zones (Peker et al., 2024b). Peker et al. (2024b) used HEC-HMS with multiple return-period storms to produce 2D HEC-RAS flood scenarios and then derived depth-velocity hazard maps for the Göksu Basin in Türkiye. Similarly, Khan et al. (2024) applied HEC-HMS in Dubai to simulate event runoff and calculate peak discharges associated with impervious-area trends, thereby identifying the most flood-prone sub-basins. HEC-HMS captures both direct runoff and baseflow processes needed for flood peaks. Critically, HEC-HMS outputs (runoff hydrographs and volumes) have been fed into hydraulic or GIS models to map inundation and hazards. Ethiopian researchers applied HEC-HMS-generated hydrographs as upstream boundary conditions in HEC-RAS and Google Earth Engine to produce flood inundation maps under climate scenarios (Belay et al., 2025). These and other studies demonstrate that HEC-HMS's runoff computations feed directly into broader flood hazard assessments, effectively linking precipitation inputs to spatial flood-risk outputs.

From the exhaustive review work carried out on the HEC-HMS rainfall-runoff model, Sahu et al. (2020) concluded that the selection of the modelling method and approach is mainly based on the desired output and availability of the data. They analyzed the work of researchers who compared different modelling methods to obtain the best model suitable under different hydrological conditions and found HEC-HMS as a good model over others and recommended it for simulation of runoff. From the reviews, the HEC-HMS rainfall-runoff model is a wide range of applications in flood forecasting and water resource planning and management (Martin et al., 2012). Khélifa and Mosbahi (2022) mention that this model is designed to be applicable in different geographic

areas for solving the widest possible range of problems. It is commonly employed to simulate the generation of runoff in extensive river systems, compact urban or natural watersheds, and areas without water level measurements. Paudel et al. (2019) finds that the SCS (soil conservation service) curve number loss method, SCS (soil conservation service) unit hydrograph method, constant monthly baseflow method, and Muskingum routing method are the best fit performed methods of the hydrological processes of infiltration loss, direct runoff transformation and base flow part of the model. Asadi and Boostani (2013) also employed the SCS curve number method to model infiltration loss. The SCS unit hydrograph method to model the transformation of precipitation excess into direct surface runoff. The constant monthly method was employed to model baseflow and the Muskingum routing model was used to model the reaches.

2.3.1 Loss Model (SCS Curve Number)

In HEC-HMS, for each component of the runoff process, different methods or models are available. Each method has parameters, and the values of these parameters need to be entered as inputs to the model. To compute the losses from the basin, the SCS CN loss method was used, which includes the curve number and percent of imperviousness for each basin (Koneti et al., 2018).

The Curve Number (CN) method is a widely used empirical rainfall–runoff model developed by the U.S. Soil Conservation Service (now NRCS) in 1954. It assigns a dimensionless index (typically between 30 and 100) to characterize the runoff potential of different combinations of soil type, land use, and antecedent moisture conditions, where higher CN values indicate higher runoff potential (USDA NRCS, 2004). The model is based on a conceptual relationship between rainfall, initial abstraction (e.g., interception and infiltration), and potential maximum retention, SSS, which is inversely related to the curve number. The CN values were originally calibrated from numerous small watershed experiments across the United States (Mishra & Singh, 2003). While it provides a simplified means to assess runoff based on land surface properties, the method aggregates complex hydrologic processes into a single parameter and lacks sensitivity to spatial and temporal variability (Woodward et al., 2003).

Halwatura and Najim (2013) also used the SCS curve Number and according to them the SCS CN method implements the curve number methodology for incremental losses. The program calculates the incremental precipitation during a storm by recalculating the infiltration volume at the end of each time interval. The amount of water that infiltrates during each time interval is the difference in volume between the end of one-time interval and the start of the next. They also mention that the SCS CN method requires percentage land use pattern of the catchment and the sub catchments, total length of the river and the elevation of the catchment area. SCS CN model estimates precipitation excess by considering cumulative precipitation, soil cover, land use, and antecedent moisture content.

According to Wang et al. (2023), Considering the change in land use, the loss method selected is the SCS curve number. In this method, the net rainfall is estimated as a function of accumulated rainfall, land cover, land use, and previous humidity, as shown below:

$$P_e = \frac{(P - I_a)^2}{P - I_a + S} \quad (7)$$

Where,

P_e = Direct runoff (mm or inches)

P = Precipitation (mm or inches)

I_a = Initial abstraction ($0.2 * S$)

S = Potential maximum retention after runoff begins (mm or inches)

Again, the potential maximum retention after runoff begins can be estimated by:

$$S = \frac{25400}{CN} - 254 \quad (8)$$

Where,

CN is the Runoff Curve Number.

Low CN values mean that the surface of the basin has a high potential to retain water, whereas high values indicate that the rainfall could only be stored to a limited extent (Khaddor et al., 2017). Initial abstraction (I_a) in the SCS-CN method is the portion of rainfall lost (in interception, depression storage, infiltration) before runoff begins.

Jaafar et al. (2019) found that recent advances in global hydrological datasets have revolutionized curve number (CN) estimation, particularly through the GCN250 global gridded dataset. This 250m resolution dataset combines the European Space Agency's Climate Change Initiative land cover product (ESA CCI-LC) with the HYSOGs250m hydrological soil group classification, providing CN values for three antecedent moisture conditions (dry, average, wet). He also mentioned that studies validate GCN250's effectiveness in South Asian basins, with research demonstrating 0.925 correlation between predicted and observed runoff when using GCN250 CNs in SCS-CN modeling (Jaafar et al., 2019). The dataset's 250m resolution captures Kathmandu's micro-scale land use variations, from dense urban cores (CN=92-98) to peri-urban farmlands (CN=72-86).

2.3.2 Transform Model (SCS Unit Hydrograph)

The SCS-UH transforms excess rainfall into a runoff hydrograph using a dimensionless unit hydrograph shape and a lag or peak time parameter. By construction, the SCS-UH relates the time-to-peak (T_p) to the basin time-of-concentration (T_c). HEC-HMS requires specifying a precipitation-runoff transform (PRF) and a basin lag time (lag) to use the SCS-UH. In many studies (Romania, Ethiopia, India, etc.) the lag is initially estimated from catchment geometry (Herbei et al., 2024). Lag time refers to the duration between the center of the precipitation mass and the highest point of water flow. The Romanian study of Herbei et al. (2024) computed basin lag from Mishra and Singh's formula and then adjusted it by calibration. Kulkarni and Kale (2022) tested SCS-UH versus Clark UH in India, while Tangam et al. (2024) compared SCS-UH with other transforms in the Niger/Sirba basin. Overall, the SCS-UH is widely used for ungauged or limited-data basins globally due to its empirical simplicity.

The lag time is calculated from the formula:

$$T_{lag} = 0.6 * T_c \quad (9)$$

Where,

T_{lag} and T_c are the lag time and time of concentration in hours (Al-Mukhtar & Al-Yaseen, 2019b).

Also,

$$T_{lag} = \frac{L^{0.8}(S + 1)^{0.7}}{1140 \cdot Y^{0.5}} \quad (10)$$

Where,

T_{lag} = Lag Time (in hours)

L = Length of the main watercourse (in feet)

S = Potential maximum retention (in inches)

Y = Average watershed slope (in percent)

2.3.3 Routing (Muskingum)

The Muskingum method is a storage-based routing technique extensively utilized in HEC-HMS. It symbolizes channel storage as the combination of prism and wedge. The Muskingum routing method employs a straightforward conservation of mass approach to guide the flow of water through the stream reach. Nevertheless, it does not assume that the water surface is flat. By assuming a non-level water surface, it becomes possible to consider the increased storage during the rising phase of a flood wave and the decreased storage during the falling phase (Gill, 1978). The Muskingum k represents the duration of travel within the reach. It can be estimated from the knowledge of the cross-section properties and flow properties. The Muskingum X is the weighting between inflow and outflow influence (Sampath et al., 2015). The Muskingum model is favored in practice for its ability to capture flood-wave attenuation and is used in many basin models (e.g. Ethiopia, Romania, India) as shown by the broad use of HEC-HMS (Al-Mukhtar & Al-Yaseen, 2019a).

In this model, calibration for two parameters, ‘X’ and ‘K’, can be required to increase the match between observed and simulated hydrograph. ‘K’ is dimensionless weight, which is a constant coefficient that varies between 0 and 0.5, where ‘X’ is a factor representing the relative influence of flow on storage levels. It can be assumed that the value equals 0.1 as an initial value of the parameters, which can be corrected during the calibration process. ‘K’ is estimated using the equation:

$$K = \frac{L}{V_w} \quad (11)$$

Where,

L = Length of the main watercourse (in feet)

V_w = Flood Wave Velocity, which can be taken as 1.5 times the Average Velocity

2.3.4 The Nash–Sutcliffe Efficiency (NSE)

The Nash–Sutcliffe efficiency (NSE) has become a standard, widely-used metric for assessing hydrological model performance (Moriasi et al., 1983; Nash & Sutcliffe, 1970; Pushpalatha et al., 2012). In effect, NSE quantifies the fraction of observed flow variance captured by the model by computing one minus the ratio of simulation error variance to observed variance (Gupta et al., 2009). The Nash–Sutcliffe Efficiency (NSE) is used in calibrating HEC-HMS models by comparing simulated hydrographs to observed streamflow data. During calibration, model parameters are adjusted to maximize the NSE value, indicating better alignment between simulated and observed flows (Gebre, 2015).

By definition, NSE ranges from negative infinity to 1. an NSE of 1.0 indicates a perfect match between simulated and observed stream flows, NSE = 0 means the model is only as good as using the long-term mean, and negative values imply the model is worse than this naïve benchmark (Moriasi et al., 1983; Ritter & Muñoz-Carpena, 2013). Values between 0 and 1 are therefore interpreted as progressively better performance. In practice, many studies and evaluation guidelines use heuristic thresholds: for example, NSE > 0.50 is often taken as “satisfactory” performance, while values above roughly 0.65–0.75 are viewed as “good” or “very good” fits (Krause et al., 2005; Moriasi et al., 1983). Moriasi et al. (1983), for instance, explicitly recommend NSE (along with bias and RSR) as a primary calibration statistic and note that achieving NSE > 0.50 typically signifies a satisfactory streamflow simulation. Likewise, recent modeling studies routinely report NSE and interpret high values as indicators of strong model skill (e.g., classifying NSE > 0.75 as very good) (Abbaspour et al., 2017; Bennett et al., 2013). In sum, the peer-reviewed literature consistently treats NSE as an interpretable, useful gauge of hydrologic model accuracy, endorsing its use (often in concert with other metrics) whenever model and observed flow hydrographs are compared (Pushpalatha et al., 2012).

2.4 Integration of Hydrologic and Hydraulic Models

Because both hydrologic and hydraulic components are essential for modeling flood events, the dual use of HEC-HMS and HEC-RAS in modeling studies has become a standard and effective strategy (Peker et al., 2024a). This approach enables first, a rainfall-runoff analysis followed by hydraulic routing for flood modeling, with an improved, complete, and spatially representative depiction of flooding behavior. The integration of HEC-HMS and HEC-RAS improve prediction for flood extent, peak flows and timing of flood inundation. The HEC-HMS and HEC-RAS integration is particularly useful for environments with limited data or rapidly urbanizing basins with complex and ever-changing flood impacts (Thakur et al., 2017).

The coupling of HEC-HMS and HEC-RAS involves using HEC-HMS to simulate rainfall-runoff processes, generating hydrographs that serve as input boundary conditions for HEC-RAS, which then models the river's hydraulic behavior and floodplain inundation. This integrated modeling approach has been applied in various studies worldwide (Thakur et al., 2017). In the study of Peker et al. (2024a), HEC-HMS was used to simulate flow rates for different return periods (25, 50, 100, 500), which were then input into HEC-RAS for hydraulic modeling. Manning's n values were derived from CORINE land cover data, and a 5 m resolution digital surface model was employed

to enhance the accuracy of flood hazard mapping. In context of Junjung River Catchment, Malaysia, Ata et al. (2023) developed hydrological models using HEC-HMS and HEC-RAS to forecast river behavior during significant rainfall events. The models were calibrated using observed streamflow data, and the results were utilized to create flood hazard maps for 50- and 100-year return periods. Knebl et al. (2005) also demonstrated the integration of these models facilitated the assessment of flood risks associated with land use changes and climate variability.

Several other studies have also explored the effectiveness of integrated hydraulic and hydrologic modeling approaches in flood risk assessment and forecasting. For instance, Pathan and Agnihotri (2019) applied a one-dimensional flood modeling approach using HEC-RAS and ArcGIS to delineate flood extents in the lower region of Navsari City. Similarly, the integration of tools like HEC-RAS and the HEC-HMS model has proven valuable for developing flood risk maps and forecasting models across various return periods (Parhi, 2018b). In another study, Afzal et al. (2022) utilized GIS in combination with HEC-RAS to model flooding across different cross-sections of the Purna River Basin. Additionally, tools like HEC-RAS and the Global Flood Monitoring System (GFMS) have been recognized for their capability in accurately delineating flood-prone zones, providing crucial support to disaster management agencies for issuing early warnings to at-risk communities (Dwivedi et al., 2020).

While integrated models of hydrology and hydraulics provide a robust basis for simulated flood behavior, their reliability is inherently dependent on the quality of the topographic data as representations of the terrain. Inaccurate or coarse elevation data can greatly diminish the reliability of flood predictions (Annis et al., 2020a). As such, many recent studies have utilized high-resolution digital elevation models (DEMs) created with unmanned aerial vehicles (UAVs). DEMs created with UAVs will often reveal previously unrecognized surface variations that lower-resolution datasets, previously utilized as DEM or topographical data, failed to capture resulting in enhanced accuracy for the modelling outputs (Clasing et al., 2023).

2.5 Usage of Unmanned Aerial Vehicle (UAV) for DEM Generation

Unmanned Aerial Vehicles (UAVs) equipped with cameras or LiDAR can rapidly produce very high-resolution terrain models. Structure-from-motion photogrammetry from UAV imagery yields centimeter-scale Digital Elevation Models (DEMs) at low cost and effort (Annis et al., 2020b). Such DEMs capture fine features such as riverbed micro-topography, bank geometry and small levees that coarser maps miss, improving hydraulic model fidelity. Parizi et al. (2022) showed that using a 1 m UAV-derived DEM versus a 30 m ASTER DEM in 2D HEC-RAS flood simulations of Iran's Atrak River changed flood extent by about 17% (Parizi et al., 2022). Similarly, Clasing et al. (2023) built a 1D HEC-RAS model of Chile's Ñuble River using a UAV bathymetric survey and validated it against a June 2023 flood; the model produced only ~10.6% mean error in water depth (30-year flood), demonstrating that UAV-derived terrain yielded highly accurate flood predictions. emphasize that UAV surveys deliver DEMs “with very high resolution and accuracy” at far lower cost/time than LiDAR or satellite methods, and indeed their case study (Italy) found the UAV-based DEM supported flood simulations closely matching higher-end benchmarks (Annis et al., 2020b).

These UAV-derived DEMs are routinely used as inputs to HEC-RAS to extract river cross-sections and floodplain topography. Iqbal et al. (2023) applied a UAV-based terrain model in a 2D HEC-RAS simulation of Bangladesh's Jamuna River that closely reproduced the June–July 2020 floods when compared against field photos and observations. In Turkey, Aci et al. (2023) performed UAV flights (5–15 m altitude, <1 cm spatial resolution) to map a stream on a forest road and generate HEC-RAS geometry for culvert design. In summary, numerous studies (Asia, Europe, Africa, Latin America) have demonstrated that UAV-derived DEMs, when fed into 1D or 2D HEC-RAS, significantly improve river and floodplain modeling accuracy by providing detailed topography for channel and overbank areas.

Even though precise terrain data assists with modeling surface flood extents, it's also important to be able to validate those models against real flood events. This is crucial in urban and semi-urban catchments because there are microtopographic and land cover differences that will affect the spread of flooding (Foroughnia et al., 2022). Supervised classification of satellite imagery is a prevalent and useful method to map real flood extent during or after the event. By comparing modeled flood extents with observations of inundation from approved sources like Sentinel-1 or Sentinel-2, researchers will be able to assess the realism of their flood modeling and perform validation (Huang & Jin, 2020).

2.6 Supervised Classification for Flood Extent Mapping

Supervised classification is one of a primary technique for extracting flood extent from remote sensing imagery. This method involves training a classifier with labeled data representing water and non-water areas, and then applying the classifier to the imagery to identify flooded regions (Palomba et al., 2020). SAR imagery, such as that from Sentinel-1, can penetrate clouds and rainfall, proving advantageous for flood detection (Amitrano et al., 2024). Palomba et al. (2020) proposed a supervised machine learning approach for flood delineation using Sentinel-1 data, highlighting the effectiveness of SAR in overcoming cloud cover limitations. SAR data, however, is susceptible to speckle noise and requires specialized processing, which can complicate analysis. Moreover, SAR systems face challenges related to temporal availability. Sentinel-1 (C-band) revisits a location every 6–12 days. If a flood peaks and recedes between SAR acquisitions, no flood signal is captured. Studies show that even with dual Sentinel-1 satellites, only a fraction of flood events are imaged at peak (Notti et al., 2019). Limited availability of SAR data, particularly noted during 2023-2024, results in lower temporal resolution for flood monitoring (Hu et al., 2025). When SAR images from the actual flood dates are unavailable, accurate flood delineation becomes particularly challenging. While the use of the mean and median SAR images can be helpful, accurate delineation remains difficult. Additionally, SAR backscatter exhibits limited sensitivity to surface changes under certain conditions, potentially resulting in incomplete flood detection (Zum Zwecke et al., 2005).

To overcome the limitations of individual sensors, several studies emphasize the combined use of optical and SAR data. Tavus et al. (2020) explored a fusion approach using both Sentinel-1 and Sentinel-2 datasets for flood mapping, aiming to integrate the benefits of both data types. Konapala et al. (2021) investigated the use of Sentinel-1 and Sentinel-2, assessing their capability for generating accurate flood inundation maps through various band combinations and deep learning

techniques, indicating that the combined use of Sentinel-1, Sentinel-2, and elevation information improves flood mapping accuracy. Tarpanelli et al. (2022) assessed the effectiveness of Sentinel-1 and Sentinel-2 for flood detection in Europe, further supporting the value of these Sentinel satellites in flood monitoring. Petropoulos et al. (2024) also leveraged Sentinel-2 and Geographical Information Systems (GIS) for mapping flooded regions, demonstrating the combined utility of these resources in flood analysis.

Recent research has demonstrated the efficacy of machine learning algorithms in supervised classification for flood mapping when applied to Sentinel-2 imagery for flood detection (Albertini et al., 2024). These methods typically require training data comprising spectral signatures from known flooded and non-flooded areas to develop classification models that can effectively discriminate between these categories across the broader image. Sentinel-2's key advantage for flood mapping is its high spatial resolution, allowing precise flood boundary detection. Under clear skies, its optical sensors sharply distinguish water from land, exploiting water's low NIR reflectance (Tarpanelli et al., 2022). Optical sensors like Sentinel-2 offer very high spatial (10 m) and spectral resolution, enabling detailed flood mapping whenever cloud cover is low. Sentinel-2 imagery can successfully delineate inundated areas when clear-sky images are available. Li et al. (2024) even developed a gap-filling method using Sentinel-2 (and Landsat) to produce seamless 2–3 day flood maps at 30 m resolution, achieving high accuracy (average F1-scores nearly equal to 0.93 during floods).

The Maximum Likelihood Classifier (MLC) is a classic Bayesian method that assigns each pixel to the class with highest probability (assuming Gaussian spectral distributions) (Ghayour et al., 2021). It is often a strong choice for flood mapping, especially with good training data. Notti et al. (2019) tested multiple classifiers on Landsat/Modis images and chose maximum likelihood (and spectral angle) as “most appropriate” for detecting flooded areas. Farhadi et al. (2024) also noted that supervised methods like MLC (and logistic regression) “are effective in flood detection and monitoring” when using labeled flood/non-flood pixels. Historical studies report MLC yields high flood-map accuracy when spectral classes are separable. One SAR/optical fusion study found overall classification accuracies of 83–100% using MLC on flood images (Aduah & Mantey, 2012). While modern ML (RF, SVM) are popular, MLC remains competitive in many flood mapping applications, achieving accuracy comparable to ANN or Random Forest on Sentinel-2 land-cover tasks (Ghayour et al., 2021). Its analytical nature and simple assumptions make it a transparent choice. Thus, for an urban flood case like Kathmandu, using MLC on Sentinel-2 (with proper training) is well-supported by literature as an effective optical classifier.

Together, the literature supports using Sentinel-2 with supervised classification when clear images are available and SAR is lacking or unusable, while noting NDWI-based maps may miss peak inundation without timely cloud-free data. Although satellite-based flood mapping brings an additional level of validation, it often does not provide the accuracy needed to calibrate models, especially in regions where damage assessment is limited by high cloud coverage or few data points (Notti et al., 2019). When recorded flood levels, debris lines, and high-water marks are available via field observations, they offer ground-truth evidence to help calibrate hydraulic model parameters. This calibration process including field observations will help to ensure that the

resulting simulated flood extents and depths do correspond well to flood extents and depths that were estimated in the real world (Wyżga et al., 2020).

2.6.1 Maximum Likelihood Classification

Maximum likelihood classification is a commonly used and extensively studied classification algorithm in remote sensing, often regarded as a fundamental pixel-based approach (Mondal et al., 2012). In this approach, a pixel is assigned to the class that has the highest probability (maximum likelihood) to it. This approach assumes that the data from each class in each band follows a normal distribution (Mondal et al., 2012). Consequently, choosing a few pixels is enough to obtain an accurate estimation of the mean vector and the covariance matrix. Moreover, as many samples as possible should be used so that the algorithm can consider the many changes in spectral features. To assess each pixel's resemblance to the designated classes, two properties of the mean vector and covariance matrix are often computed. Bayesian law is used to calculate this likelihood as follows (Richards, 2022):

$$D = \ln(a_c) - \left[\frac{1}{2} \ln(|\text{COV}_c|) \right] - \left[\frac{1}{2} (X - M_c)^T (\text{COV}_c^{-1}) (X - M_c) \right] \quad (12)$$

Where,

D = Weighted Distance (indicates the likelihood)

c = Specified Class

X = Measurement Vector of the Desired Pixel

M_c = Mean Vector of the Class c

COV_c = Covariance Matrix of the Pixels of the Class c

2.7 Calibration of Hydraulic Model Using Field Observation Data

Flood modelling guidelines emphasize calibrating HEC-RAS model to any available field data, especially in data-sparse, developing basins. Standard frequency analyses may underestimate peak discharges when an observed flood is beyond the gauged record. In such cases, practitioners adjust model inflows so that simulated water levels/extents match observed high-water marks (HWMs) or debris lines, effectively treating the historical flood as a fixed event rather than a pure probabilistic outcome.

High flood level (HFL) marks such as debris lines, wrack marks, or surveyed high-water elevations on structures are often collected in post-flood field campaigns (using GPS or total station) or even reported via citizen observations. These observed water-surface elevations at peak flow serve as calibration targets. In HEC-RAS, measured HFLs can be entered as “Observed Water Surface” values at cross-sections. Modelers then adjust parameters (notably channel/floodplain Manning’s n) so that the simulated peak water surface matches the observed marks. Wyżga et al. (2020) surveyed trash and wash lines from a 2014 flood along the Morávka River (Czech Republic) and used them in a 1D hydraulic model and then they tuned n -values until the model reproduced the observed peak stage at those sections. Similarly, engineering practice recommends calibrating HEC-RAS by comparing simulated water levels to known floodmarks or rating curves. In essence,

each observed HFL provides a data point to ensure the HEC-RAS profile passes through real flood elevations.

Several published studies have modeled floods in ungauged rivers by iteratively guessing flows and tuning Manning's n to match observed flood depths or extents. In an ungauged overflow-receiving watershed, Wang et al. (2010) estimated the design discharge using steady 1D HEC-RAS by iteratively adjusting inflow values until the simulated water surface profiles met target elevations at key control points. This trial-and-error approach effectively calibrated the peak flow based on hydraulic performance criteria in the absence of gauged data. Ghanbarpour et al. (2011) calibrated a 1D HEC-RAS model for a historical flash flood without stream gage data, using trial-and-error adjustments to the input hydrograph and Manning's n to match observed floodmarks and high-water elevations. Canada's Hydrologic and Hydraulic Procedures recommend using high-water marks to estimate flow when discharge data are unavailable, calibrating models to match known flood stages. They emphasize that extreme floods, often caused by atypical processes, should be treated separately from standard frequency analysis and require more detailed modeling, such as iterative calibration to observed flood evidence. For the Mulde River in Germany, flood modeling was conducted by Cerri (2017) without continuous flow data. A 1D HEC-RAS model was calibrated by iteratively adjusting assumed peak discharges to align simulated inundation with satellite-derived flood extents. By matching the modeled floodplain to remote-sensed water masks, a credible peak flow estimate was inferred despite the absence of gauge data. Oucherif and Benmamar (2017) calibrated HEC-RAS in an ungauged desert basin using regional regression estimates of the 100-year flood discharge. A steady-flow simulation was performed, and Manning's n values were adjusted through trial and error to match GPS-surveyed high-water marks from the October 2008 flood. The calibration yielded optimal n values and discharge that closely reproduced observed flood elevations. Psomiadis et al. (2020) modeled an ungauged flood in Greece using 1D HEC-RAS, running multiple simulations with varying peak discharges. Lacking gauge data, they iteratively adjusted the inflow until the simulated inundation best matched the flood extent observed via satellite imagery. Gholami (2022) used a 1D HEC-RAS model of an ungauged watershed. Without measured flows, they increased the peak discharge in steps and adjusted Manning's n until the simulated flood depths matched field-measured floodmarks on trees. Adhikari et al. (2023) used a steady-flow 1D HEC-RAS model without measured discharge data, starting with assumed roughness values and iteratively adjusting Manning's n through trial and error to match observed high-water marks. By iteratively adjusting the discharge and Manning's n values, researchers have successfully bridged the gap between observed flood extents and simulated model results, thereby enhancing the accuracy of flood predictions even in the absence of direct flow measurements.

2.8 Catchment Area Ratio (CAR) Method

In numerous mountainous and remote areas, there is no good streamflow data because there are no gauging stations. Therefore, it can be difficult to conduct hydrologic modeling as it relates to inflows (necessary to conduct hydraulic simulations). Researchers may implement indirect estimating procedures such as Catchment Area Ratio (CAR) method which is used for estimation of flows in ungauged basins based on use of flows from gauged watersheds (Yang et al., 2019). Interestingly, this type of estimating is applied not simply to ungauged river basins, but also to

multiple locations at multiple points along a river system in the estimation of flow, at least several tributaries along with the main channel which allows spatially distributed flow estimation at various levels in the watershed. This is the case in areas experiencing extreme localized rainfall events, like Nepal, and extreme terrain making it difficult to collect conventional data (Fasipe & Izinyon, 2021).

The study done by Acharya and Joshi (2020) presents different methods that can be employed to analyze flood frequency in ungauged mountainous rivers, where discharge data from similar catchments are accessible. Yang et al. (2019) explored the usage of a new method that coupled the unmanned aerial vehicle (UAV) data with the classical slope-area method to calculate river discharges in typical ungauged catchments. UAV data is used to obtain topographic information of the river channels. Li et al. (2019) developed a combined method that integrates the parameter transfer method (based on similarity in catchment characteristics) with the drainage area ratio method to improve the accuracy of continuous runoff estimation in ungauged catchments. Their study used the ‘Xinanjiang’ hydrological model and tested the combined approach across several catchments in China. According to Basnet et al. (2018), here are different approaches to estimate the flow of ungauged rivers and it is up to the individual to choose a suitable method among those available methods. Nevertheless, it is crucial to understand the specific parameters of the chosen method (e.g., rainfall, surface characteristics of the catchment, steepness of the basin), as they greatly influence the results. However, all these methods rely on different assumptions. The selected method might lead to unreliable results if the parameters and assumptions are not considered well. With the review of multiple literatures, Catchment Area Ratio (CAR) method is generally and more typically used because of its simplicity and good enough results that are obtained after validation.

Accurate estimation and modeling of water availability and quality for water supply and ecological assessment necessitates reliable estimation of flow. In the past, estimating flow rates in ungauged catchments has involved using different methods. One of the most commonly used methods for estimating daily flow in a catchment without a gauge is the watershed area ratio technique. The area ratio method is employed to calculate flow in an ungauged catchment when a nearby gauged watershed is available as a reference. The method estimates flow at an ungauged location by multiplying the measured flow at the nearby reference gage by the area ratio of the ungauged to gauged watershed. Discharge of ungauged river is calculated using the formula below:

$$Q_2 = \frac{A_2}{A_1} * Q_1 \quad (13)$$

Where,

Q_2 = Discharge of a Concerned point

Q_1 = Discharge of the Reference Point

A_2 = Area of a Concerned Catchment

A_1 = Area of the Reference Catchment

This method of discharge calculation is suitable when the discharge data of watershed with similar is available nearby. A major assumption of the catchment area ratio method is that the flow is the function of watershed area only. Flow rate of ungauged catchment is assumed proportional to the watershed area. This approach is employed not only for estimating discharge in ungauged river basins, but also at multiple locations along a river system, particularly where tributaries converge with the main channel, thereby enabling spatially distributed flow analysis throughout the watershed (Fasipe & Izinyon, 2021)

2.9 Research Gap and Rationale for Integrated Approach

In the last few years, researchers worldwide have begun using integrated flood modeling frameworks using hydrologic models (such as HEC-HMS), hydraulic models (such as HEC-RAS), high-resolution terrain data from obtained using UAVs, remote sensing images for validation, and some additional field-based calibration. Peker et al. (2024c) generated hazard maps in Türkiye using the calibrated HEC-HMS model with 2D HEC-RAS and a 5 m Digital Elevation Model (DEM). Peker et al. (2024a) used photogrammetry from UAVs to create local DEMs ranging from 1-30 m in resolution for a 20 km river segment and found that model outputs using the 1 m UAV DEMs had, on average, about 92% correspondence to flood extents, using water surfaces captured from satellite- and UAV-based observations, while Global DEMs such as SRTM, ASTER etc. had errors greater than 1 m in depth and greater than 17% in extents. Huang and Jin (2020) also generated high fidelity 2D flood simulation in Taiwan, using UAV-based DEM and HEC-HMS that was calibrated with an NSE greater than 0.88. Darji et al. (2024) modeled a dam breach, using a DJI drone-derived 10 cm DEM, calibrating the HEC-RAS outputs against field benchmarks. At the same time, there are users that wish to differentiate themselves from modeling and use remote sensing that has itself become a standard with regard to flood mapping and validation- such as supervised classification of Sentinel-2. For instance, Afzal et al. (2022b) compared water depths from HEC-RAS simulations with flood extents outlined from images processed from Satellite Sentinel-1/2 with classification Kappa index of about 90%. Together, these cases underscore that combining UAV topography, HEC modeling, and satellite validation can dramatically enhance model accuracy and credibility, especially in areas with limited ground data.

While there has been some progress, the level of development of fully integrated studies in Nepal, particularly for the KVW, has been slightly slower. Many have relied on global DEMs such as SRTM, ALOS etc. which can be coarse at larger scales, found synthetic hydrographs, or not calibrated models. For example, Dangol and Bormudoi (2015) developed a 1D HEC-RAS model for the Bishnumati River but did not use UAV data or observed flood marks. Shrestha et al., 2023) produced a flood map of Kathmandu from a 10 m resolution only from optical imagery, but did not reference or fit the results to outputs of a model or to field data. Further, according to Watson et al. (2024), publicly accessible flood maps of Kathmandu are based on 90 m DEMs, which is too coarse for planning at the urban scale and often includes artificial depressions which will generate large over-estimates of inundation. Chaulagain et al. (2023b) generated flood susceptibility maps for Kathmandu using a GIS-based MCDA approach but did not use high-resolution DEMs or validate results with observed flood extents. Hence, based on review of available literatures, some of these models are described as not validated and others overly reliant on default parameter settings.

To address these methodological gaps, our study implements a fully integrated, high-resolution flood modeling framework, that is applied to the Bagmati–Nakkhu confluence. The hydrologic component combines long-term peak discharge records from the Department of Hydrology and Meteorology (DHM) for the Bagmati River with simulated hydrographs for the ungauged Nakkhu River using HEC-HMS. Discharges were estimated for various return periods (5, 10, 25, 50, 100 and 150) with the Gumbel distribution. A DEM with sub-meter resolution was developed using UAV photogrammetry, allowing high-resolution topography input to HEC-RAS. The hydraulic model was calibrated to observed high flood level (HFL) locations from the 27 September 2024 flood event, and followed global best practice procedures similar to Clasing et al. (2023) and Parizi et al. (2022a). For validation, Sentinel-2 post-flood optical imageries were classified using the Maximum Likelihood Classification to create observed flood extents as outlined in works of Hirpa et al. (2023) and Huang and Jin (2020), which were compared to the simulated results. Unlike other studies conducted in Kathmandu, this study utilizes all five parts viz. hydrologic modeling using HEC-HMS, UAV-derived DEM, calibration in the field, HEC-RAS simulation, and satellite validation, in one workflow. This presents a valid and replicable model for urban flood hazard mapping in data-poor environments, and responds directly to the identified need in Nepal for high-resolution, calibrated, and validated modeling frameworks (Watson et al., 2024).

3 METHODOLOGY

3.1 Study Area

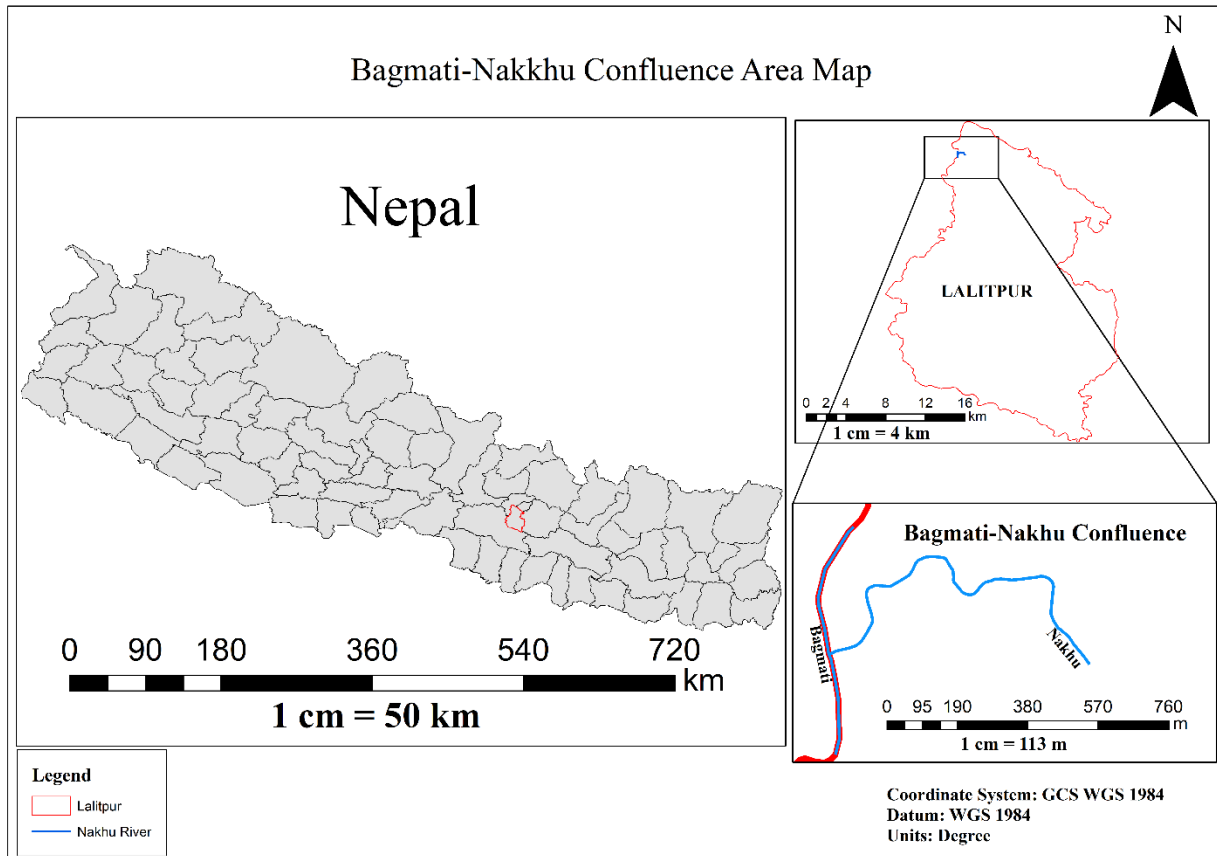


Figure 1: Study Area

3.2 Instrument Used

1. DJI Phantom 4 (UAV)
2. Emlid Reach 2 (GNSS Receiver)

3.3 Softwares Used

1. ArcGIS
2. ENVI
3. Global Mapper
4. Google Earth Engine
5. HEC-HMS
6. HEC-RAS
7. Pix4D
8. QGIS

3.4 Data Used

Table 1: Data used and its sources

Data	Data Source	Date Range	Resolution
Sentinel 2 Optical Imagery	Copernicus Data Space Ecosystem	October 01 2024	10m
DEM	Obtained from UAV	April 26/27 2025	50m
Land Cover	Dem obtained from UAV	April 26/27 2025	50m
Discharge of River	Department of Hydrology and Meteorology	1993-2024	-
Water Level	Department of Hydrology and Meteorology	1993-2024	-
Flood Marks	Rtk Survey	May 07 2024	-
Rainfall (Point Data)	NASA POWER	2000-2024	-

3.5 Conceptual Framework

The conceptual framework of this study integrates field-based observations, UAV-derived topographic data, satellite imagery, and hydrologic-hydraulic modeling to simulate flood inundation and generate hazard maps for the Bagmati-Nakkhu confluence. As illustrated in Figure 2, the framework begins with the collection of primary data from field surveys, UAVs, and satellite remote sensing. Hydrologic modeling using HEC-HMS estimates discharge for the Nakkhu River, while observed discharge data for the Bagmati River is obtained from the Department of Hydrology and Meteorology (DHM). These discharge datasets are jointly input into the HEC-RAS hydraulic model to simulate flood extents. The model results are validated using field-measured flood marks and satellite-derived flood extent through supervised classification. Finally, GIS-based spatial analysis is conducted to generate flood depth and hazard maps, which guide recommendations for zoning, infrastructure resilience, and wetland conservation.

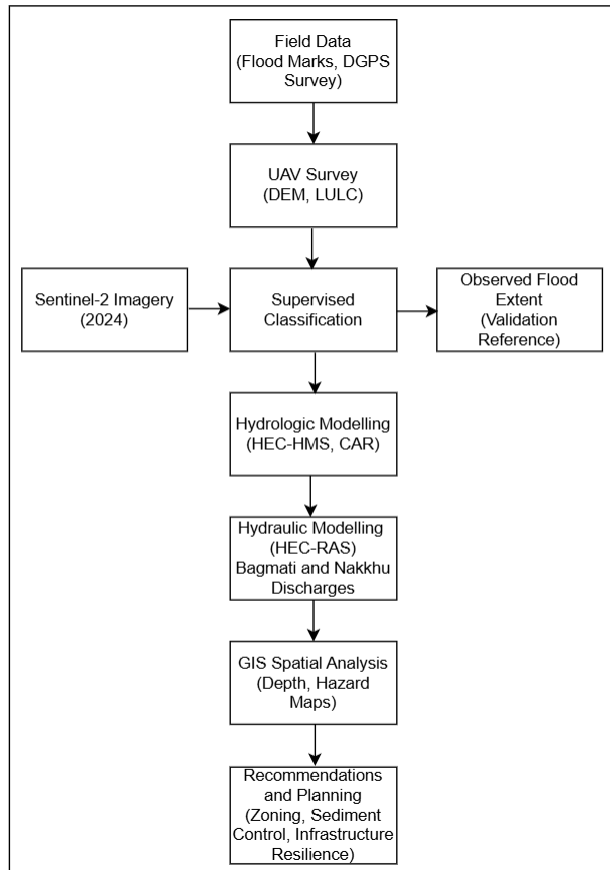


Figure 2: Conceptual Framework Workflow

3.6 Methodological Workflow

To achieve accurate flood hazard mapping and inundation modeling for the Bagmati-Nakkhu confluence, a multi-source and multi-stage workflow was developed. The methodology integrates field-collected flood marks, UAV-derived topographic data, and satellite imagery with hydrological and hydraulic models (HEC-HMS and HEC-RAS). Peak discharges are estimated from both ground stations and simulations, followed by flood modeling for various return periods. Outputs from HEC-RAS are validated using classified satellite imagery and ground truth points. GIS is used throughout to prepare land use maps, process remote sensing data, and produce final flood hazard outputs. The complete workflow is illustrated in Figure 2.

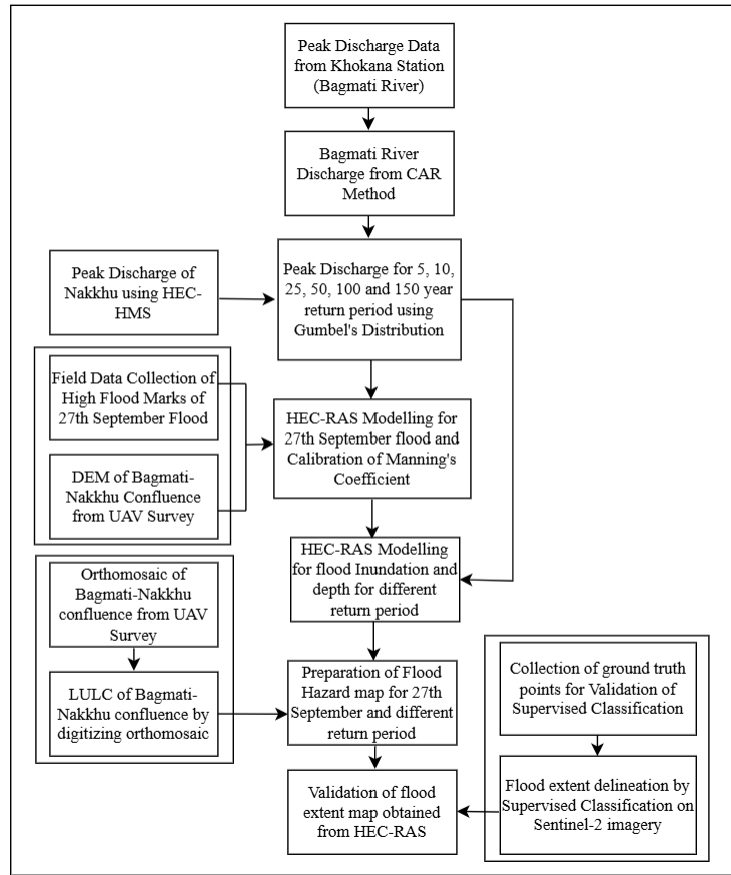


Figure 3: Methodological Workflow

3.6.1 Supervised Classification

Supervised classification was used to delineate flood-affected and non-flooded areas within the Bagmati-Nakkhu confluence using Sentinel-2 imagery dated October 1, 2024. This classification aimed to generate a binary flood extent map using ENVI software. The steps undertaken in the classification process are detailed below.

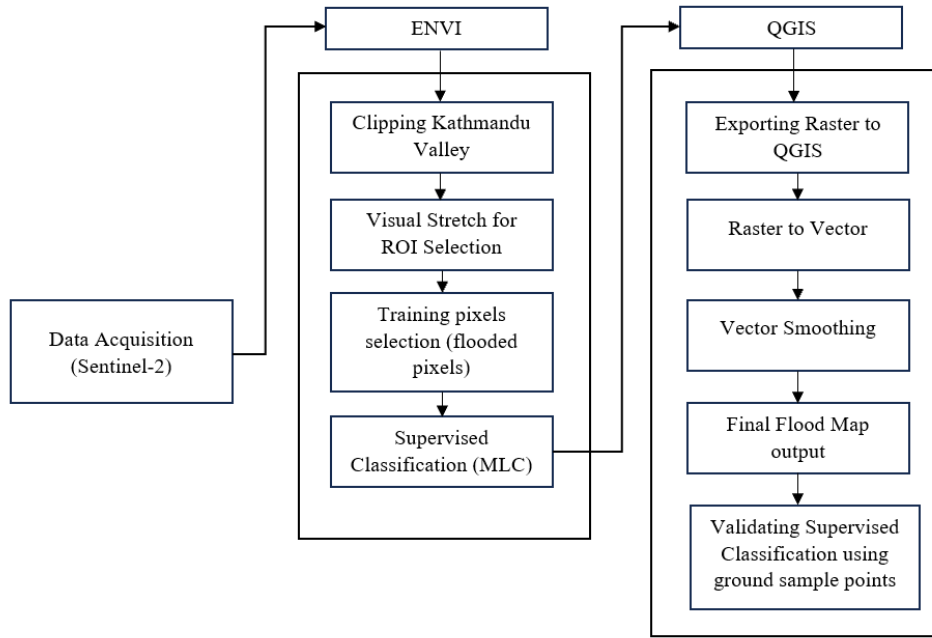


Figure 4: Flood Delineation Using Supervised Classification Workflow

3.6.1.1 Satellite Image Acquisition

A Level-1C Sentinel-2 image captured on October 1 2024 was obtained from the Copernicus Open Access Hub. This date was selected based on flood event on September 26th to 28th, indicating that significant flooding had occurred in the study area just three days prior. The image provided high-resolution data (10–20 m) across various bands. Key bands used for flood classification included: Band 2 – Blue (10 m), Band 3 – Green (10 m), Band 4 – Red (10 m), and Band 8 – Near-Infrared (NIR, 10 m).

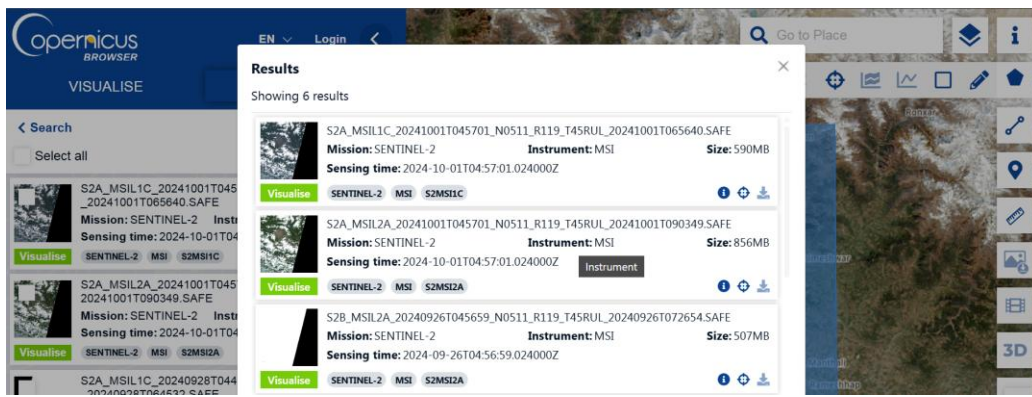


Figure 5: Copernicus Browser

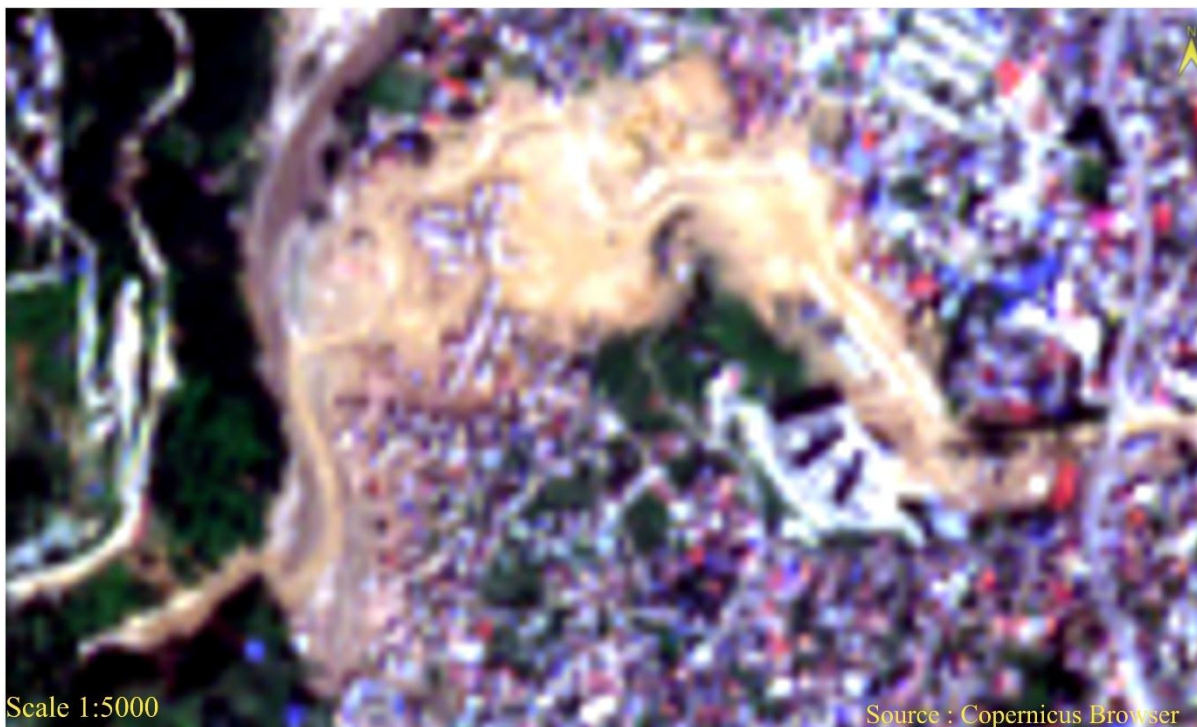


Figure 6: Sentinel imagery of Confluence area

3.6.1.2 Pre-processing

Pre-processing was carried out using ENVI software and consisted of several steps. First, band stacking was performed, where individual spectral bands were stacked to create a multispectral composite image suitable for classification analysis. Next, clipping to the Region of Interest (ROI) was done to limit the processing area to the Bagmati-Nakkhu confluence and the surrounding flood-prone regions. Finally, a visual quality check was conducted to manually inspect cloud cover and shadow presence. The selected image was mostly cloud-free and therefore deemed suitable for further analysis.

3.6.1.3 Training Sample Selection

As the satellite image was acquired three days after the peak flooding event, many areas that were initially inundated had begun to dry. Consequently, flooded zones were not always visibly covered by standing water but were instead inferred from indicators such as increased soil moisture and residual surface saturation.

To ensure accurate classification, training samples were carefully delineated. Flooded area samples were identified based on the presence of sediment deposits and moist soil patches observable near water bodies in the imagery. In contrast, non-flooded area samples were selected from locations characterized by ground conditions, elevated terrain, vegetation, and urban infrastructure that exhibited no visual evidence of flooding.

These samples were defined as Regions of Interest (ROIs) within the ENVI software environment and were subsequently validated using ground truth data obtained from field photographs.

3.6.1.4 Classification Using Maximum Likelihood

The classification was performed using the Maximum Likelihood Classifier (MLC) in ENVI. This algorithm was chosen because it effectively distinguishes spectrally similar classes by considering the variance-covariance structure of the input data. The output raster was a binary classified flood map reflecting the spatial distribution of flood extent with two primary classes: Flooded and Non-Flooded.

3.6.1.5 Accuracy Assessment

To ensure the accuracy of the flood extent delineated from remote sensing data, a field survey was conducted in the Bagmati–Nakhu confluence area. The objective was to collect ground truth data regarding the maximum extent of the September 2024 flood, which would later serve as a reference for validating the classified flood extent map derived from Sentinel-2 imagery.

The field survey involved the use of Emlid GNSS equipment, comprising a base station and a rover unit operating in RTK (Real-Time Kinematic) mode. The process began with the establishment of a control point in the study area, where the base station was set up. Once the base station was operational and transmitting corrections, the rover was connected to receive these corrections in real-time, enabling centimeter-level positional accuracy.

With the rover in hand, the field crew traversed the flood-affected area and recorded x, y, z coordinates at multiple locations identified as the outermost points reached by the floodwaters. These points were selected based on visible flood marks, sediment deposits, and information provided by local residents who witnessed the flood event.

The data points were later overlaid on the flood extent map generated through supervised classification of Sentinel-2 satellite imagery, to check how accurately it matched real ground conditions.

To validate the classification, 125 ground-truth points were used: 80 points for flooded areas and 45 points for non-flooded areas. These were collected during post-flood fieldwork.

Confusion Matrix:

Table 2: Confusion Matrix

Reference / Ground Truth	Predicted: Flooded	Predicted: Non-Flooded	Total
Flooded	75 (True Positive)	5 (False Negative)	80
Non-Flooded	3 (False Positive)	42 (True Negative)	45
Total	78	47	125

Classification Accuracy Metrics

True Positives (TP) = 75

True Negatives (TN) = 42

False Positives (FP) = 3

False Negatives (FN) = 5

Total Correct Predictions = 117

Total Validation Points = 125

Overall Accuracy (OA):

$$\begin{aligned} &= (\text{TP} + \text{TN}) / \text{Total} \\ &= (75 + 42) / 125 \\ &= 93.6\% \end{aligned}$$

Recall (Sensitivity):

$$\begin{aligned} &= \text{TP} / (\text{TP} + \text{FN}) \\ &= 75 / 80 \\ &= 93.75\% \end{aligned}$$

Precision (User's Accuracy for Flooded):

$$\begin{aligned} &= \text{TP} / (\text{TP} + \text{FP}) \\ &= 75 / 78 \\ &= 96.15\% \end{aligned}$$

F1 Score:

$$\begin{aligned} &= 2 \times (\text{Precision} \times \text{Recall}) / (\text{Precision} + \text{Recall}) \\ &\approx 94.9\% \end{aligned}$$

Kappa Coefficient (κ):

$$\text{Observed agreement (Po)} = 117 / 125 = 0.936$$

$$\text{Expected agreement (Pe)} = [(78 \times 80) + (47 \times 45)] / 125^2 = 8355 / 15625 \approx 0.5347$$

$$\text{Kappa } (\kappa) = (\text{Po} - \text{Pe}) / (1 - \text{Pe}) = (0.936 - 0.5347) / (1 - 0.5347) \approx 0.86$$

The classification results were highly accurate, with an Overall Accuracy of 93.6% and a Kappa coefficient of 0.862, indicating nearly perfect agreement between the classified map and reference data. The Recall of 93.75% indicates that the majority of the actual flooded areas were correctly identified, whereas the Precision of 96.15% confirms that the majority of the predicted flooded areas were actually flooded on the ground. The F1 Score of 94.9% demonstrates the classification's validity in accurately detecting flooded areas.

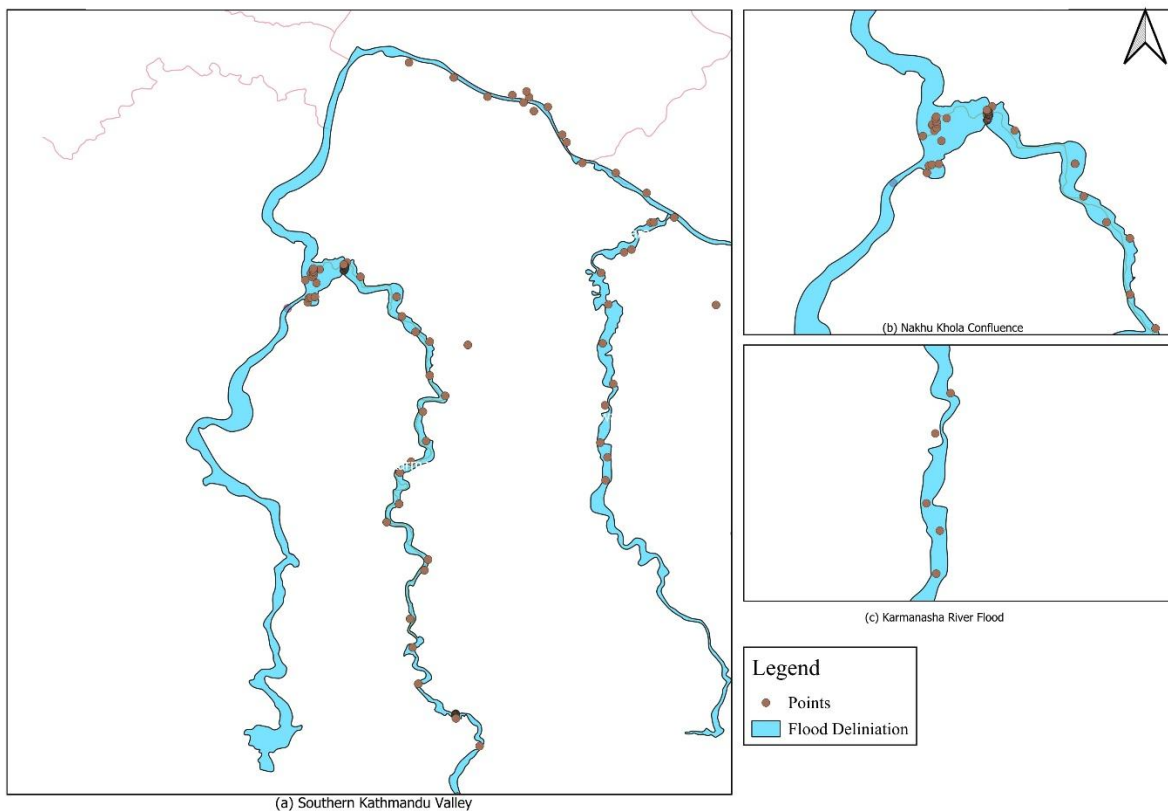


Figure 7: Flood Delineation and Validation

3.6.1.6 Post-Processing

To improve the interpretability and presentation of the classified output, a series of post-processing steps were implemented.

First, the classified raster image was converted into vector format to facilitate further spatial analysis. Subsequently, only the ‘Flooded’ class was extracted, as the primary objective of the study was to delineate and analyze flood-affected areas; the ‘Non-Flooded’ class was excluded from the final map.

Following this, vector smoothing was applied to the extracted flood polygons to eliminate irregular boundaries and enhance cartographic quality.

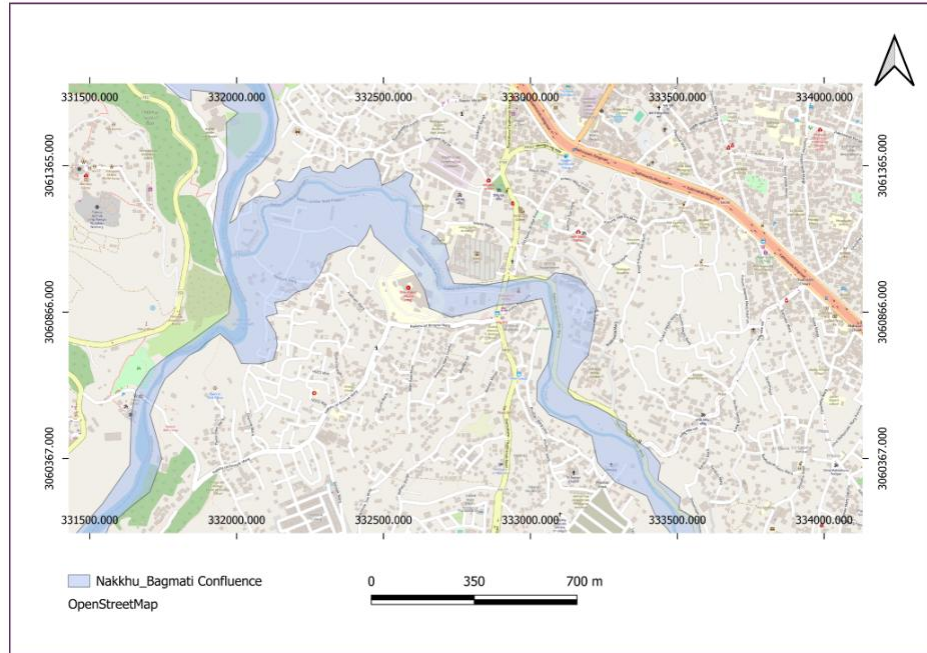


Figure 8: Flood Extent Map

3.6.2 DEM and Orthomosaic Generation from UAV Survey

3.6.2.1 UAV Flight Operation Workflow

To generate high-resolution topographic datasets such as the orthophoto, Digital Elevation Model (DEM) and Digital Surface Model (DSM), a UAV survey was carried out over the Bagmati–Nakhu confluence area. The survey was conducted using a DJI Phantom 4 RTK drone, which is equipped with an onboard RTK module for improved positional accuracy. For RTK correction, an Emlid Reach RS2 unit was used as a static base station. The UAV itself functioned as the RTK rover, receiving corrections from the base in real time.

The field setup began by establishing the Emlid base station at a fixed control point in the survey area. Once the base was set up and transmitting RTK corrections, the UAV was configured and launched along a pre-programmed flight path. The drone followed a grid-based pattern and captured geotagged images with centimeter-level accuracy. The mission was fully autonomous, and the flight was conducted under clear weather conditions to ensure data quality. Throughout the operation, image capture was automated based on pre-defined intervals and overlaps.

Table 3: UAV Flight Specification

Parameter	Value
Camera Type	FC6360_5.7
Forward Overlap	75%
Side Overlap	65%
Flight Altitude	58 meters above ground
Total Flight Duration	4 hour 27 minutes
Total Number of Images Captured	2167
Coordinate System	WGS 84
Survey Time Frame	4/26/2025 - 4/28/2025

3.6.2.2 Image Processing in Pix4D Mapper

The collected images were processed using Pix4D Mapper. The initial processing involved automatic image alignment, key point extraction, and internal camera calibration. The coordinate system used for processing was UTM Zone 45N. Ground Control Points (GCPs) collected during field surveys were incorporated to georeference the project accurately. A dense point cloud was then generated using structure-from-motion techniques, followed by the creation of a high resolution orthophoto and a Digital Surface Model (DSM).

Table 4: Geolocation Error Table

Min Error [m]	Max Error [m]	Geolocation Error X [%]	Geolocation Error Y [%]	Geolocation Error Z [%]
-	-8.49	0.00	0.00	0.00
-8.49	-6.79	0.00	0.00	0.00
-6.79	-5.10	0.00	0.00	0.00
-5.10	-3.40	0.19	0.28	0.00
-3.40	-1.70	0.33	3.45	0.00
-1.70	0.00	46.78	48.42	41.85
0.00	1.70	51.12	45.90	46.09
1.70	3.40	1.58	0.51	0.00
3.40	5.10	0.00	1.44	0.00
5.10	6.79	0.00	0.00	0.05
6.79	8.49	0.00	0.00	0.09
8.49	-	0.00	0.00	0.00

Mean [m]	0.067636	-0.053239	1.526097
Sigma [m]	0.438793	0.762719	1.127607
RMS Error [m]	0.443975	0.764575	1.400694

Over 97% of geolocation errors in the X and Y directions fall within the range of ± 1.7 meters, indicating high horizontal accuracy.

The vertical (Z-axis) accuracy, while slightly more variable, remains within ± 1.7 meters for nearly 88% of the dataset.

The minimal occurrence of outliers ($> \pm 3.4$ m) reflects the robustness of RTK correction and GCP referencing during processing.



Figure 9: Ortho mosaic of Study Area

3.6.2.3 Point Cloud Classification in ENVI LiDAR

The dense point cloud from Pix4D was exported in LAS format and imported into ENVI LiDAR for classification. ENVI LiDAR automatically categorized the points into several classes, including ground, vegetation (low, medium, high), buildings, and high objects such as poles. Manual correction was performed where necessary to refine misclassifications. Accurate classification of ground points was essential for terrain modeling.

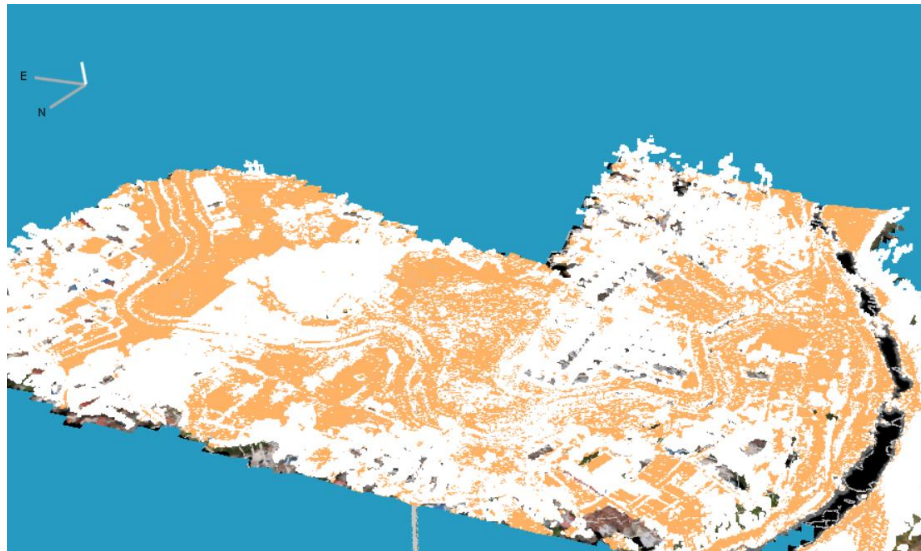


Figure 10: Point Cloud Classification

3.6.2.4 DTM and DSM Generation in ENVI LiDAR

Both Digital Terrain Model (DTM) and Digital Surface Model (DSM) were generated using ENVI LiDAR. The DSM was derived from all first return points, capturing features such as buildings and vegetation. The DTM was generated using only ground-classified points, representing the bare-earth surface. Both models were produced at a spatial resolution of 0.5 meters and exported as GeoTIFF files for further analysis.

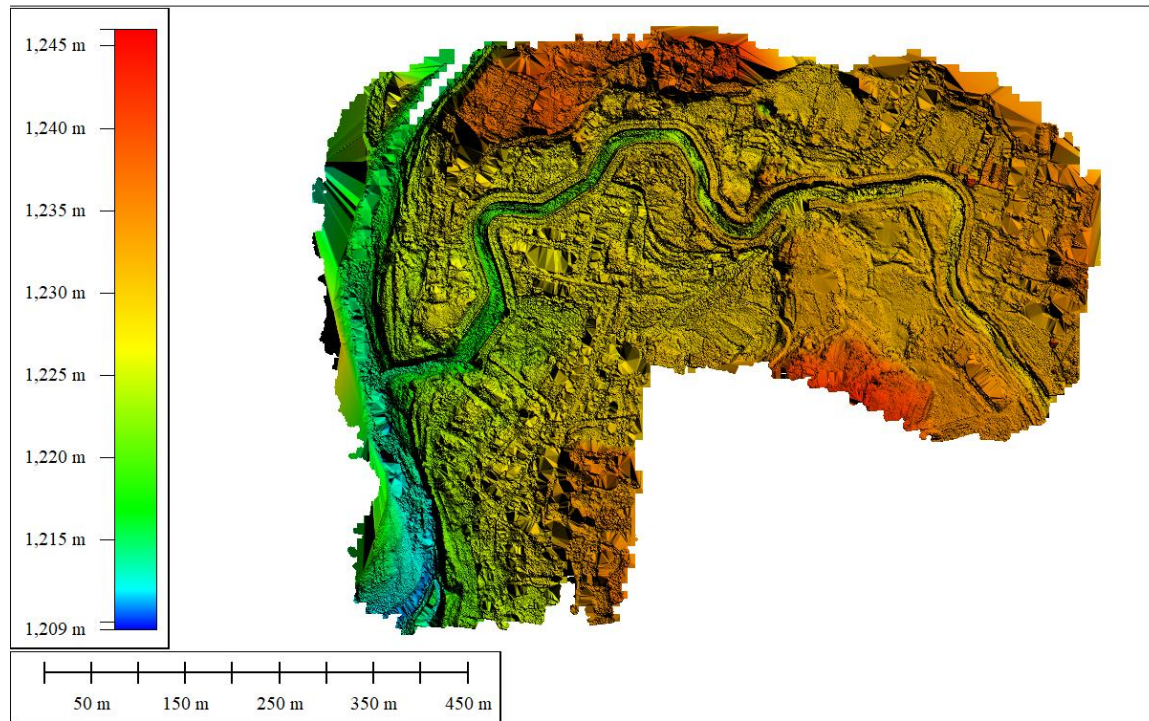


Figure 11: Digital Terrain Model



Figure 12: Digital Surface Model

3.6.2.5 Preparation of Land Cover Map of Study Area

Using high-resolution orthophotos generated from drone flights, various surface features such as built-up areas, water bodies, forests, and bare ground can be clearly identified based on their color, texture, and shape. These features are then outlined and classified using GIS software, resulting in a detailed map that represents the distribution of different land cover types within the study area.

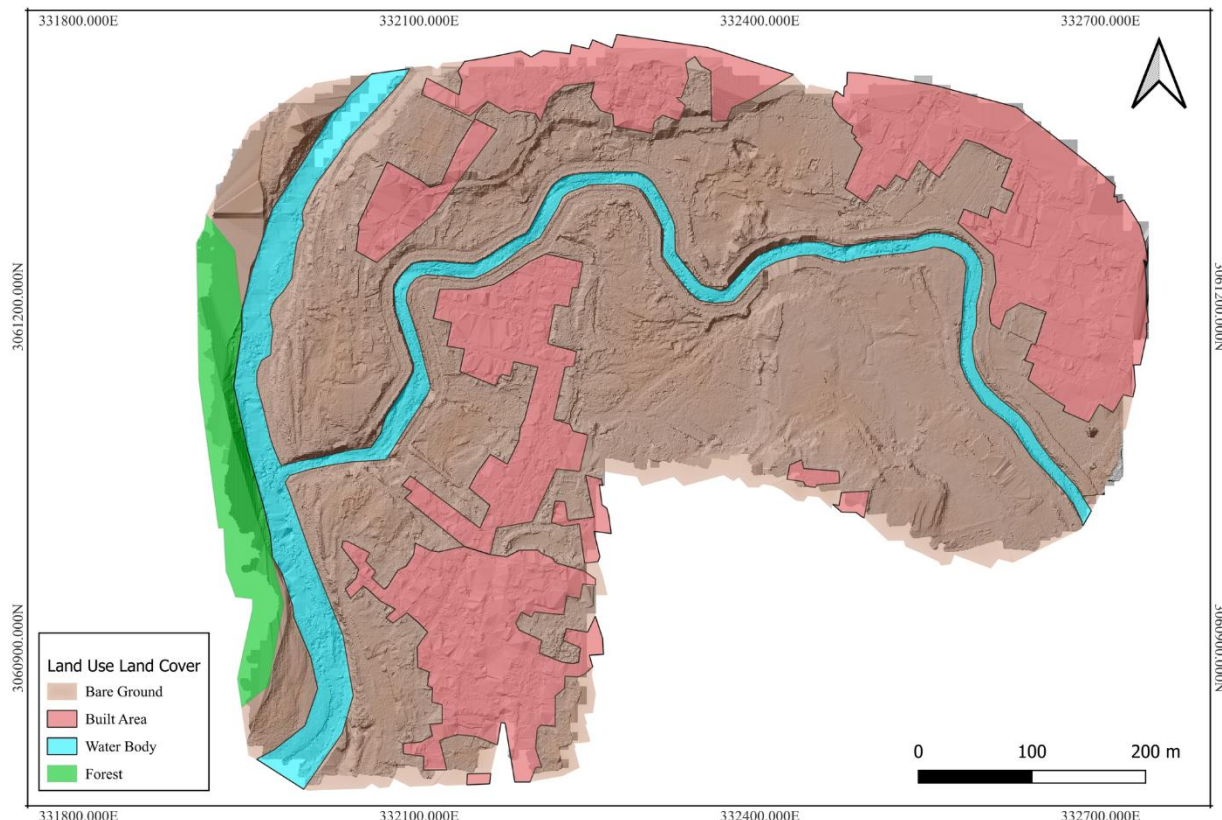


Figure 13: Land Cover of Study Area

3.6.3 Hydrologic Modeling Using HEC-HMS and the Catchment Area Ratio (CAR) Method

Hydrologic modeling for the Nakkhu River basin was carried out using the Hydrologic Engineering Center's Hydrologic Modeling System (HEC-HMS), version 4.12. The primary objective was to estimate peak discharge at the Nakkhu Breakpoint which is the farthest upstream point of the Nakkhu River covered by the Digital Elevation Model (DEM). Peak discharge values were simulated for a 25-year period (2000–2024) using rainfall data obtained from NASA's Prediction of Worldwide Energy Resources (POWER) dataset.

For the Bagmati River, peak discharge records were available from the Department of Hydrology and Meteorology (DHM) at the Khokana hydrological station, located approximately 3 kilometers south of the study area. However, to estimate the peak discharge for various return periods at multiple points along the Bagmati River within the study area, the Catchment Area Ratio (CAR) method was employed. This method allowed for the extrapolation of peak discharge based on the ratio of catchment areas between the known (Khokana) and target locations.

Catchment delineation and area calculations for all relevant points were performed using the HEC-HMS interface due to its user-friendly capabilities. For this purpose, the ALOS PALSAR Digital Elevation Model (DEM) with 12.5-meter spatial resolution was utilized. The DEM data was obtained from the Alaska Satellite Facility Distributed Active Archive Center (ASF DAAC) and downloaded via the ASF Vertex data portal.

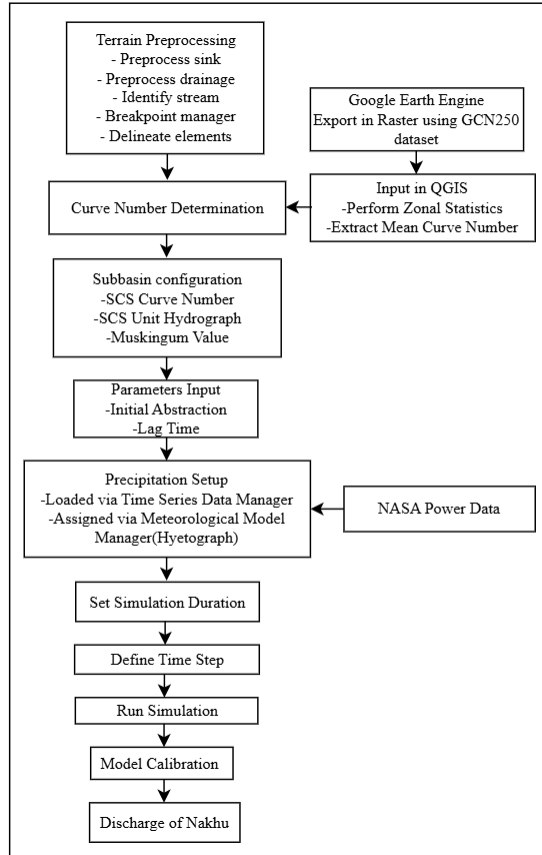


Figure 14: Methodological Flowchart for HEC-HMS

3.6.3.1 Basin Model Setup

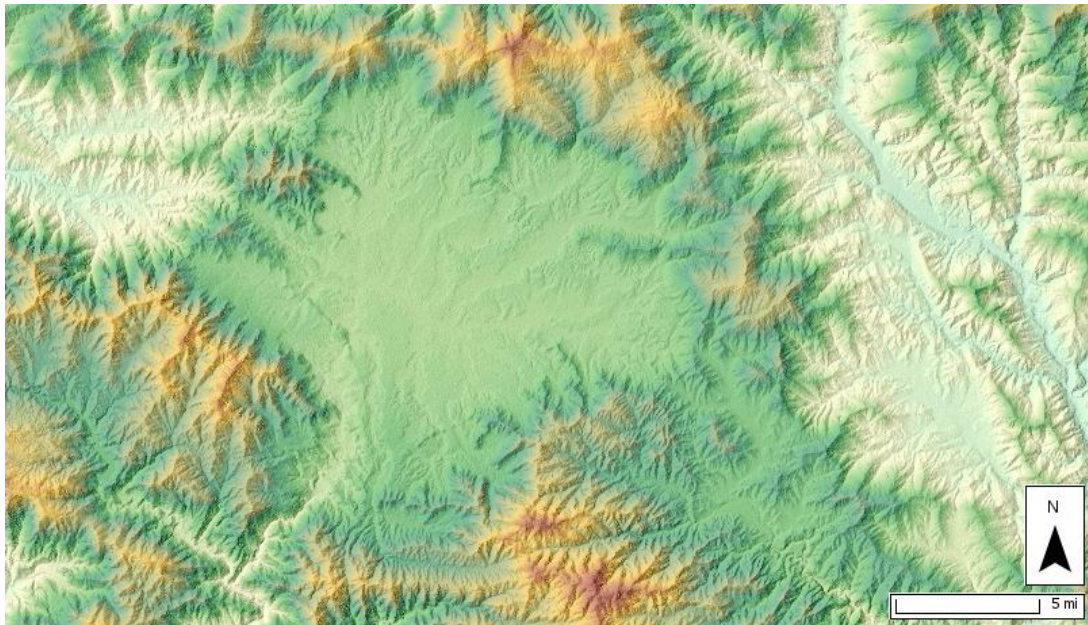


Figure 15: ALOS PALSAR DEM of the Study Area

The modeling process in HEC-HMS began with the creation of a Basin Model representing the Bagmati and Nakkhu catchments. A Terrain Model was then created by importing the ALOS PALSAR 12.5 m DEM, downloaded from the ASF Vertex portal. The DEM was assigned to the basin model, and its coordinate reference system was specified to ensure accurate georeferencing. Once configured, the terrain was successfully visualized in the HEC-HMS interface for further hydrologic analysis.

3.6.3.2 Terrain Preprocessing and Watershed Delineation

After setting up the terrain in HEC-HMS, GIS preprocessing steps were carried out to prepare the model for watershed delineation. This included sink preprocessing to remove artificial depressions in the DEM, drainage preprocessing to establish flow direction and accumulation patterns, and stream identification using a minimum contributing area threshold of 10 km². A shapefile representing the Nakkhu Breakpoint, digitized from the DEM and satellite imagery overlay, was added using the Breakpoint Manager to define the outlet of the watershed. With the breakpoint in place, the “Delineate Elements” function was used to automatically generate hydrologic components such as sub-basins, junctions, and reaches, completing the delineation process. Three sub-basins (S1, S2, S3), one junction (J1) and one reach (R1) were delineated.

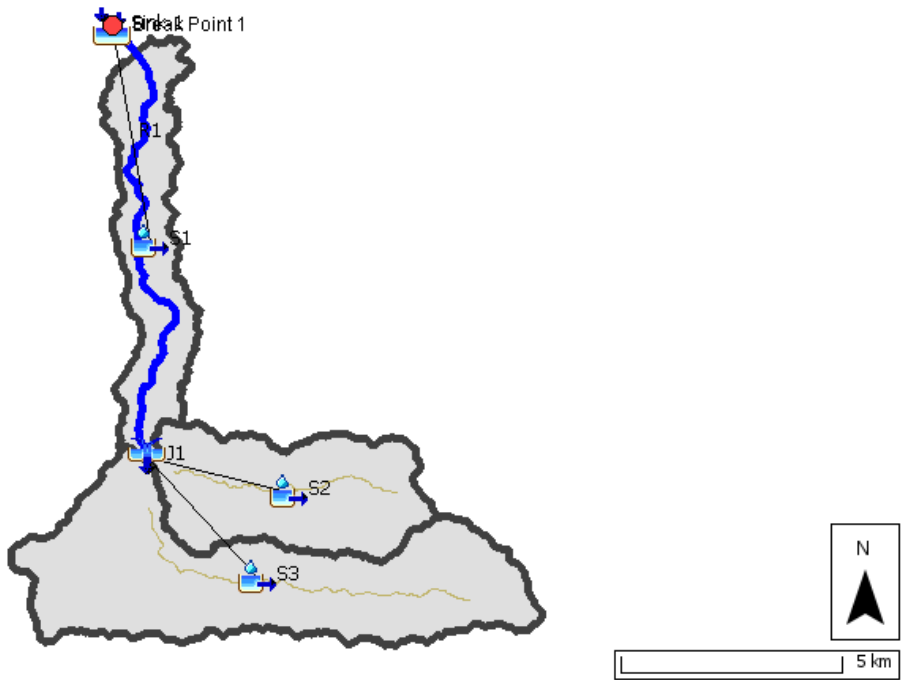


Figure 16: Delineated Elements for Nakku Breakpoint

3.6.3.3 Model Parameterization and Method Selection

Following watershed delineation, the hydrologic parameters and computational methods were configured in the HEC-HMS program settings. The SCS Curve Number method was selected as the loss method for all sub-basins to estimate infiltration losses. For runoff transformation, the SCS Unit Hydrograph method was applied uniformly across all sub-basins. Muskingum routing was used as the reach routing method to simulate flow through river reaches. Additionally, the Specified Hyetograph method was chosen to define precipitation input for each sub-basin.

3.6.3.4 Hydrologic Parameters Assignment

Following the selection of hydrologic methods, parameter values were assigned for each component of the model. For the SCS Curve Number (CN) loss method, values for initial abstraction, impervious area percentage, and CN were specified for each sub-basin. The initial abstraction was estimated as 20% of the potential maximum retention (S), in accordance with standard SCS guidelines. The impervious percentage was calculated by dividing the built-up area by the total sub-basin area, using 10-meter resolution Sentinel-2 land use/land cover (LULC) data provided by ESRI. Curve Numbers for each sub-basin were determined using the GCN250 method developed by Jaafar et al. (2019), which integrates soil and land cover data at a spatial resolution suitable for regional-scale modeling.

For the SCS Unit Hydrograph transform method, lag time was calculated for each sub-basin based on the longest flow path length, average basin slope, and the Curve Number, following SCS empirical formulations.

For reach routing, the Muskingum method was applied. Initial estimates of the Muskingum parameters were set as $K = 0.5$ hours and $X = 0.25$ for the main river reach (R1), with the expectation of refinement during model calibration.

3.6.3.5 Precipitation Input Configuration

To provide rainfall input to the hydrologic model, three precipitation gages viz. Gage 1, Gage 2, and Gage 3, were created using the Time-Series Data Manager in HEC-HMS. For each gage, a daily time interval was specified, with a start date of January 1 and an end date of December 31, covering a full annual cycle. Daily precipitation data for each gage was sourced from NASA's Prediction of Worldwide Energy Resources (POWER) dataset, which provides gridded, satellite-derived meteorological data. The rainfall time series for each gage was inputted manually to represent the spatial variability of rainfall across the study area.

3.6.3.6 Meteorologic Model Setup

Within the Meteorologic Model Manager of HEC-HMS, a meteorologic model was created to link precipitation inputs with the hydrologic elements. Each sub-basin was assigned a corresponding precipitation gage based on spatial distribution: Gage 1 and Gage 2 were assigned to sub-basin S2, while Gage 3 was assigned to sub-basin S3.

3.6.3.7 Control Specifications Setup

A control specification was created using the Control Specifications Manager in HEC-HMS to define the simulation period and time step. The start date, end date, and a time interval of 1 day were specified to align with the temporal resolution of the precipitation data and to ensure consistency across all components of the model. This configuration governed the execution timeline for all hydrologic simulations within the project.

3.6.3.8 Simulation Execution

A simulation run was created in HEC-HMS by linking the previously defined basin model, meteorologic model, and control specification. Upon execution, the model generated a summary report containing daily discharge values for each day of the year, as well as the peak discharge for all hydrologic elements, including sub-basins, junctions, reaches, and the outlet point (Nakkhu Breakpoint).

For calibration purposes, the model was first run for the year 2022, as observed daily discharge data for the Nakkhu River during this period was available from the Department of Hydrology and Meteorology (DHM), Nepal. This allowed for direct comparison between simulated and observed discharge values, facilitating the evaluation and refinement of model performance.

3.6.3.9 Model Calibration

Following the initial simulation for the year 2022, a discharge gage (DG1) was created under the Time-Series Data Manager in HEC-HMS, incorporating daily observed discharge data for the Nakkhu River from January 1 to December 31, 2022. This discharge data, obtained from the Department of Hydrology and Meteorology (DHM), Nepal, was linked to the sink (Nakkhu Breakpoint) in the model. While the observation station was not located exactly at the modeled breakpoint, the two points share similar catchment area i.e. approximately 54 km^2 , allowing the observed data to be used reliably for calibration.

The initial simulation yielded a Nash–Sutcliffe Efficiency (NSE) value of 0.520, indicating moderate model performance. Subsequently, automatic calibration followed by manual adjustments was performed by fine-tuning parameters such as Muskingum K and X, Curve Number (CN), initial abstraction, and impervious percentage. After calibration, the NSE improved to 0.666, reflecting a good model fit. According to multiple studies, an NSE value above 0.50 is generally considered satisfactory, and a value of 0.666 demonstrates that the model achieved reliable performance in replicating observed hydrologic conditions.



Figure 17: Nash–Sutcliffe Efficiency (Before Calibration)



Figure 18: Nash–Sutcliffe Efficiency (After Calibration)

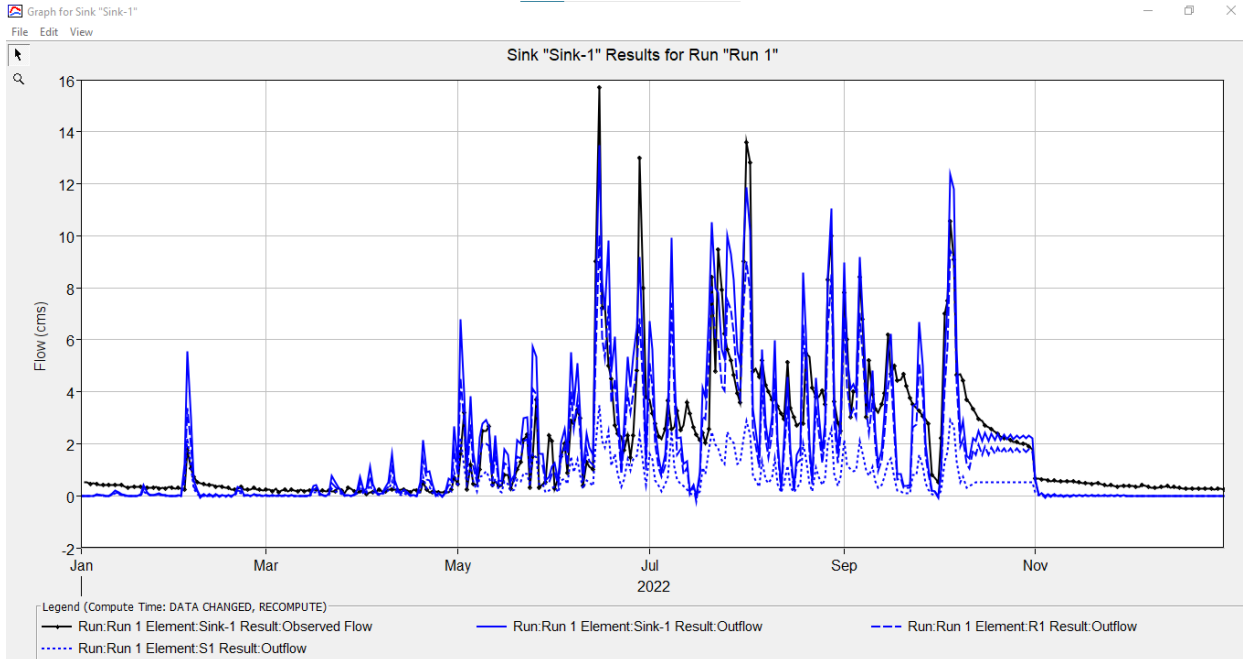


Figure 19: Observed vs Simulated Flow (After Calibration)

3.6.3.10 Model Validation and Multi-Year Simulation

After successful calibration, the model was validated by running a simulation for the year 2020 using the calibrated parameter values. The observed peak discharge for 2020 occurred on 20th July, with a recorded value of $21.4 \text{ m}^3/\text{s}$. The model simulation identified the same date for peak discharge and produced a discharge value of $25.4 \text{ m}^3/\text{s}$, indicating strong temporal agreement and validating the model's ability to reproduce observed flood events with reasonable accuracy.

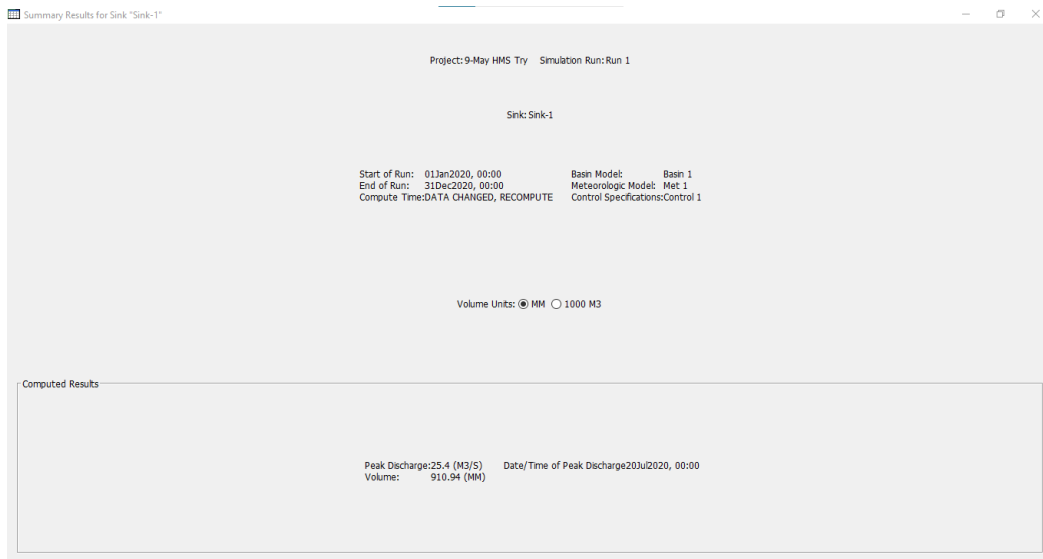


Figure 20: Validation on 2020 Observed Data

Following validation, the model was deemed suitable for simulating discharge across multiple years. By updating the start and end dates along with the corresponding rainfall data for each year,

the peak discharge values at the Nakkhu Breakpoint were successfully computed for all remaining years within the study period.

Table 5: Simulated Peak Discharge for Nakkhu Break Point

Year	Maximum Discharge (m ³ /s)
2000	25.3
2001	15.9
2002	15.1
2003	9.1
2004	21.2
2005	20
2006	15.7
2007	15.1
2008	26.8
2009	30.1
2010	15
2011	18.1
2012	28.2
2013	27.3
2014	22.1
2015	25.8
2016	15.8
2017	14.9
2018	18.3
2019	27.8
2020	25.4
2021	18.7
2022	13.5
2023	21.7
2024	54.1

3.6.3.11 Catchment Area Delineation Along the Bagmati River

After completing the hydrologic modeling for the Nakkhu River, HEC-HMS was further utilized to delineate the catchment areas for three selected points along the Bagmati River within the study area, using the same ALOS PALSAR Digital Elevation Model (DEM) for consistency. The first point, referred to as the confluence upstream point, represents the farthest upstream location of the Bagmati River within the study boundary. The second, the confluence downstream point, is situated just after the confluence of the Bagmati and Nakkhu Rivers. The third point corresponds to the location of the Khokana hydrological station, for which discharge data was provided by the Department of Hydrology and Meteorology (DHM). Since the available discharge data corresponded only to the Khokana station, it was necessary to delineate the catchment areas of the two additional points to estimate their respective discharge values. These estimates were made using the Catchment Area Ratio (CAR) method, based on the principle that peak discharge varies proportionally with catchment area.

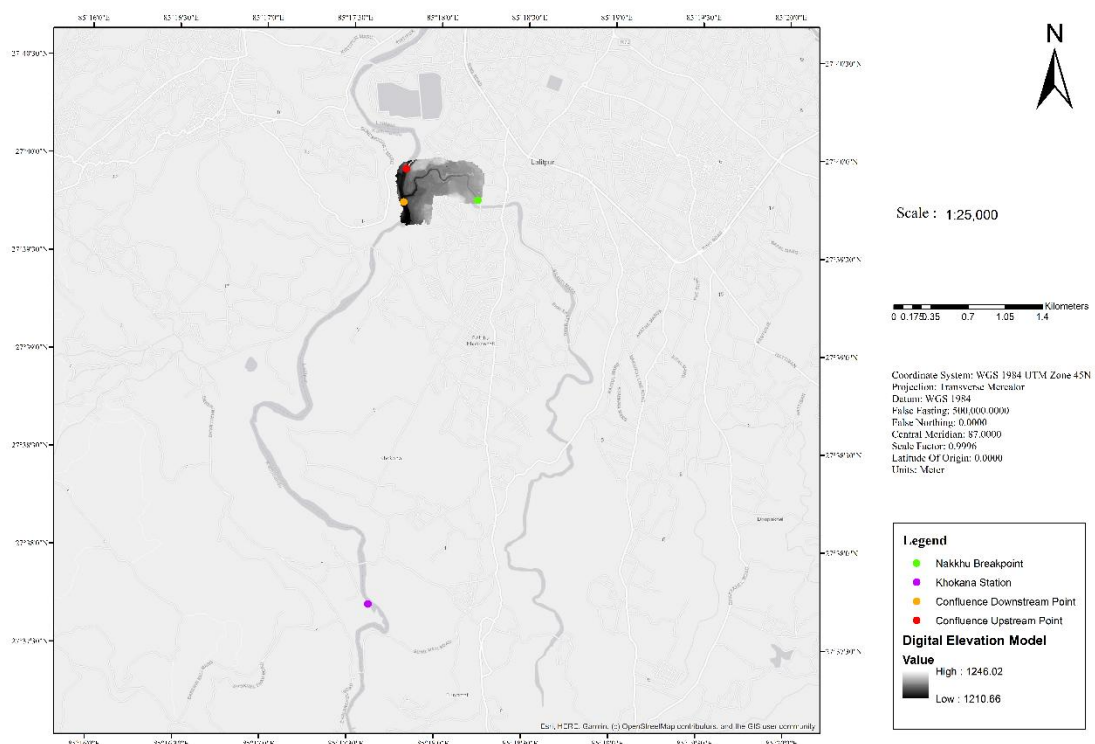


Figure 21: Break Points (Bagmati and Nakkhu)

The Catchment Area were calculated for the points as:

Table 6: Catchment Area for Break Points

Points	Area (km ²)
Nakkhu Breakpoint	54.166
Confluence Upstream Point	531.977
Confluence Downstream Point	588.3779
Khokana Station	607.549

3.6.4 Hydrologic Modelling Using HEC-RAS

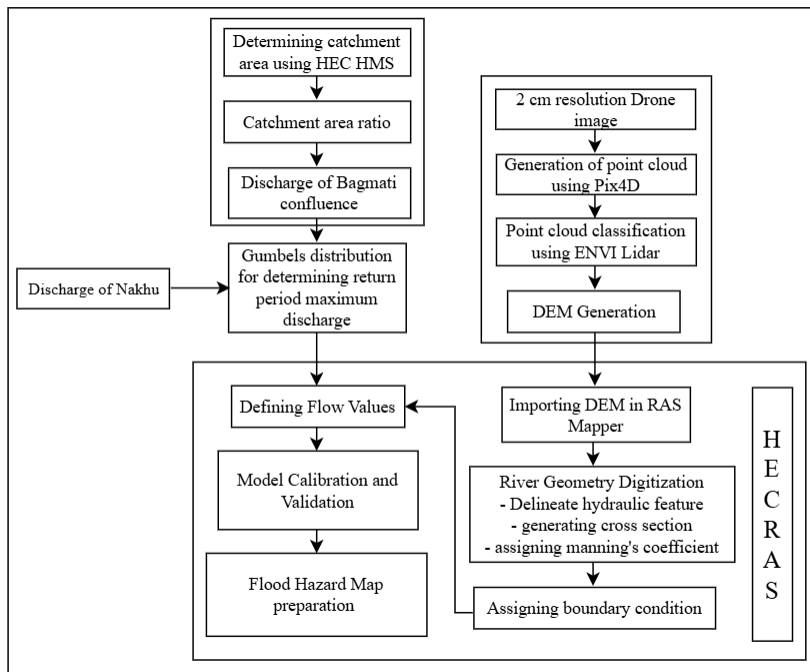


Figure 22: Methodological flowchart for HEC-RAS

3.6.4.1 Flood Frequency analysis

Flood frequency analysis aims to estimate the probability of occurrence of different magnitudes of floods over a specific period. In this study, to model the discharge corresponding to different return periods, we employed Gumbel's Extreme Value Type-I distribution, which is widely used for analyzing hydrological extremes, particularly the annual maximum series of river discharge or water level.

To ensure the appropriate application of Gumbel's distribution, a long-term dataset is essential. Typically, at least 20 years of annual peak discharge data is required for reliable estimates. In our case, a 24-year series of peak annual discharge data (2000–2024) for the Nakku River was derived using HEC-HMS simulations. Using this dataset, the flood magnitudes corresponding to various return periods were estimated through Gumbel's method. The results are presented in the table below:

Table 7: Return Period Discharge of Nakku River obtained using Gumbel's Distribution

Return Period (T) in years.	Reduced Variate, $Y_T = -[\ln \ln(T / (T - 1))]$	Frequency Factor $K = (y_t - \bar{y}_n) / S_n$	Expected Flood (m³/s), $X_T = \bar{X} + K * \sigma_X$
5	1.49994	0.8931701	29.47338
10	2.25037	1.5839169	35.53144
25	3.19852	2.4566773	43.18582
50	3.90194	3.1041409	48.86428
100	4.60015	3.7468237	54.5008
150	5.00729	4.1215875	57.7876

Similarly, we also required peak discharge values before and after confluence of Nakkhu River with the Bagmati River. For this, annual peak discharge data from the Khokana station, located downstream of the confluence was used. The below show the maximum discharge of the Khokana station from year 1993-2024. Using this discharge value as the input for the gumbel's distribution we obtained the return periods discharge of khokana station.

Table 8: Annual Peak Discharge of Khokana Station obtained from DHM

Year	Discharge(m ³ /s)	MAXIMUM INSTANTANEOUS	
		Gauge Height(m)	Date
1993	938	6	20/07/1993
1994	533	4.78	7/8/1994
1995	393	4.24	18/07/1995
1996	328	3.88	14/07/1996
1997	493	4.58	18/08/1997
1998	649	5.08	9/7/1998
1999	421	4.2	3/7/1999
2000	519	4.6	8/8/2000
2001	275	3.5	13/08/2001
2002	942	6	22/07/2002
2003	421	4.2	31/07/2003
2004	268	3.36	9/7/2004
2005	747.953	-	-
2006	191	2.9	19/07/2006
2007	424	4.12	5/9/2007
2008	135	2.5	3/8/2008
2009	375	3.9	27/07/2009
2010	354	3.8	7/9/2010
2011	480	4.36	1/7/2011
2012	173	2.78	3/8/2012
2013	130	2.46	22/07/2013
2014	176	2.8	14/08/2014
2015	364	3.85	17/08/2015
2016	515	4.5	26/07/2016
2017	386	3.95	15/08/2017
2018	354	3.8	12/7/2018
2019	545	4.62	12/7/2019
2020	392	3.86	20/07/2020
2021	571	4.62	6/9/2021
2022	260	3.34	6/10/2022
2023	864	-	-
2024	1138	-	-

Table 9: Return Period Discharge of Khokana River obtained using Gumbel's Distribution

Return Period (T) in years.	Reduced Variate, $Y_T = -[\ln(\ln(T / (T - 1)))]$	Frequency Factor $K = (y_t - \bar{y}_n) / S_n$	Expected Flood (m³/s), $X_T = \bar{X} + K * \sigma_x$
5	1.499939987	0.859412121	672.1903
10	2.250367327	1.529855559	836.8951
25	3.198534261	2.376962621	1045
50	3.901938658	3.005395031	1199.384
100	4.600149227	3.629187194	1352.628
150	5.007292664	3.992935463	1441.989

The discharge values obtained above are specific to the Khokana station which lies downstream. However, to model the Bagmati River before and after the confluence with the Nakkhu River we required discharge estimates at two distinct points.

To derive these, the catchment area ratio method was applied assuming a proportional relationship between catchment area and discharge. Using this approach, the peak discharge values for different return periods were estimated for:

Q_1 = Discharge at confluence upstream point

Q_2 = Discharge at confluence downstream point

Q_3 = Discharge at khokana station point

A_1 = Catchment area of confluence upstream point

A_2 = Catchment area of confluence downstream point

A_3 = Catchment area of khokana station point

The overall peak discharge of the return period for our study is given as:

Table 10: Return Period Discharge before and after Confluence obtained using CAR

At Khokana Station	Peak Discharge (m³/s), Q_3	$A_1 * Q_3$	Q_1 (m³/s)	$A_2 * Q_3$	Q_2 (m³/s)
5 years	672.1903	357589.7792	588.5777	395501.9171	650.9795
10 years	836.8951	445208.9446	732.7951	492410.5815	810.487
25 years	1045	555915.965	915.0142	614854.9055	1012.025
50 years	1199.384	638044.7022	1050.195	705691.0392	1161.538
100 years	1352.628	719566.9856	1184.377	795856.4221	1309.946
150 years	1441.989	767104.9823	1262.622	848434.4596	1396.487

3.6.4.2 Working on HECRAS

For flood modeling, HEC-RAS 6.7 (Beta 2 Developer Version) was employed. HEC-RAS enables simulation of flood events based on discharge inputs and terrain data, and was used to model inundation patterns for different return period flows. The model was run using a steady flow simulation, which assumes constant flow conditions over time. This approach is suitable for analyzing peak flood scenarios and estimating inundation extents for specific return periods.

The following key inputs were used:

Table 11: Return Period Discharge of all required river for integrating to HEC-RAS

Return Period(T) in years	Maximum Discharge(m ³ /s)		
	Nakkhu	Bagmati Before Confluence	Bagmati After Confluence
5	29.47338	588.5777	650.9795
10	35.53144	732.7951	810.487
25	43.18582	915.0142	1012.025
50	48.86428	1050.195	1161.538
100	54.5008	1184.377	1309.946
150	57.7876	1262.622	1396.487

Discharge Data: Peak discharges for various return periods, estimated using Gumbel's distribution, were input at designated flow locations.

Terrain Data: A high-resolution Digital Elevation Model (DEM) was used to define the topographic surface and create the geometric layout of the river and floodplain.

Boundary Conditions: Normal Depth was used as the upstream and downstream boundary conditions to guide the hydraulic behavior of flow through the study area.

Manning's Roughness Coefficient (n): Suitable Manning's n values were assigned to different land cover types along the channel and floodplain to represent surface resistance. These values were based on literature and land use characteristics observed in the study area.

a) Working with RAS Mapper

Ras Mapper is a built-in tool within HEC-RAS that facilitates the integration of terrain data and the creation of geometric components required for hydraulic modeling. In this project, Ras Mapper was used to input the Digital Elevation Model (DEM) and digitize the river geometry, including the river centerline, bank lines, flow paths, and cross-sections.

Key considerations during geometry creation included:

- All geometric features (centerline, bank lines, flow paths, and cross-sections) were drawn from left to right, following the direction of flow, i.e., from upstream to downstream.
- Cross-sections were ensured to be non-intersecting and drawn perpendicular to the flow direction, especially relative to the river centerline.

- For rivers with confluence points (as in our case, where the Nakkhu River joins the Bagmati River), junctions were properly defined. Each reach's centerline was separately connected to the junction point at the confluence to maintain hydraulic continuity and accurate flow distribution.

This step was critical to ensure the accuracy of the hydraulic model and to avoid computational errors during simulation.

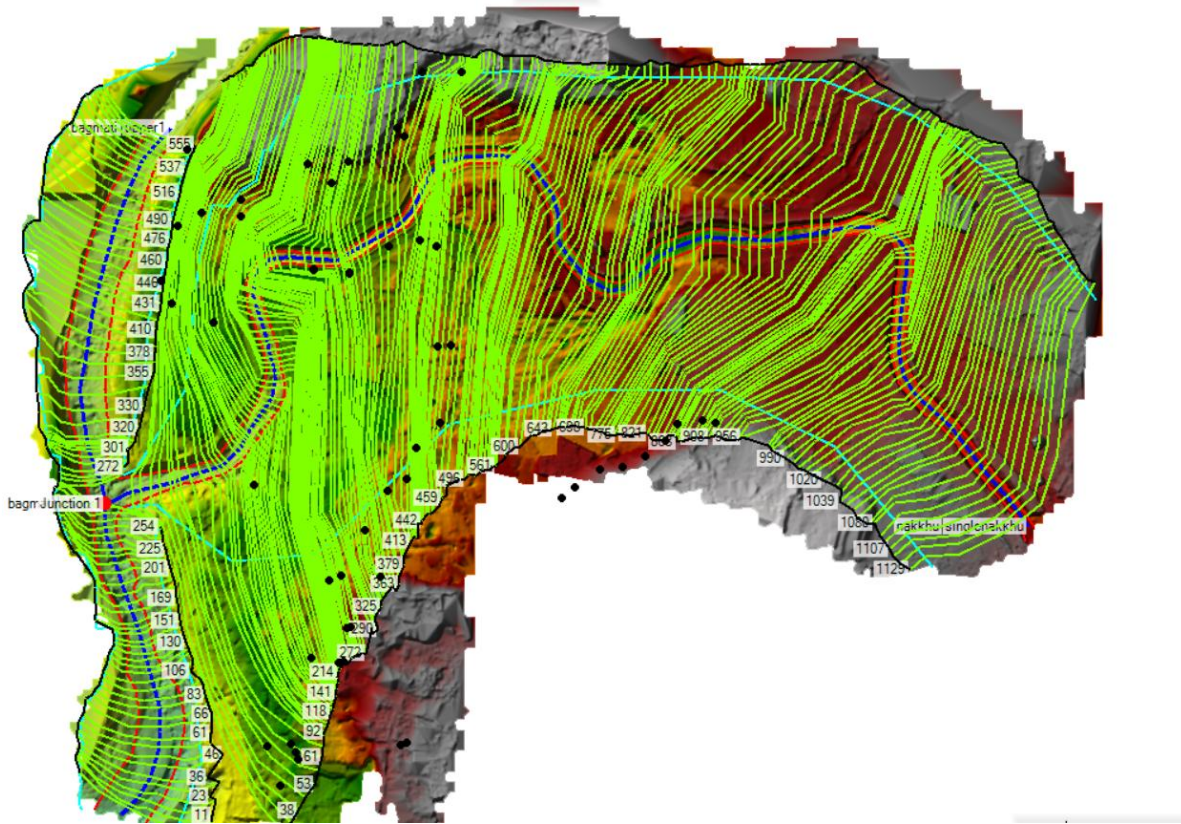


Figure 23: Terrain and River Geometry used for the modelling the flood return periods

b) Manning's Coefficient

The View/Edit Geometry tool in HEC-RAS allows for visualization and modification of the cross-sections created for each reach. In this project, three reaches were defined: Upper Bagmati, Lower Bagmati, and the Nakkhu River. Within this tool, Manning's roughness coefficients can be assigned to individual cross-sections to represent channel and overbank resistance. However, for simplification, a uniform Manning's coefficient was assumed across the entire study area.

c) Steady Flow data

In this study, the steady flow analysis was conducted to simulate peak flood conditions for various return periods. The Steady Flow Data editor in HEC-RAS was used to input peak discharges corresponding to each return period at designated upstream locations. The discharge value entered

was of Upstream of Nakkhu River, Upstream of Bagmati River and Downstream of Bagmati River. This steady flow setup enabled the model to compute water surface profiles and inundation extents corresponding to different flood scenarios. Under the steady flow reach boundary conditions was selected as normal depth.

	River	Reach	RS	5 yrs	10 yrs	25 yrs	50 yrs	100 yrs	150 yrs
1	bagmati	upper1	555	588	733	915	1050	1184	1263
2	bagmati	lower2	254	650	810	1012	1162	1309	1396
3	nakkhu	singlenakkhu	1129	29	35	43	49	54	58

Figure 24: Assigning steady flow data for each profile (return year)

d) Reach Boundary Condition

Reach boundary conditions are essential for accurate computation of water surface profiles in HEC-RAS. For this study, under steady flow conditions, the boundary condition selected was the normal depth. It refers to the uniform water depth achieved under a constant discharge in a channel with a uniform slope. Normal depth is calculated based on the channel slope which was provided as input for the upstream of Nakkhu River, upstream of Bagmati River and downstream of Bagmati River.

The channel slope was determined using the HEC-RAS View Profile tool. It allows users to visualize water surface and channel bed profiles. The slope between two cross-sections can be calculated using the following formula:

$$\text{Slope}(S) = \frac{\Delta h}{L}$$

Where,

Δh = Elevation difference between two cross-sections (m)

L = Horizontal distance between the two cross-sections (m)

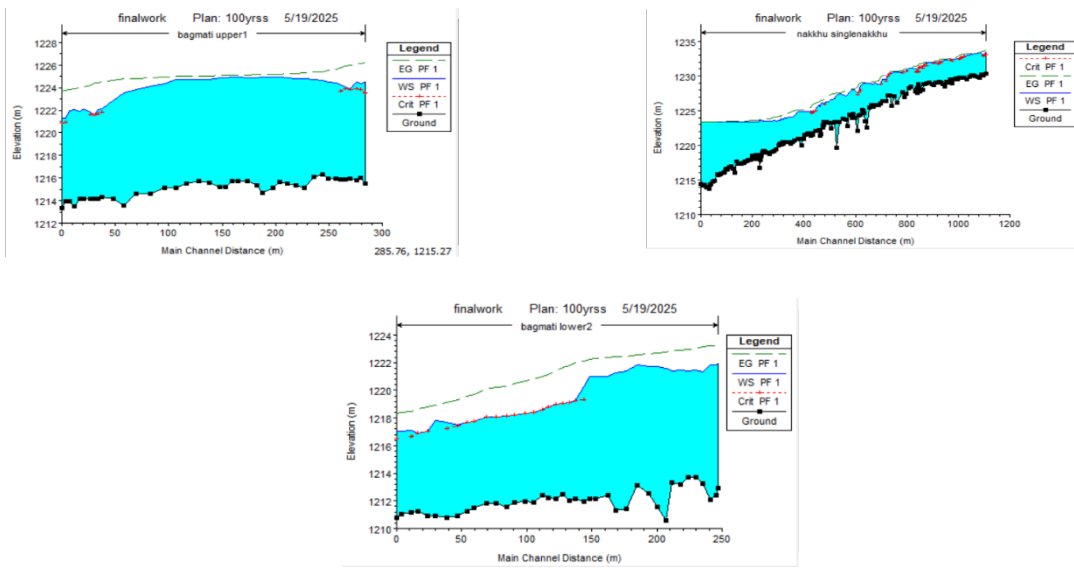


Figure 25: Determining slope using Reaches Profile

After determining the slope for each reaches the corresponding values are the input for the nromal depth as the boundary condition.

Steady Flow Boundary Conditions

Set boundary for all profiles Set boundary for one profile at a time

Available External Boundary Condition Types				
Known W.S.	Critical Depth	Normal Depth	Rating Curve	Delete
Selected Boundary Condition Locations and Types				
River	Reach	Profile	Upstream	Downstream
bagmati	upper1	all	Normal Depth S = 0.007	Junction=Junction 1
bagmati	lower2	all	Junction=Junction 1	Normal Depth S = 0.009
nakku	singlenakkhu	all	Normal Depth S = 0.014	Junction=Junction 1

Figure 26: Input for Reach Boundary Condition

3.6.4.3 Modeling of Flood Event of 27 September 2024

The flood event on September 27, 2024, resulted in peak discharges that significantly exceeded those estimated using standard return period analysis. Gumbel-based calculations suggested peak flows of approximately $1100 \text{ m}^3/\text{s}$ for the Bagmati River and $60 \text{ m}^3/\text{s}$ for the Nakkhu River. However, these values proved insufficient to reproduce the actual flood extent observed during field validation.

To address this, we relied on high-water marks, flood stains, and eyewitness accounts to iteratively adjust the discharge inputs in the HEC-RAS model. This trial-and-error approach continued until the simulated inundation closely matched the observed flood extent. While the final discharge values differ from Gumbel-based estimates, they are grounded in field evidence and reflect the actual hydraulic behavior during the event.

The discrepancy highlights a key limitation of purely statistical methods like the Gumbel distribution, which assume regularity in annual peak flows and fail to capture atypical events. The September 27 flood was likely driven by backwater effects or complex flow interactions, rather than extreme upstream discharge. As a result, conventional estimates substantially underestimated the flood hazard. To improve model accuracy, Manning's roughness coefficients were also calibrated using observed flood depths and elevation differences between terrain and high-water marks. This allowed for a more realistic representation of flow conditions.

Although this flood event does not correspond to any return period based on available discharge records, it underscores the importance of integrating empirical field data with hydraulic modeling. Understanding the causes and frequency of such anomalous floods remains an important area for future research, particularly in the context of evolving hydrological extremes.

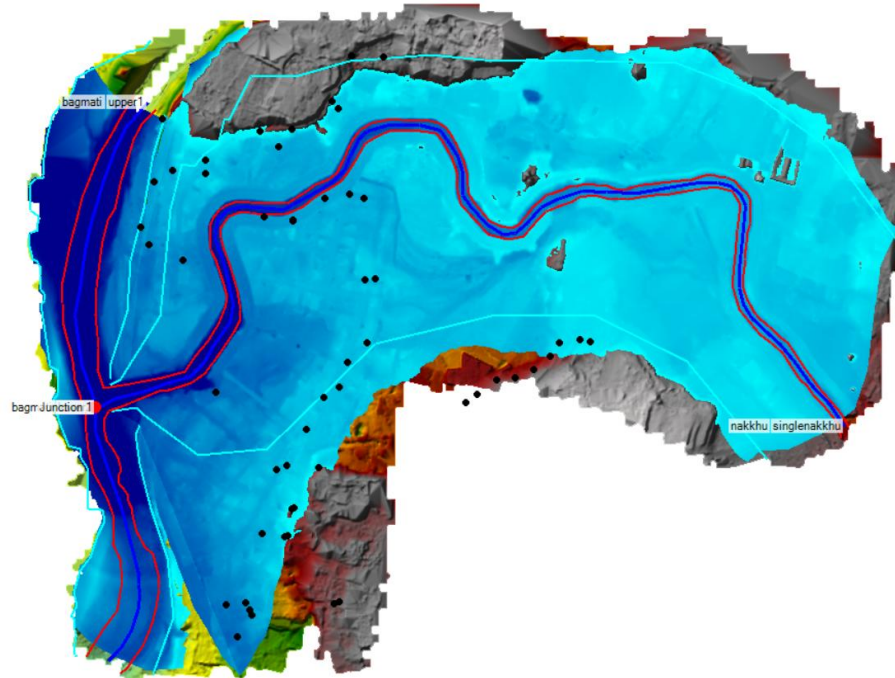


Figure 27: Calibrating the extent of September 27, 2024 flood using the surveyed points

3.6.4.4 Hydraulic Calibration Using Field Data

Model calibration typically involves comparing simulated and observed annual peak water depths. However, in this study, such annual depth data were not available for the Nakkhu and Bagmati Rivers. Instead, calibration was performed using field data collected during the exceptional flood event of September 27, 2024. Based on guidelines from Chow (1997), Manning's roughness coefficient for urban stream channels ranges between 0.03 and 0.07. This range was used to test multiple simulations.

Field-surveyed elevation and water depth data from flood-inundated points were used for comparison. Points located within the flood extent were selected, and the simulated depth and elevation values at the same locations were extracted from the model outputs under different Manning's coefficients. The coefficient that yielded the closest match between the modeled and observed depths and elevation was selected for the final simulation, serving as an alternative and practical approach to calibration in the absence of long-term depth records.

A total of 56 points obtained from a field survey were used to calibrate the Manning's roughness coefficient of which 22 depth points and 16 elevations points as the sample are shown on the tables below. At each location, the observed water depth and elevation during the September 27, 2024 flood event was compared with the modeled depths and elevations generated under different Manning's values. The following tables presents the actual field-measured depths and elevations alongside the simulated depths and elevation for various Manning's coefficients within the range of 0.03 to 0.07.

Table 12: Comparison of depth for different manning's coefficient with the observed depth

Id	Elevation (m)		Depth (m)								
	Observed	DEM	Observed	n=0.03	n=0.04	n=0.05	n=0.055	n=0.06	n=0.065	n=0.7	
1	1232.891	1227.371	5.52	4.937	5.072	5.234	5.323	5.417	5.515	5.618	
2	1232.041	1227.507	4.534	4.769	4.917	5.09	5.185	5.285	5.388	5.495	
3	1232.938	1227.507	5.431	4.769	4.917	5.09	5.185	5.285	5.388	5.495	
4	1232.441	1229.005	3.436	3.181	3.363	3.564	3.672	3.782	3.896	4.012	
5	1232.001	1227.939	4.062	4.27	4.434	4.624	4.727	4.833	4.942	5.055	
6	1232.583	1229.599	2.984	2.598	2.774	2.972	3.078	3.188	3.3	3.416	
7	1232.976	1228.646	4.33	3.634	3.777	3.945	4.038	4.135	4.236	4.342	
8	1232.456	1228.782	3.674	3.521	3.658	3.819	3.909	4.003	4.101	4.204	
9	1232.793	1229.185	3.608	3.1	3.228	3.381	3.468	3.557	3.652	3.752	
10	1232.221	1229.092	3.129	3.186	3.302	3.443	3.523	3.607	3.696	3.79	
11	1232.679	1230.049	2.63	2.24	2.357	2.499	2.58	2.664	2.754	2.848	
12	1232.327	1228.595	3.732	3.747	3.853	3.982	4.056	4.134	4.217	4.306	
13	1232.81	1228.194	4.616	4.149	4.252	4.38	4.453	4.53	4.613	4.699	
14	1232.987	1227.635	5.352	4.706	4.804	4.926	4.996	5.07	5.149	5.233	
15	1232.524	1230.206	2.318	2.146	2.249	2.375	2.447	2.523	2.605	2.691	
16	1232.018	1230.931	1.087	1.417	1.52	1.647	1.72	1.797	1.879	1.965	
17	1232.495	1231.487	1.008	0.857	0.962	1.091	1.165	1.243	1.326	1.415	
18	1232.117	1224.067	8.05	8.298	8.387	8.499	8.563	8.633	8.706	8.784	
19	1231.881	1226.111	5.77	6.252	6.342	6.455	6.52	6.589	6.663	6.742	
20	1232.614	1224.413	8.201	7.95	8.04	8.153	8.217	8.287	8.36	8.439	
21	1232.843	1225.785	7.058	6.581	6.671	6.784	6.849	6.918	6.992	7.071	
22	1233.107	1226.406	6.701	5.957	6.047	6.159	6.224	6.293	6.367	6.446	

Table 13: Comparison of elevation for different manning's coefficient with the observed elevation

Id	Elevation (m)								
	Observed	n=0.03	n=0.04	n=0.04	n=0.05	n=0.055	n=0.065	n=0.07	
1	1232.891	1232.304	1232.439	1232.601	1232.69	1232.784	1232.883	1232.985	
2	1232.041	1232.277	1232.425	1232.598	1232.693	1232.792	1232.896	1233.003	
3	1232.938	1232.277	1232.425	1232.598	1232.693	1232.792	1232.896	1233.003	
4	1232.441	1232.189	1232.37	1232.572	1232.679	1232.79	1232.903	1233.02	
5	1232.001	1232.207	1232.372	1232.562	1232.664	1232.771	1232.88	1232.993	
6	1232.583	1232.199	1232.376	1232.574	1232.68	1232.789	1232.902	1233.017	
7	1232.976	1232.282	1232.425	1232.594	1232.686	1232.784	1232.885	1232.99	
8	1232.456	1232.303	1232.439	1232.601	1232.69	1232.784	1232.883	1232.985	
9	1232.793	1232.288	1232.416	1232.569	1232.655	1232.745	1232.84	1232.939	
10	1232.221	1232.28	1232.395	1232.537	1232.616	1232.701	1232.79	1232.884	
11	1232.679	1232.287	1232.404	1232.546	1232.626	1232.711	1232.801	1232.895	
12	1232.327	1232.341	1232.446	1232.575	1232.649	1232.728	1232.811	1232.899	

13	1232.81	1232.344	1232.448	1232.575	1232.648	1232.726	1232.808	1232.895
14	1232.987	1232.339	1232.437	1232.559	1232.629	1232.703	1232.782	1232.866
15	1232.524	1232.349	1232.452	1232.578	1232.65	1232.727	1232.808	1232.894
16	1232.018	1232.347	1232.45	1232.577	1232.65	1232.726	1232.808	1232.895

The scatter plot (Figure 3) illustrates the relationship between observed and simulated depths for various Manning's n values. Each point represents a location in the domain, with colors distinguishing the n values. For lower n values of 0.03 to 0.05 the simulated depths closely align with the observed depths, clustering near the 1:1 line. As n increases beyond 0.06 the spread increases and simulated depths start to deviate from the observed values indicating reduced model accuracy.

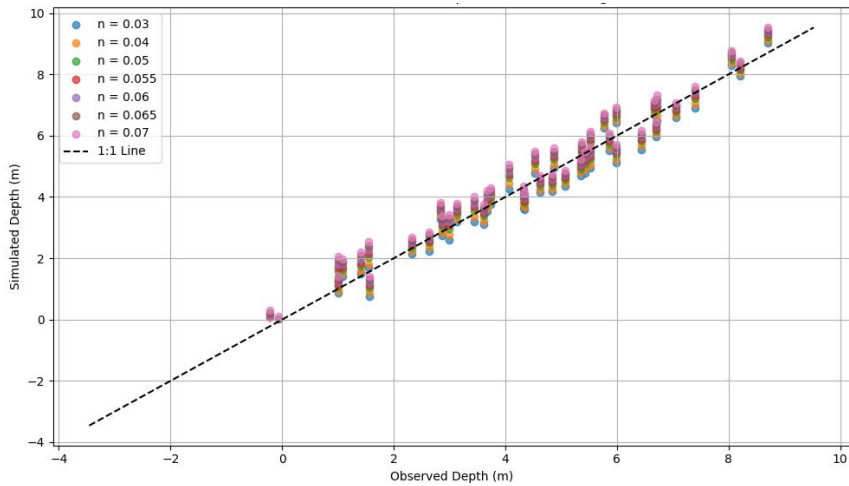


Figure 28: Comparison Between Observed Depth and Simulated Depth

Similarly, Figure 29 illustrates the relationship between observed and simulated elevation for various Manning's n values.

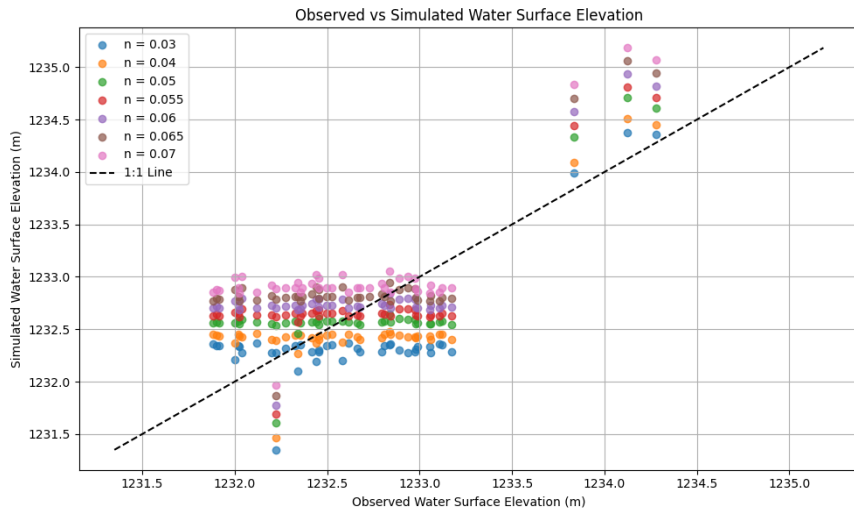


Figure 29: Comparison between Observed Elevation and Simulated Elevation

The Root Mean Square Error (RMSE) was calculated for each Manning's n to quantify the error between observed and simulated depths (Figure 4). The lowest RMSE was observed for $n = 0.05$ (approximately 0.40 m), indicating it provides the best fit to the observed data. RMSE increases as n deviates from 0.05 in both directions with the highest error (~0.57 m) occurring at $n = 0.07$. This analysis suggests that Manning's $n = 0.05$ provides the optimal balance between roughness representation and depth prediction accuracy for the modeled domain.

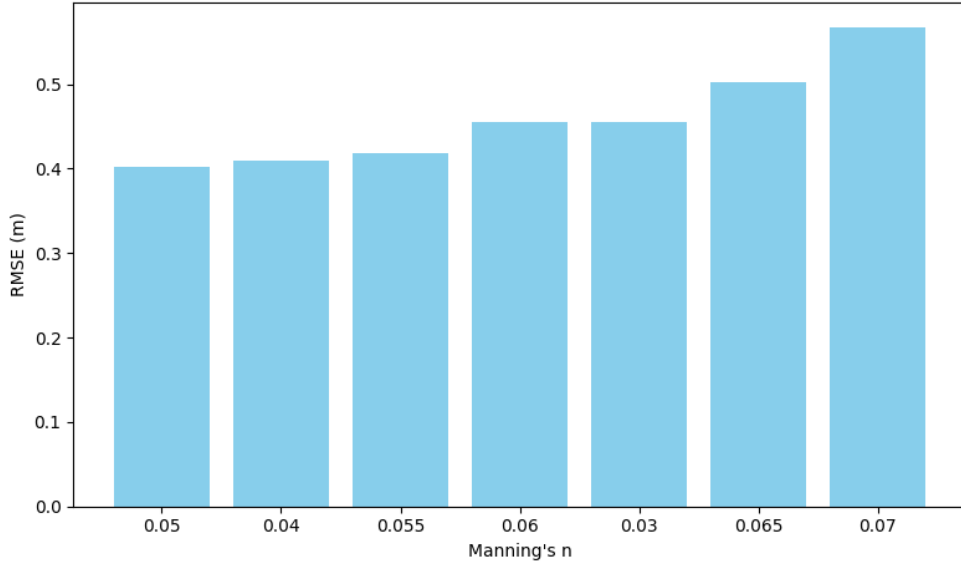


Figure 30: RMSE for each Manning's Coefficient for range (0.03-0.07) in increasing order

Table 14: RMSE Value for different Manning's Coefficient

Manning's Coefficient (n)	RMSE
0.05	0.401813
0.04	0.409005
0.055	0.417763
0.06	0.454878
0.03	0.455071
0.065	0.502254
0.07	0.56784

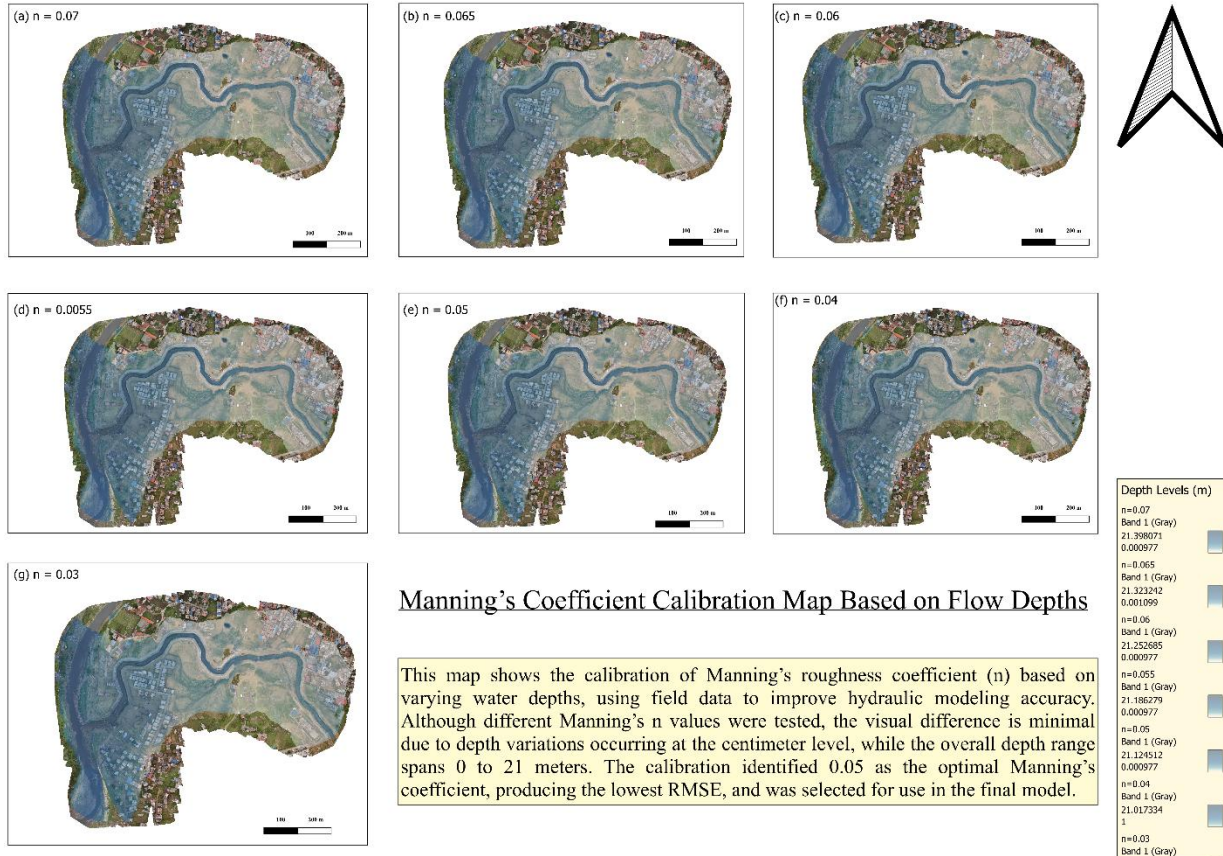


Figure 31: Inundation map of 27th September flood using manning's coefficient (0.03-0.07)

3.6.5 Preparation of Hazard Map

A geospatial analysis was performed to create flood hazard maps. The LULC of the study area was created by digitization of the high resolution orthophoto obtained from the UAV flight. Flood depth rasters obtained from HEC-RAS for every case of return period and for the event of 27 September were reclassified into 5 hazard classes based on ranges of depth: low (<2m), moderate (2-4m), high (4-8m), very high (8-12m) and extreme (>12m). This range was selected based on local considerations, as there was no available literature that specifically supports the flood range applicable to our study area.

The classified flood depth rasters were overlaid on the LULC map to create flood hazard maps. For each return period, the area proportion covered by each hazard class was calculated to represent flood exposure. For the 27 September flood, an overlay operation was performed to observe how much of each LULC was affected by each hazard class.

4 PROJECT MANAGEMENT

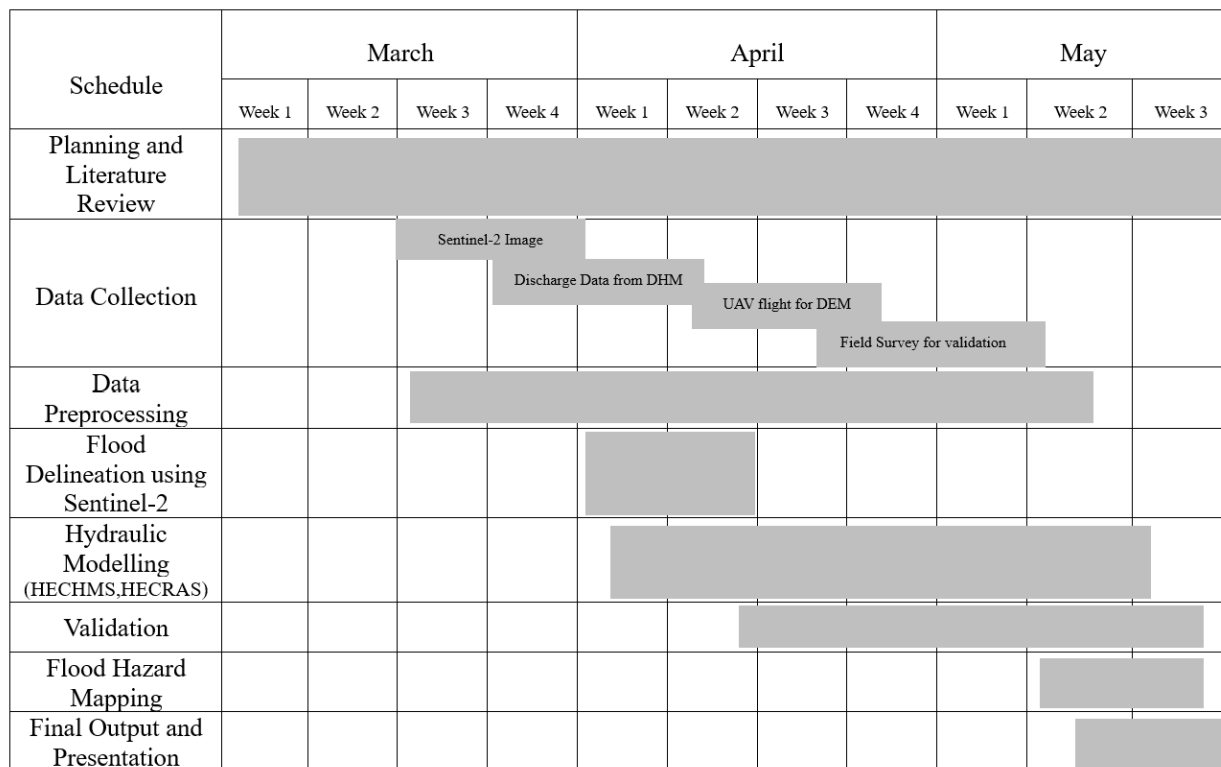
Table 15: Project Management Table

Objective	Activity	Who	When (adjusted)	How	Risk	Remedy
Delineate flood extent from image	Supervised Classification (Sentinel-2)	Pragyan Baral	April Week 2 – April Week 4	Sentinel-2 classification of 27 Sep flood	Cloud cover, spectral confusion	Use cloud-masked image, verification
Gather hydrological records	Discharge Data Collection	Shisir Kharel Abhinav Chand	March Week 3 – April Week 1	Collect historical rainfall and flow data	Missing/inconsistent data	Use of satellite rainfall
Simulate flood-producing runoff	Discharge Modelling (HEC-HMS)	Shisir Kharel	April Week 2 – April Week 4	Basin delineation, HEC-HMS model setup	Parameter uncertainty	Sensitivity analysis and calibration
Capture high-resolution terrain	UAV Survey	Abhinav Pragyan Shisir Saurav Rishav	April Week 1 – April Week 2	Drone flights with RTK GCP setup	Weather	Schedule flexibly; carry spares
Generate accurate elevation data	UAV Data Processing (DEM/Ortho)	Pragyan Baral	April Week 3 – April Week 4	Agisoft Metashape, PIX4D processing	Processing errors	QC checks
Accurate Data Acquisition	Field Survey	Abhinav Chand, Saurav Nepal	April Week 2 – April Week 3	GPS data collection, land cover ground-truthing	Access issues	Coordinate with locals
Simulate flood extent and depths	Hydraulic Modelling (HEC-RAS)	Rishav Khatiwada	April Week 4 – May Week 1	Use 1D HEC-RAS with terrain and discharges	Software instability	
Improve simulation	Manning's Coefficient Calibration	Rishav Khatiwada	May Week 1 – May Week 2	Compare flood marks and adjust roughness	Over/underestimation of depth	Iterative calibration and validation
Visualise spatial hazard	Hazard Mapping	Pragyan Baral Shisir Kharel	May Week 2 – May Week 3	Overlay flood depth and LULC, classify severity	Overlapping classes, readability	Use standard cartographic symbology

Produce output and maps	Mapping & Cartography	Saurav Nepal	May Week 3	Design final maps, legends, layout	Visual clutter, color conflicts	Cartographic guidelines, layout reviews
-------------------------	-----------------------	--------------	------------	------------------------------------	---------------------------------	-----------------------------------------

4.1 Gantt Chart

Table 16: Project Schedule



5 BUDGET

Table 17: Budget Table

Category	Subcategory	Estimated Cost (NRS)	Remarks
1. Transportation	Local travel (fuel, public transport)	500	Travel to flood-prone areas for ground truthing and data collection.
2. Equipment	DGPS device (Base + Rover)	2,500	By Geo 3D Modeling
	Field notebooks and stationery	500	For recording observations and data.
3. Miscellaneous Costs	Communication (mobile data, calls)	500	For coordination and data sharing during field visits.

6 RESULTS AND DISCUSSIONS

6.1 Flood Inundation Modelling

The results show flood extents for different return periods, along with cross sections at three key river stations: 875, 512, and 45. These correspond to the first turning point, second turning point, and the confluence, respectively.

For the September flood mapping cross section results are available for both the upstream and downstream ends of the reach including the same river stations as of Nakkhu.

These cross-section lines (875, 512, 45) are consistently shown in each of the return period flood depth maps presented below in the report. They serve as reference transects across the floodplain, allowing for comparative analysis of flood behavior under different return period scenarios.

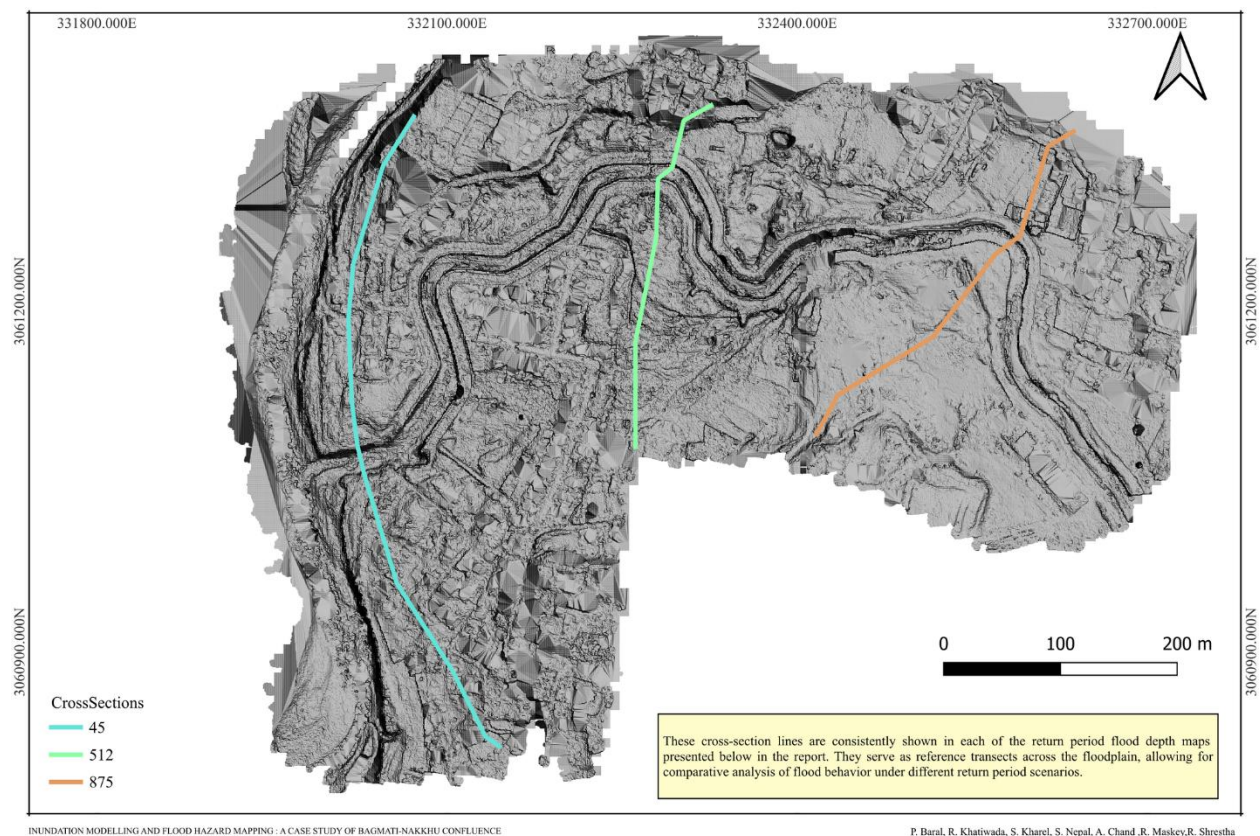
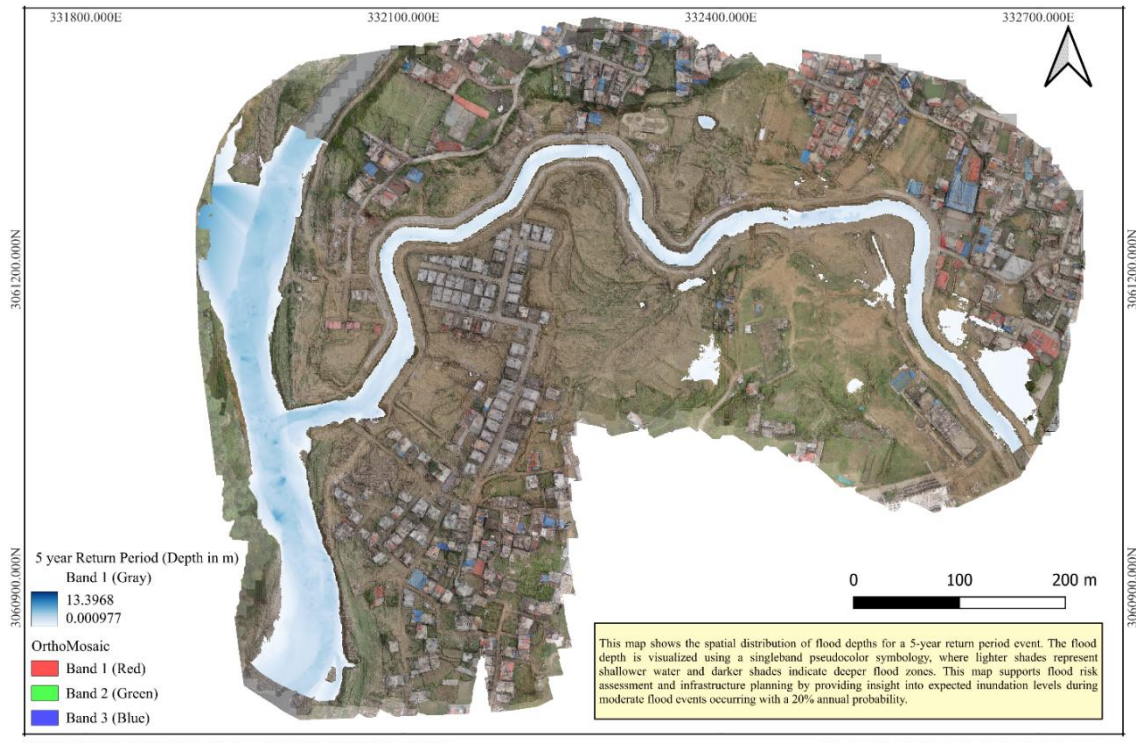


Figure 32: Cross Sections along Nakkhu River

6.1.1 5 Year Return Period

The inundation map for the 5-year return period shows relatively mild flooding conditions. Depths stay low in general, but exhibit modestly higher depths along the Bagmati River. Overall extent of inundation is limited and only minor flooding is observed in some upstream segments of the Nakkhu River, seemingly due to localized accumulation in flatter terrain. These patterns imply relatively small flood impacts at lower-frequency, lower-magnitude events.



INUNDATION MODELLING AND FLOOD HAZARD MAPPING : A CASE STUDY OF BAGMATI-NAKKHU CONFLUENCE
P. Bural, R. Khatiwada, S. Kharel, S. Nepal, A. Chand, R. Maskey, R. Shrestha

Figure 33: Inundation map for 5 year return period

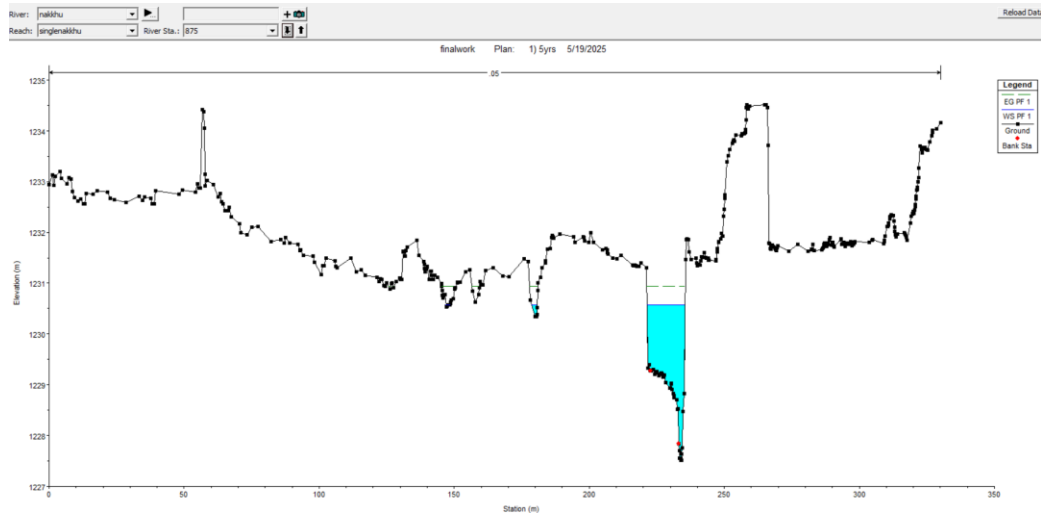


Figure 34: Cross section of upstream part of Nakkhu for 5 year return period

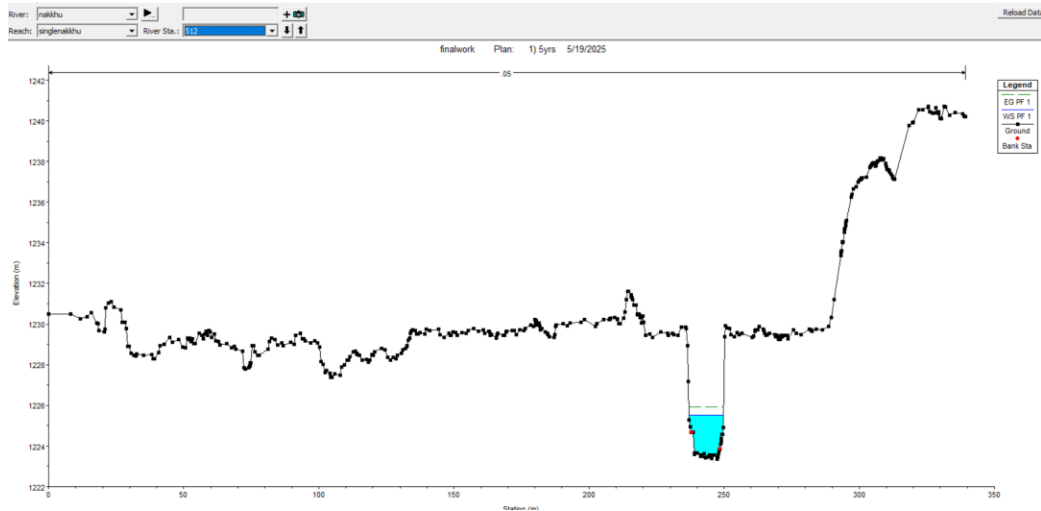


Figure 35: Cross section of mid-nakkhu for 5 year return period

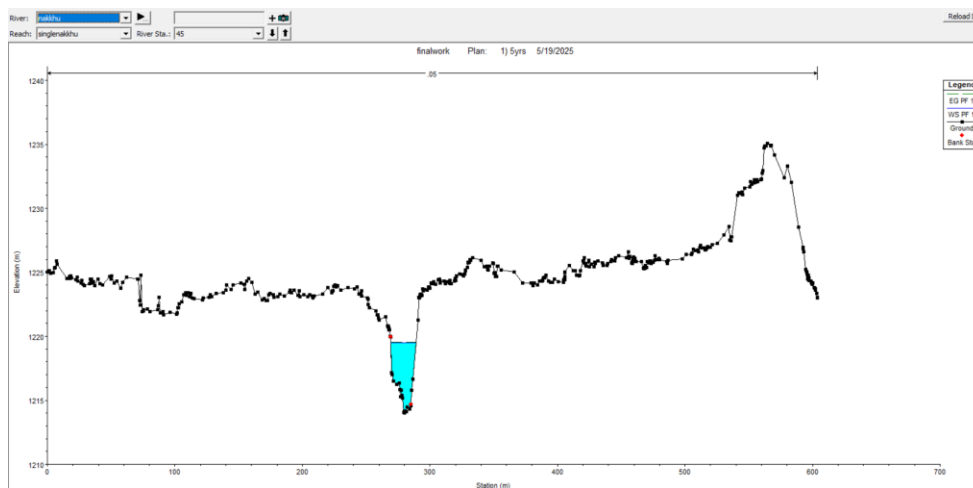
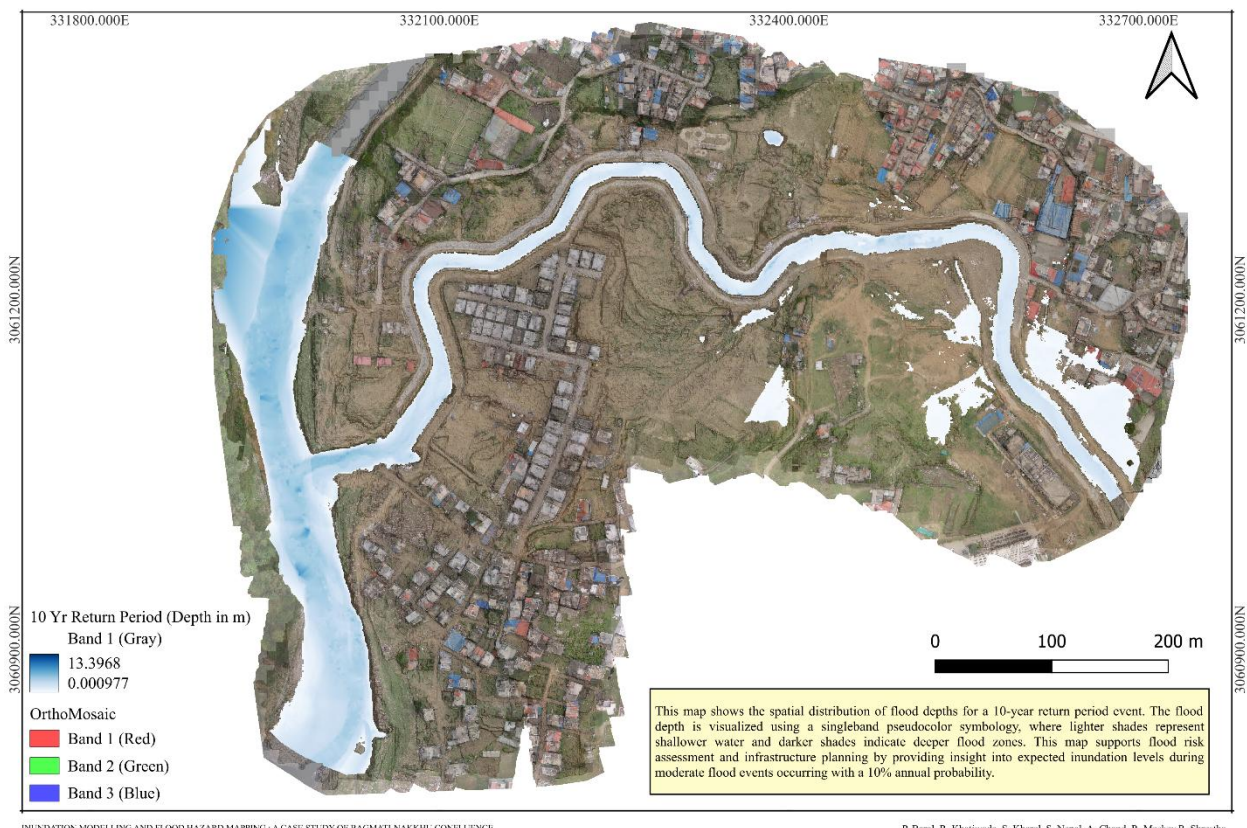


Figure 36: Cross section around Bagmati-Nakku confluence for 5 year return period

6.1.2 10 Years Return Period

Again, the inundation maps for the 10-year return period exhibit an increase in mean water depth along the Bagmati and Nakku rivers, when comparing to the 5-year inundation scenario. In particular; the upstream region of the Nakku River, an increase in the inundated area occurs. Overall, the extent of flooding (though still moderate) is clearly greater in magnitude and impact in comparison to lower return period flooding events.



INUNDATION MODELLING AND FLOOD HAZARD MAPPING : A CASE STUDY OF BAGMATI-NAKKHU CONFLUENCE

P. Baral, R. Khariwada, S. Kharel, S. Nepal, A. Chaudhary, R. Maskey, R. Shrestha

Figure 37: Inundation map for 10 year return period

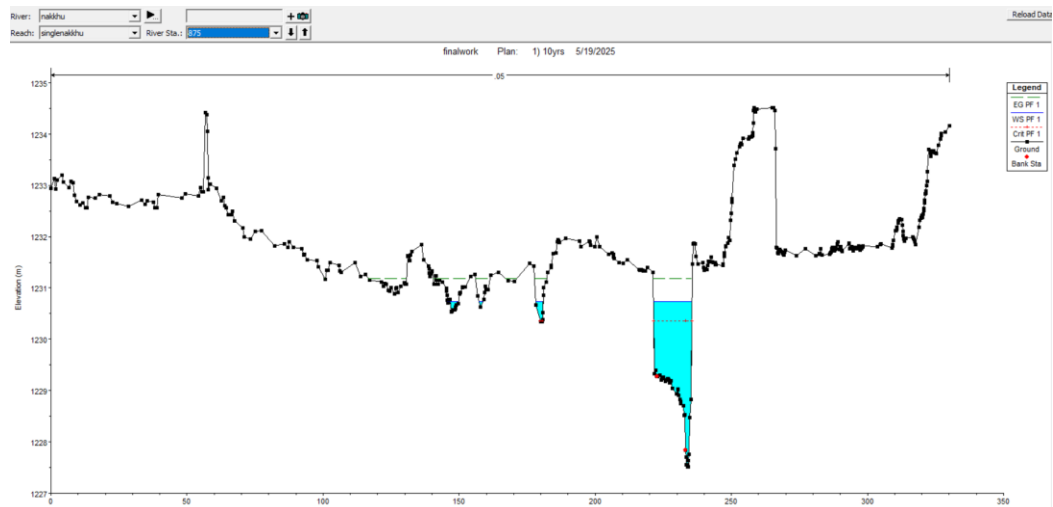


Figure 38: Cross section of upstream part of Nakkhu for 10 year return period

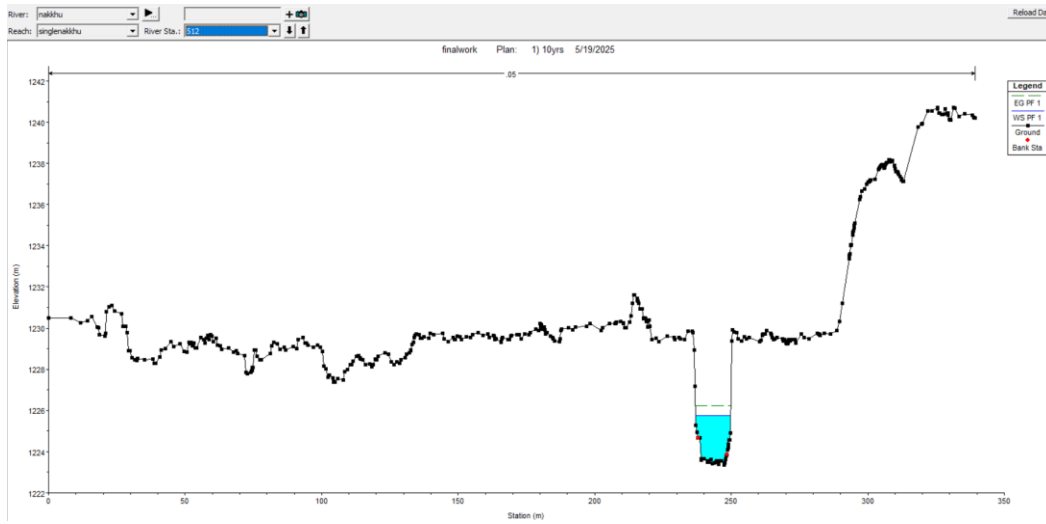


Figure 39: Cross section of mid-nakkhu for 10 year return period

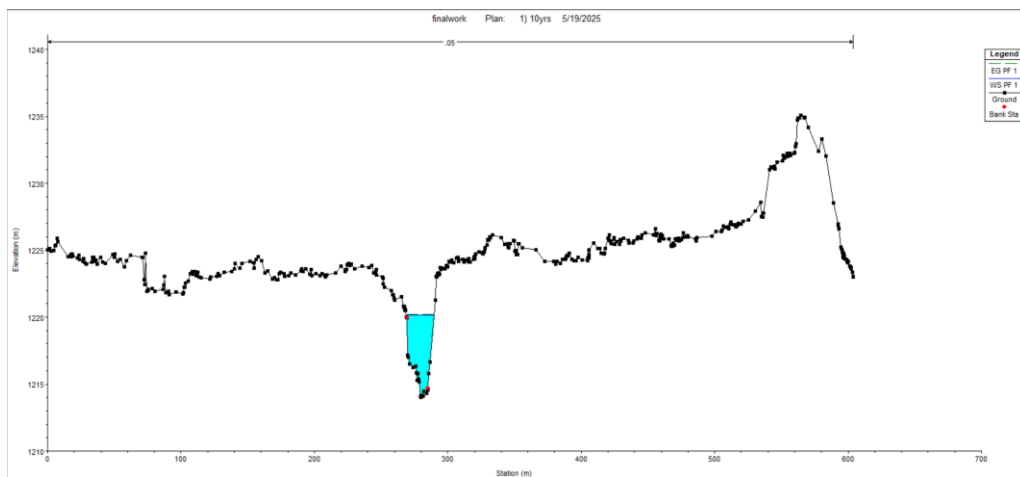
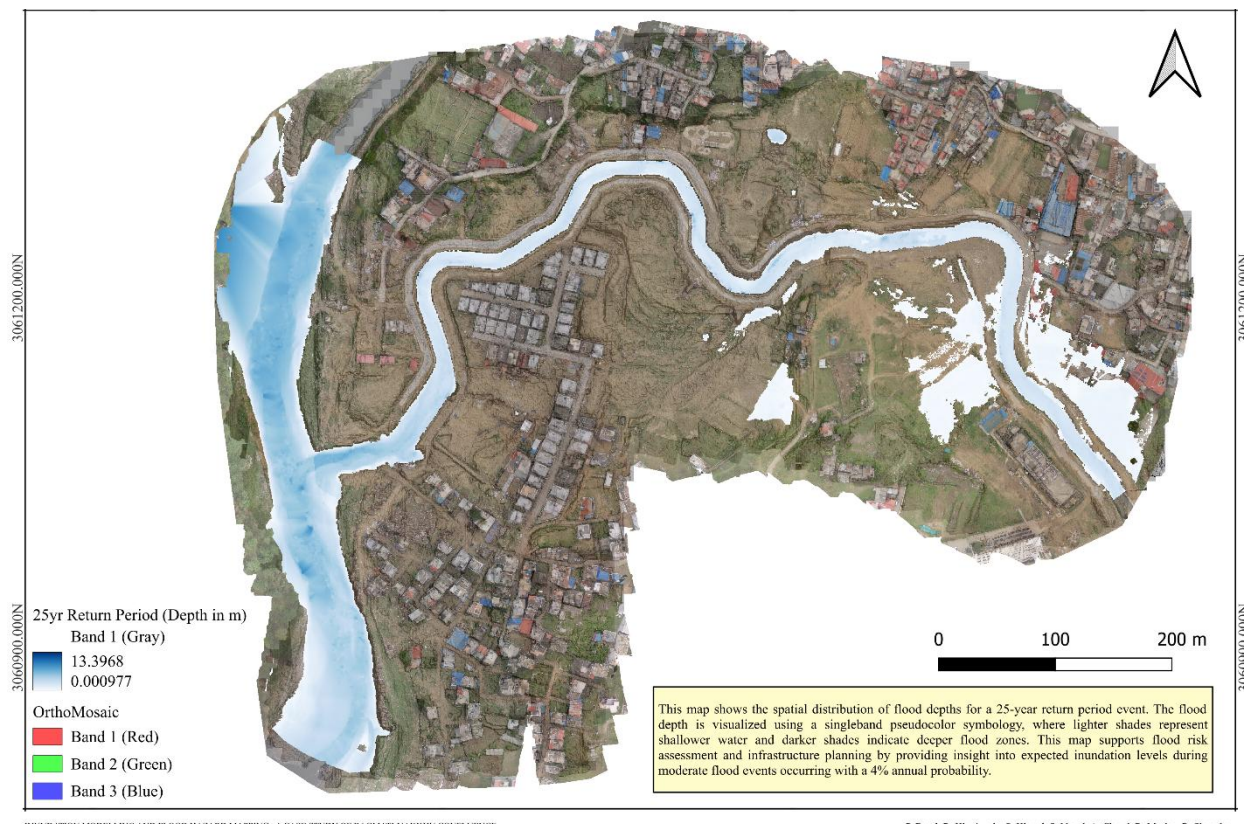


Figure 40: Cross section around Bagmati-Nakkhu confluence for 10 year return period

6.1.3 25 Years Return Period

The flood map for the 25-year return period shows an increase in water depth and area where there is flooding based on the 10-year map. The flooding increases spatially for the Bagmati and Nakkhu rivers, especially much more inundation occurs around the confluence area. The upstream area of the Nakkhu River also has increased flooding.



INUNDATION MODELLING AND FLOOD HAZARD MAPPING : A CASE STUDY OF BAGMATI-NAKKHU CONFLUENCE

P. Baral, R. Khatiwada, S. Kharel, S. Nepal, A. Chand, R. Maskey, R. Shrestha

Figure 41: Inundation map for 25 year return period

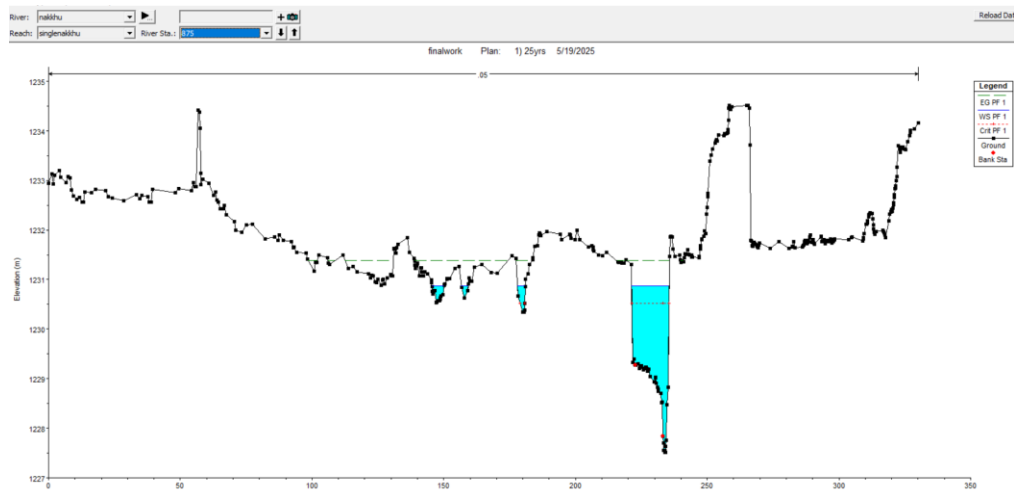


Figure 42: Cross section of upstream part of Nakkhu for 25 year return period

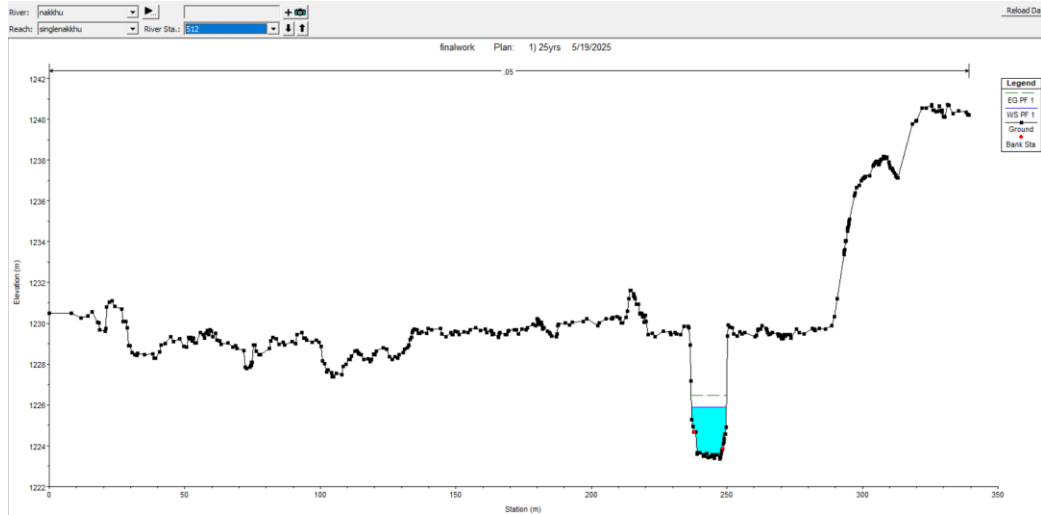


Figure 43: Cross section of mid-nakkhu for 25 year return period

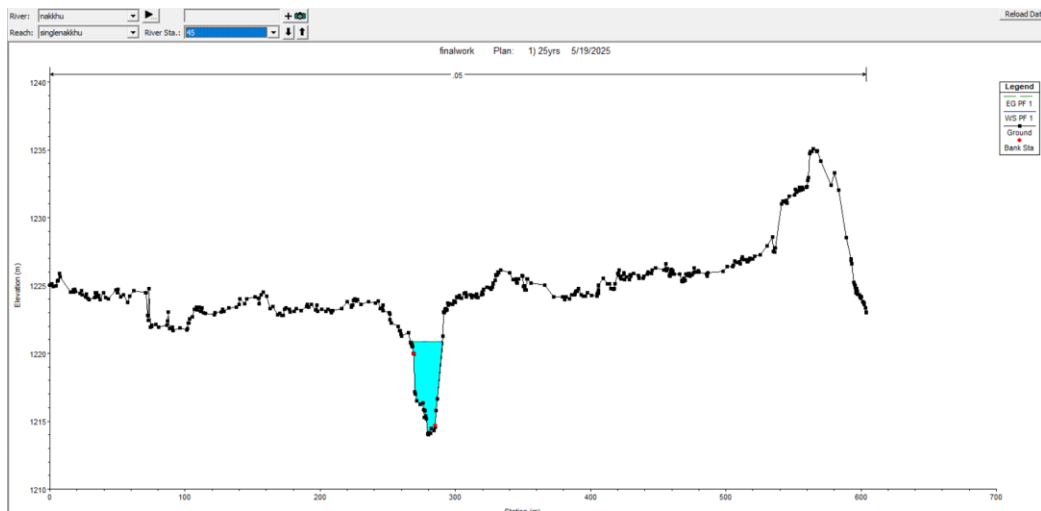
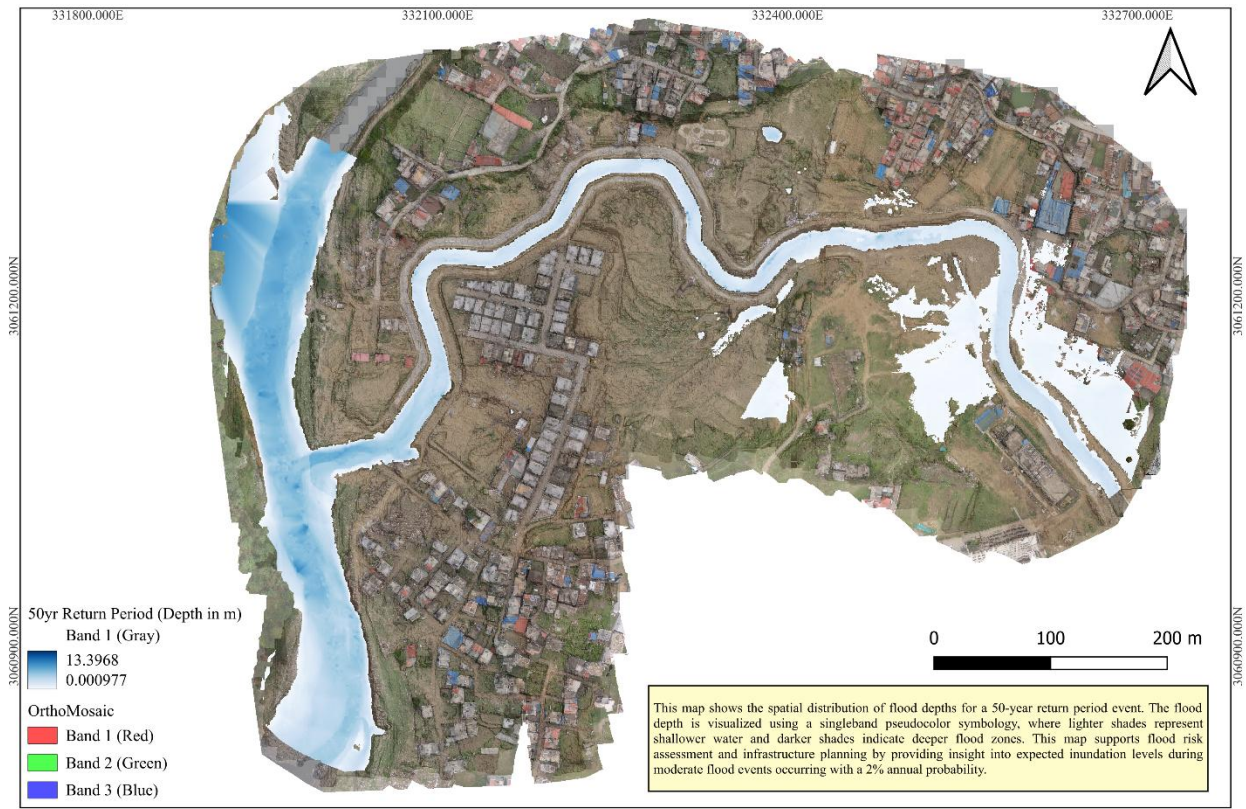


Figure 44: Cross section around Bagmati-Nakku confluence for 25 year return period

6.1.4 50 Years Return Period

Inundation map for a 50-year return period continues to indicate flooding with an increase in both depth and covered areas of flooding as in the 25-year return period. The water levels along the Bagmati and Nakku rivers increase as do the inundation depths in the inundation map as well spatial extent of inundation which covers additional settlement areas when compared to the 25-year inundation map, especially near the confluence of either river. The flooding levels for the upstream areas of Nakku (i.e. similar to the Bagmati) also extend into broader and deeper areas, demonstrating that as the return period is longer, the flood hazard gets even worse.



INUNDATION MODELLING AND FLOOD HAZARD MAPPING : A CASE STUDY OF BAGMATI-NAKKHU CONFLUENCE

P. Baral, R. Khatiwada, S. Kharel, S. Nepal, A. Chaudhary, R. Maskey, R. Shrestha

Figure 45: Inundation map for 50 year return period

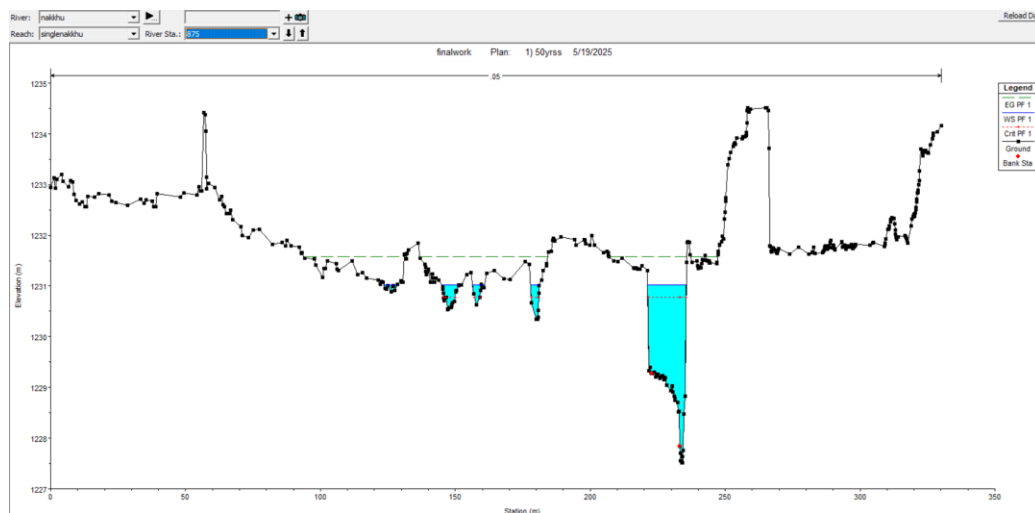


Figure 46: Cross section of upstream part of Nakkhu for 50 year return period

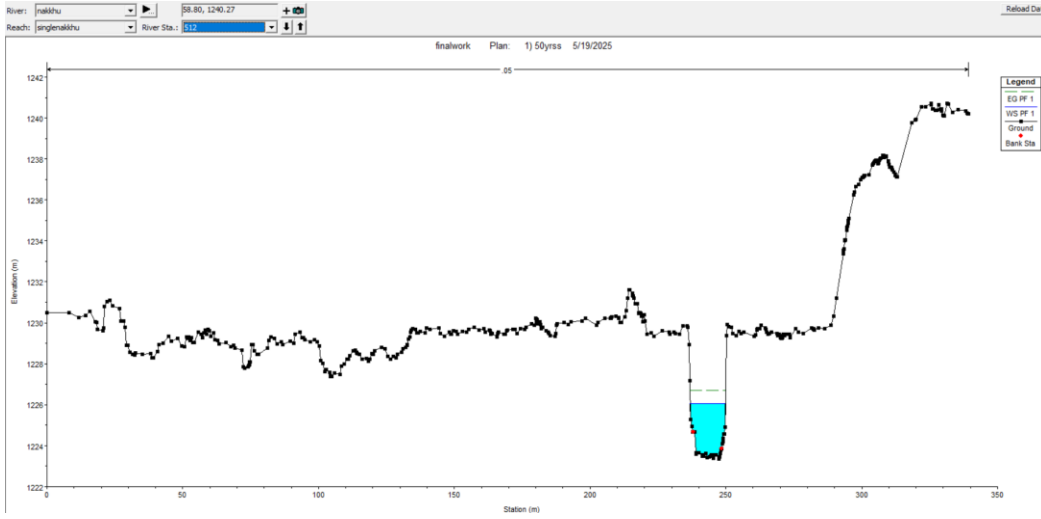


Figure 47: Cross section of mid-nakkhu for 50 year return period

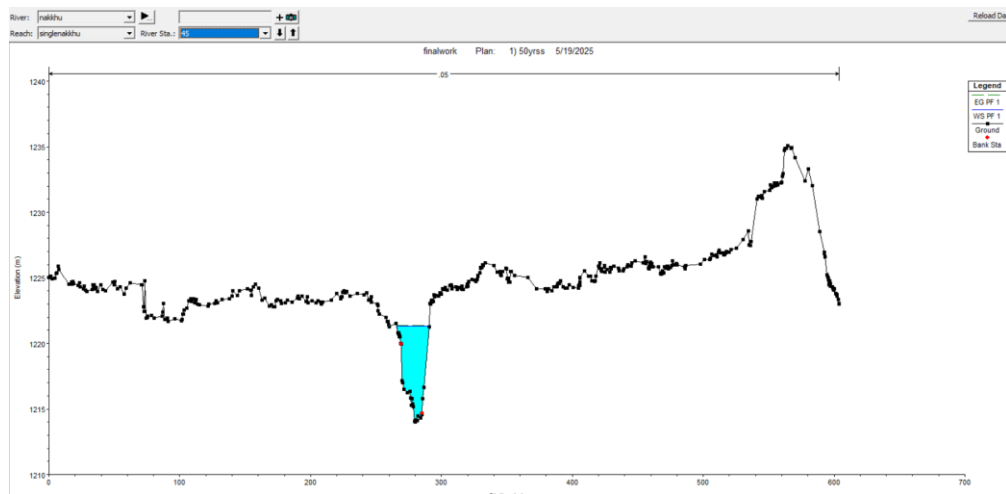
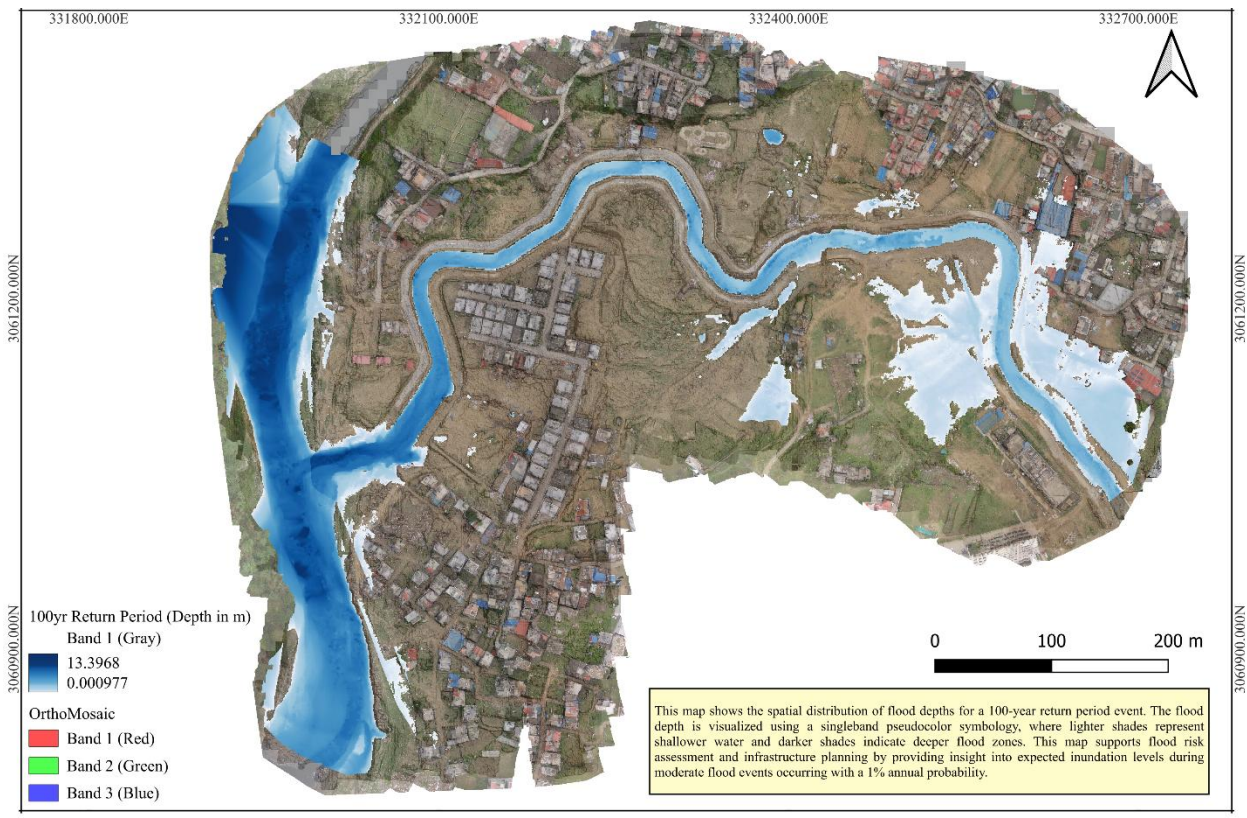


Figure 48: Cross section around Bagmati-Nakku confluence for 50 year return period

6.1.5 100 Years Return Period

The flood inundation map for a 100-year return period indicates significant increases in the water depth for the Bagmati and Nakku rivers. More specifically, the area upstream from the Nakku River almost has a large inundation area, due to water not being able to flow away as fast in the flat terrain compared to the steeper terrain downstream. The map shows a lot of overflow in the confluence area, with water traveling towards the nearby settlements. This confirms the need for better drainage in that area because from the findings we discussed we could see that uncontrolled overflows could inundate the greater area. So, based on this, we suggest that the flood event on September, 27, 2024 appears to satisfy the characteristics of a 100-year return period flood.



INUNDATION MODELLING AND FLOOD HAZARD MAPPING : A CASE STUDY OF BAGMATI-NAKKHU CONFLUENCE

P. Baral, R. Khatriwada, S. Kharal, S. Nepal, A. Chand, R. Maskey, R. Shrestha

Figure 49: Inundation map for 100 year return period

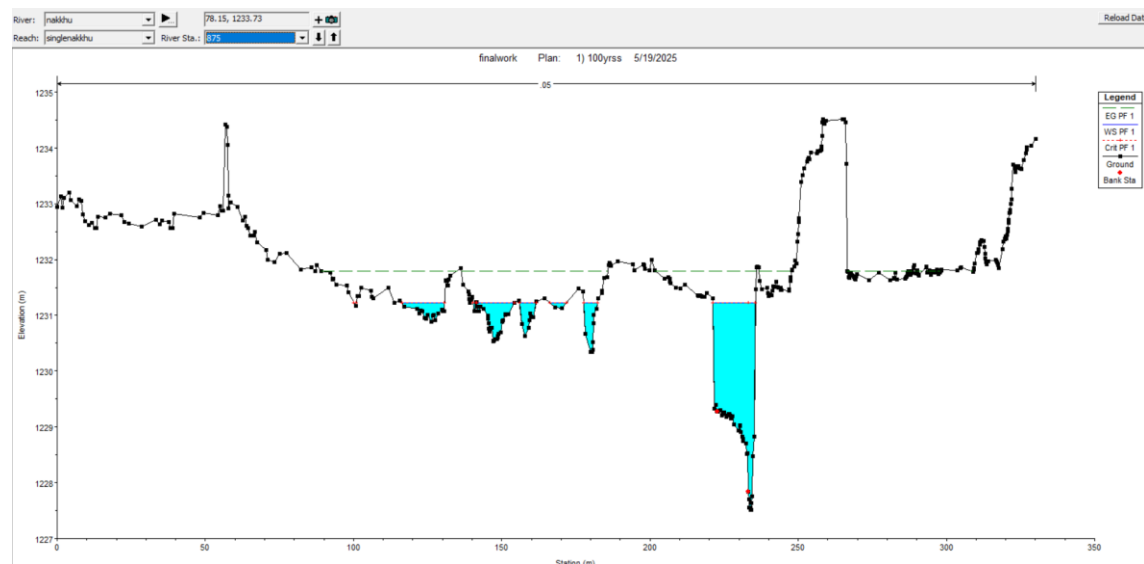


Figure 50: Cross section of upstream part of Nakku for 100 year return period

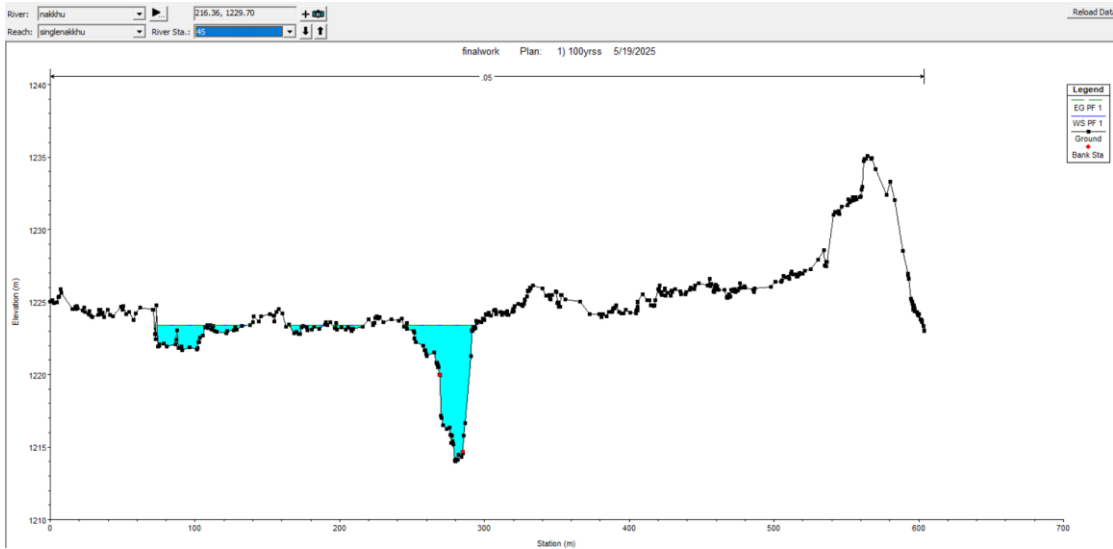


Figure 51: Cross section around Bagmati-Nakkhu confluence for 100 year return period

6.1.6 150 Years Return Period

The inundation map for the 150-year return period shows a marked increase in inundation severity when compared to lower return periods. The depth of water has increased profoundly along both the Bagmati and Nakkhu rivers, especially in the upstream areas of the Nakkhu River. This is likely due to the less steep and flatter terrain allowing for water to collect more easily. At the Bagmati-Nakkhu confluence, the overflow had further to span, and it even encroached further into the adjacent settlement and buildings. There has been both a greater spread and depth of inundation in this area, which implies growing threats to urban settings if drainage and flood control are not implemented.

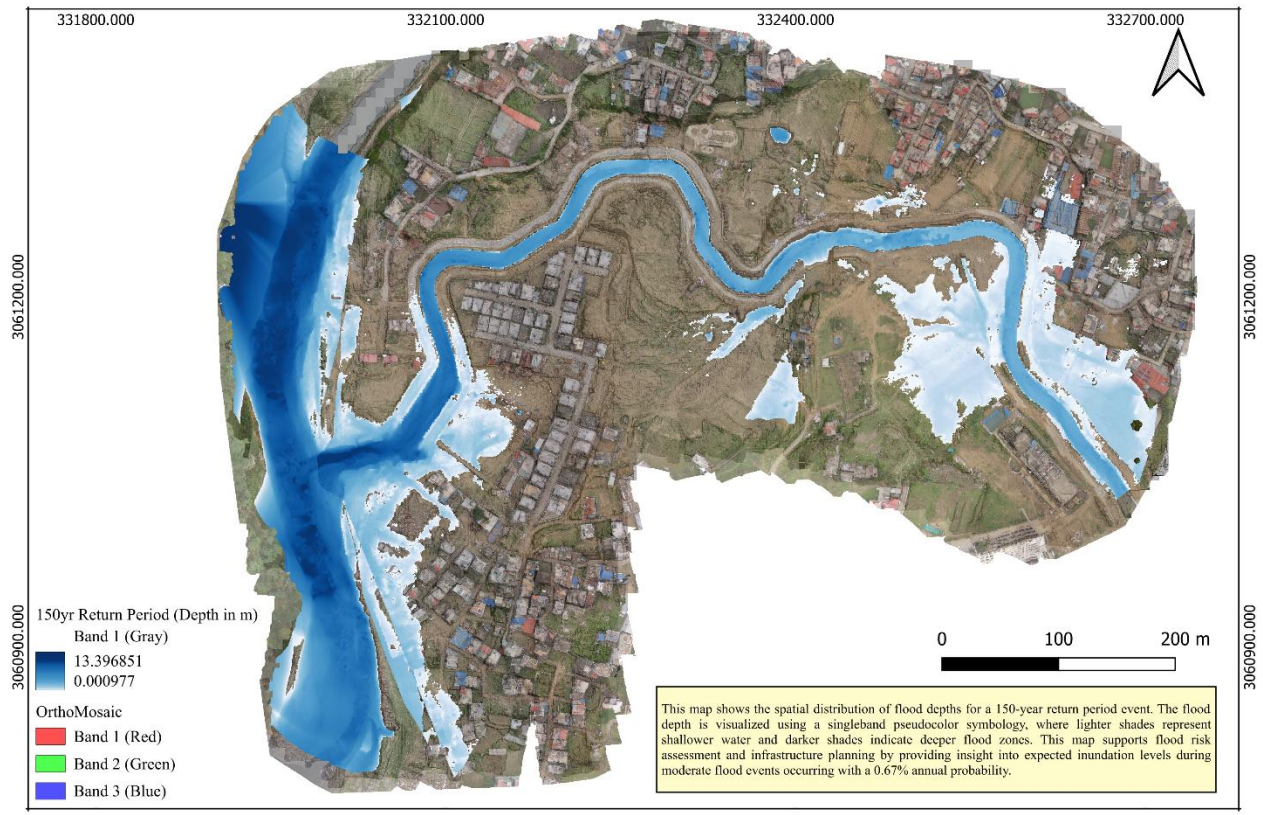


Figure 52: Inundation map for 150 year return period

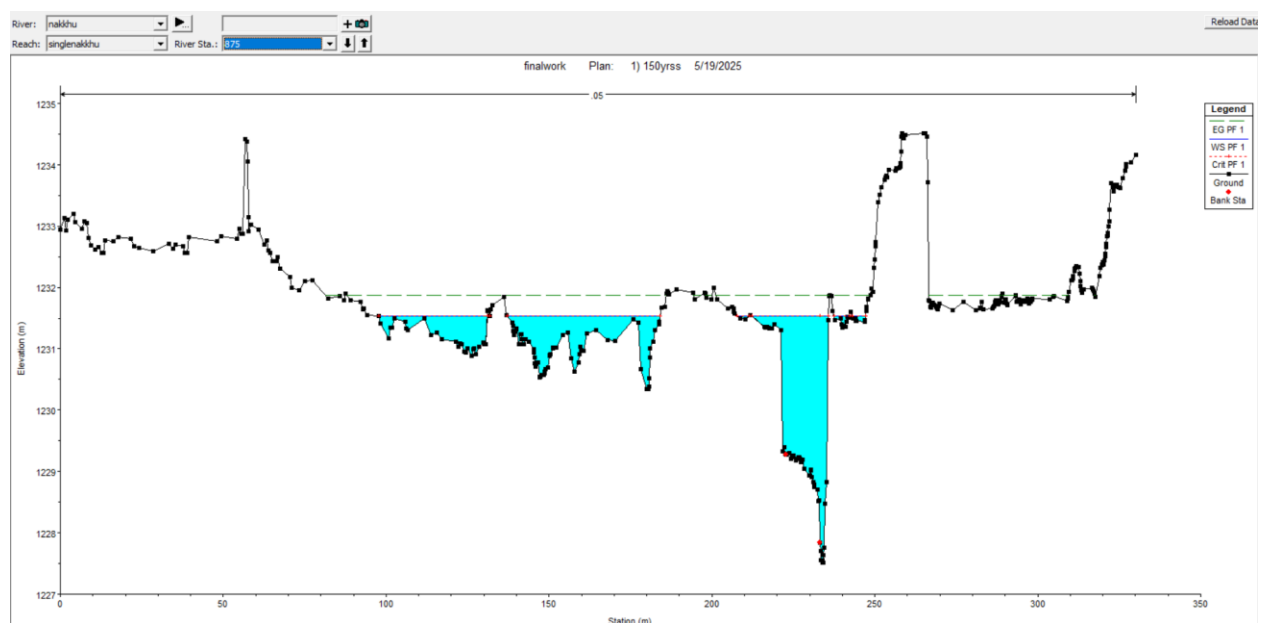


Figure 53: Cross section of upstream part of Nakku for 150 year return period

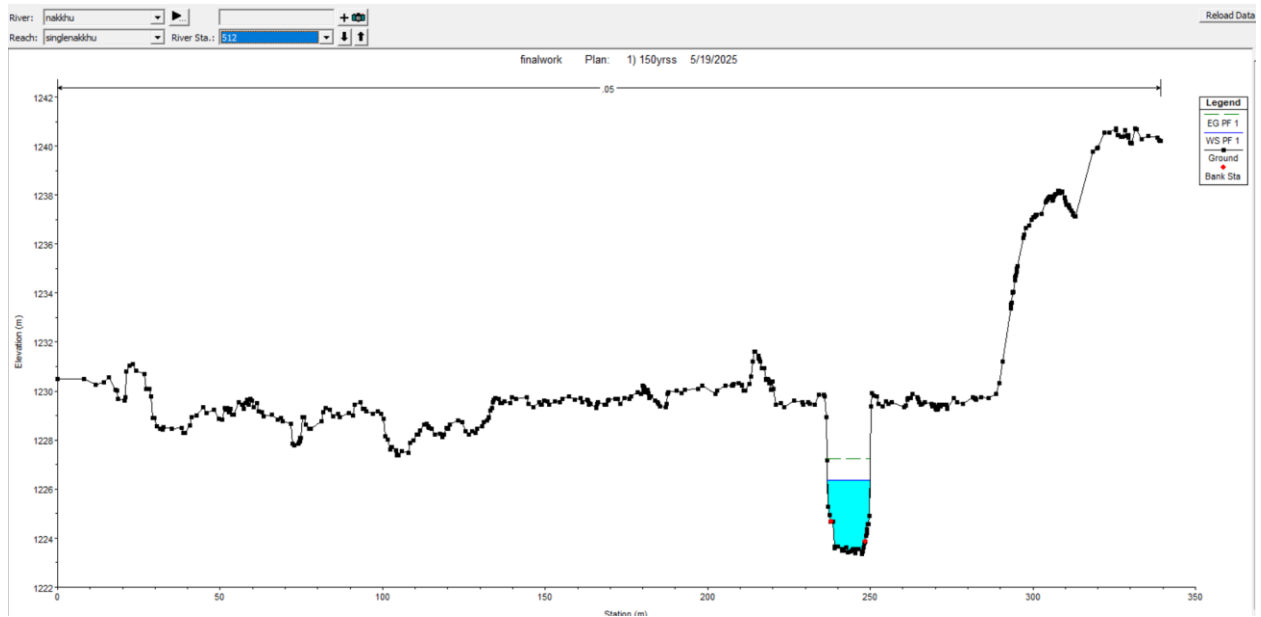


Figure 54: Cross section of mid-nakkhu for 150 year return period

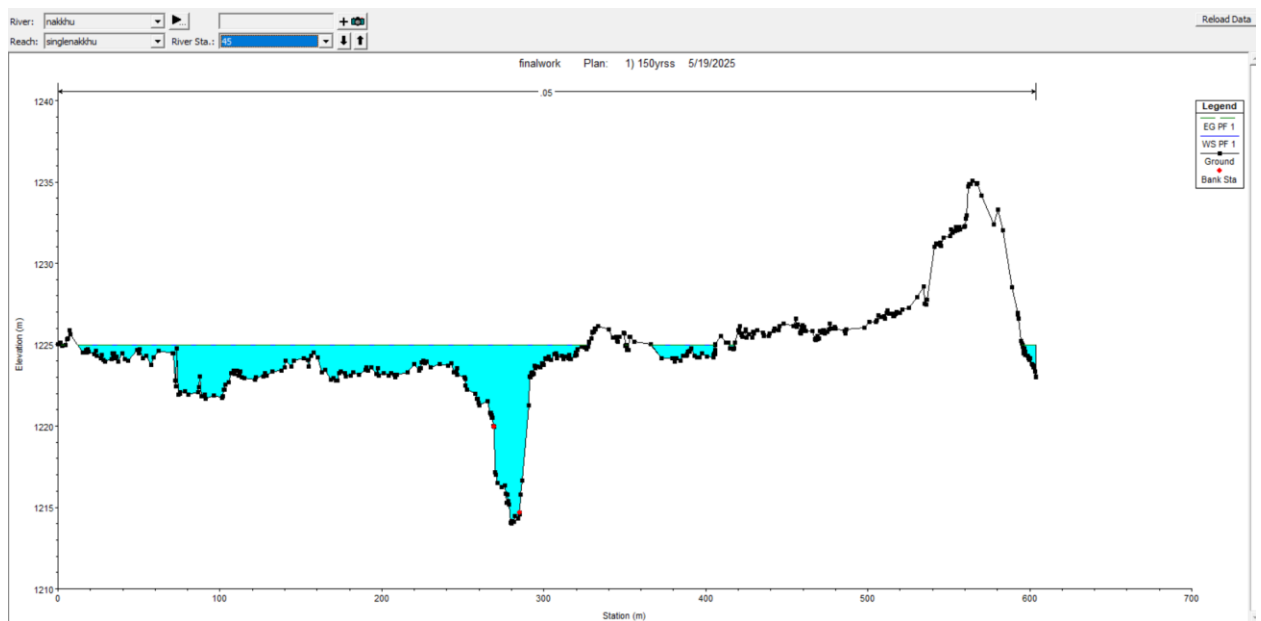


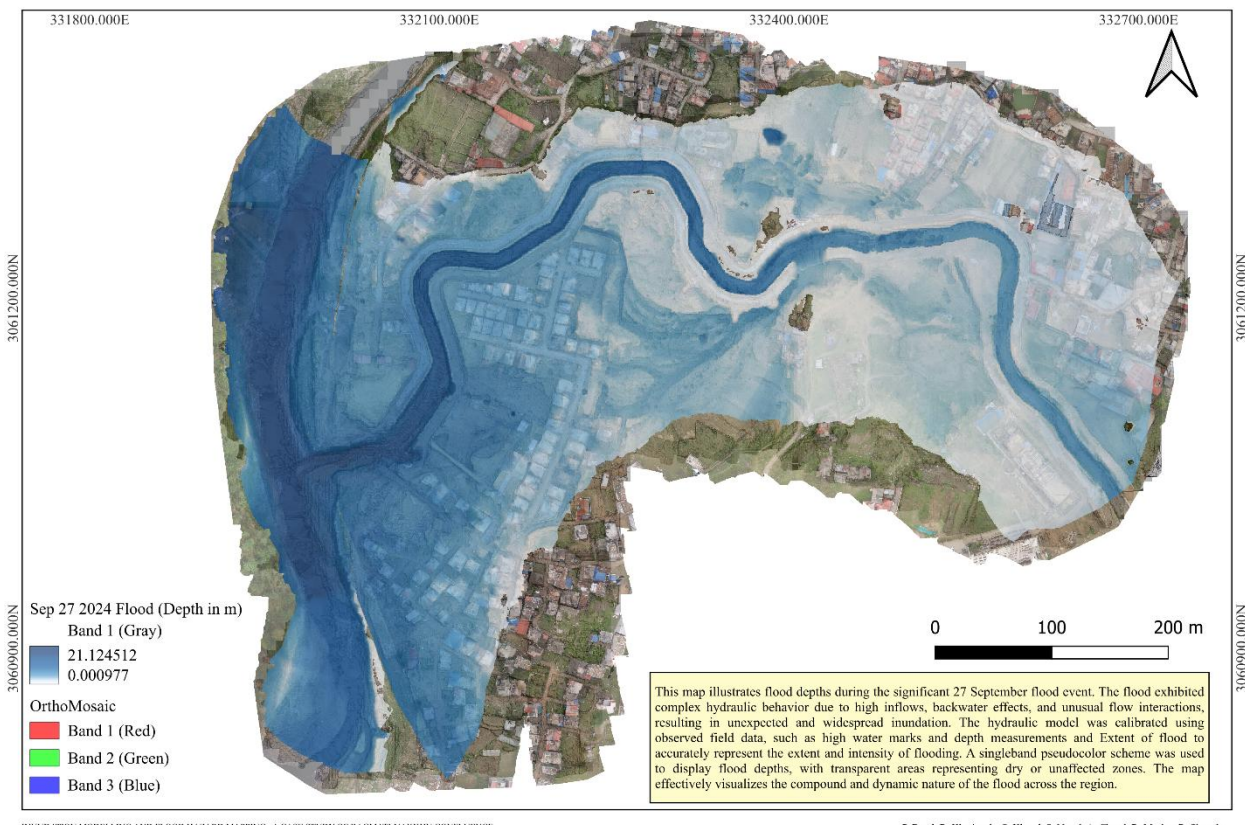
Figure 55: Cross section around Bagmati-Nakkhu confluence for 150 year return period

6.1.7 Inundation Map of 27th September

The flood inundation map indicates places and flooding depths observed on 27 September 2024 in the Kathmandu Valley. This came after a heavy downpour, over 320 mm of rainfall within a 24-hour period, record breaking in a one-day quantity since at least 1970. Nepal's Department of Hydrology and Meteorology indicated that the majority of the Kathmandu stations recorded the maximum quantity of rainfall in a single day in their 54-year records (World Weather Attribution, 2024). This event has a return period of about 100 years.

The September 27th flood was modeled using HEC-RAS with discharge values calibrated based on high water marks observed during a field survey. To simulate the flood extent and depth accurately, a discharge of 2,000 m³/s was used for the Nakkhu River. For the Bagmati River a discharge of 3,000 m³/s was applied upstream of the confluence, increasing to 4,500 m³/s downstream of the confluence. While these are not the actual measured discharges, they were selected to best match the observed flood extent. The map below shows the calibrated inundation extent for the September 27th event.

The map illustrates the spatial extent of the inundation, where different colors of blue correspond to different depths of flooding (measured in meters) as shown in the legend. An important factor that exacerbated this flooding was the narrow Chobhar gorge, which limited the flow of the river and created backwater conditions which caused significant upstream flooding. In addition to hydrological aspects, the degree of urbanization and deforestation in the Kathmandu Valley has had a cumulative long-term effect on the land's ability to absorb water resulting in increased surface runoff. Ultimately all of these factors resulted in flooding with greater intensity and extent than was commonly associated with previous floods in this area of the valley. The map demonstrates the interplay of extreme weather, geographic constraints, and land use changes.



INUNDATION MODELLING AND FLOOD HAZARD MAPPING : A CASE STUDY OF BAGMATI-NAKKHU CONFLUENCE

P. Baral, R. Khatiwada, S. Kharel, S. Nepal, A. Chand, R. Maskey, R. Shrestha

Figure 56: Inundation map of 27th September flood

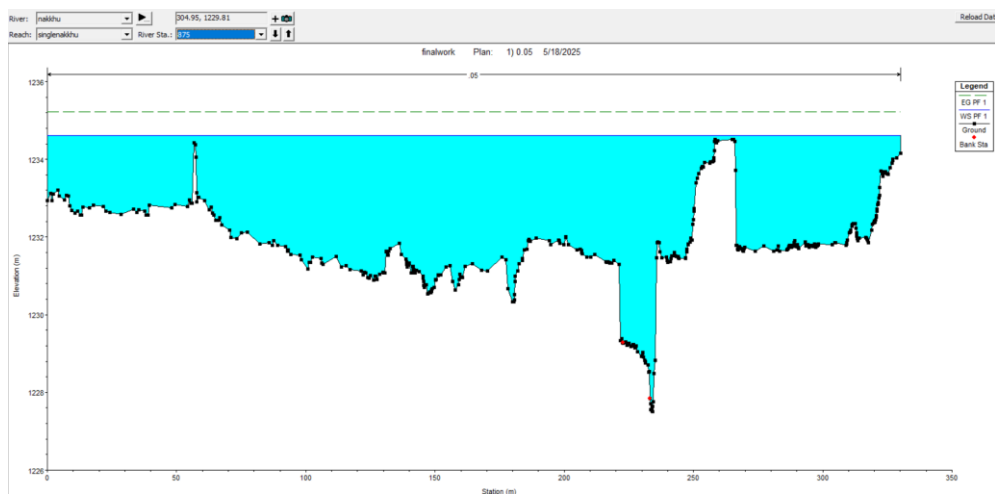


Figure 57: Cross section of upstream part of Nakkhu

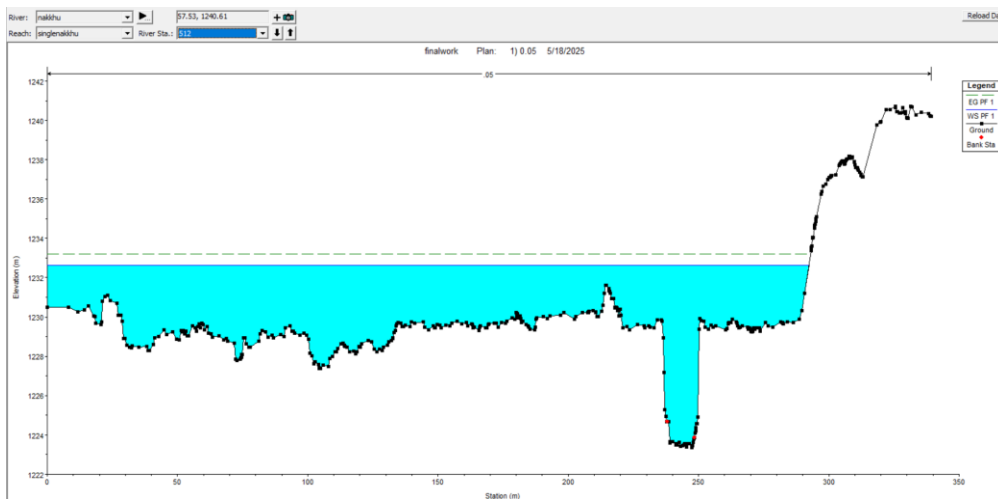


Figure 58: Cross section for mid-nakkhu

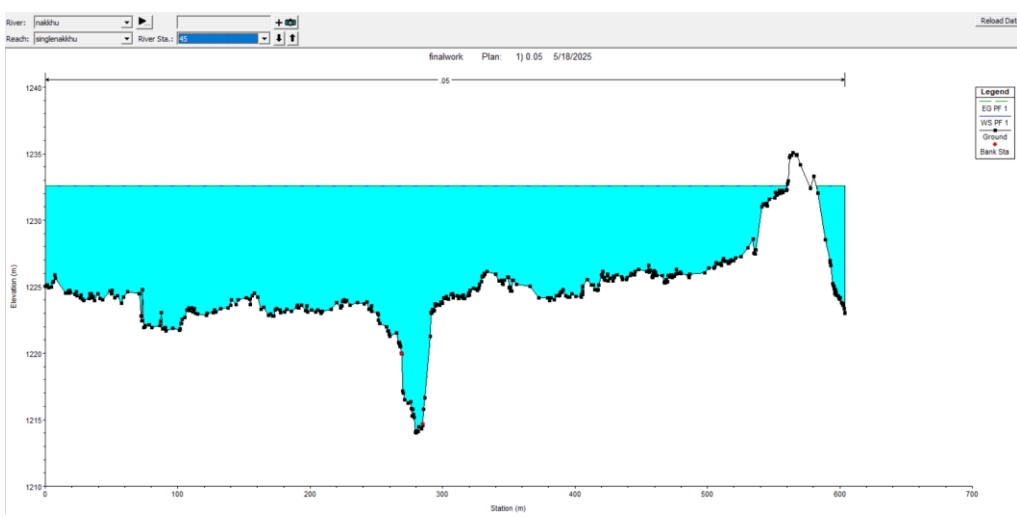


Figure 59: Cross section for Bagmati-Nakkhu Confluence

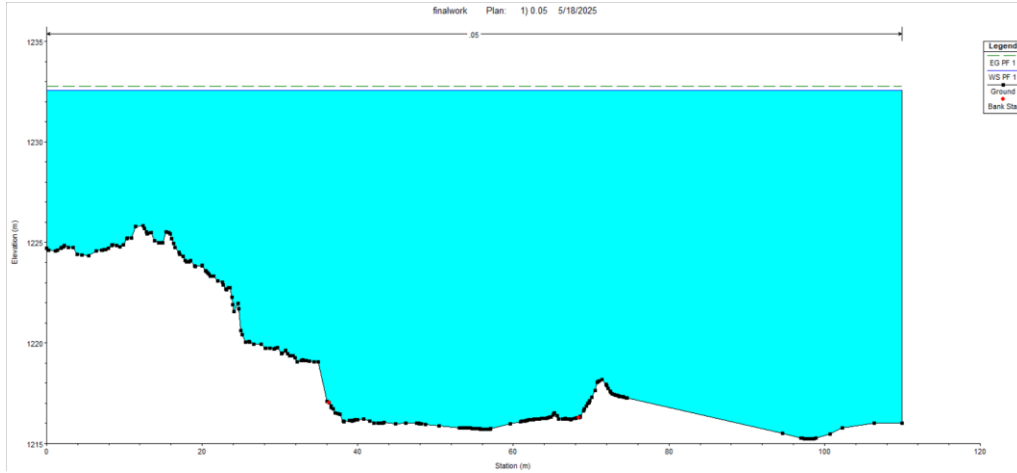


Figure 60: Cross section of Bagmati before confluence

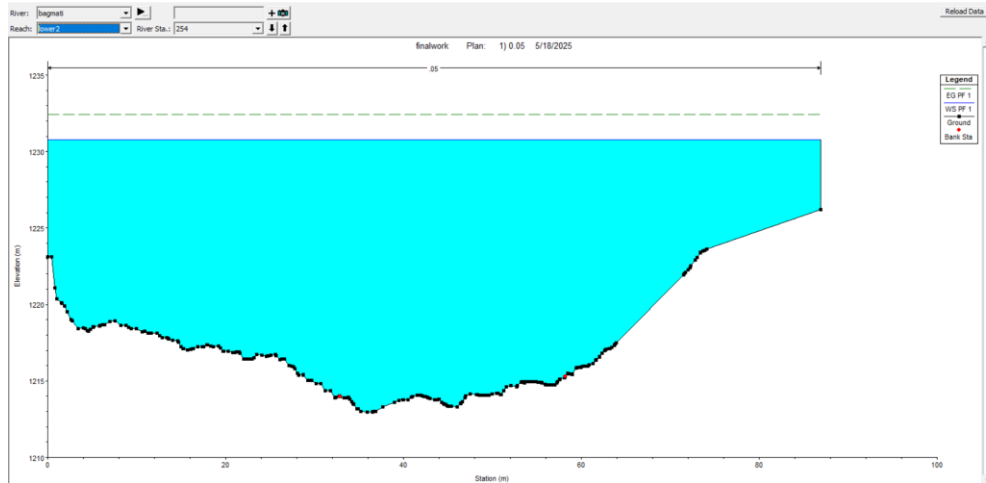
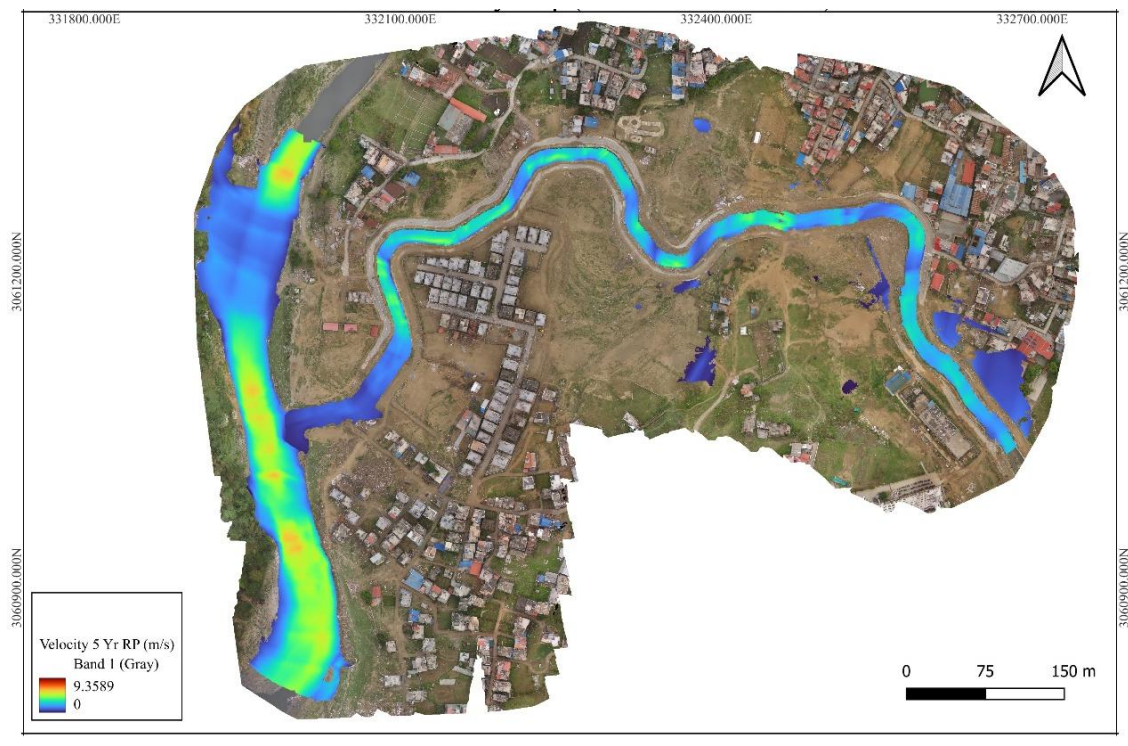


Figure 61: Cross section of Bagmati after confluence

6.1.8 Backwater effect at the Bagmati-Nakkhu Confluence

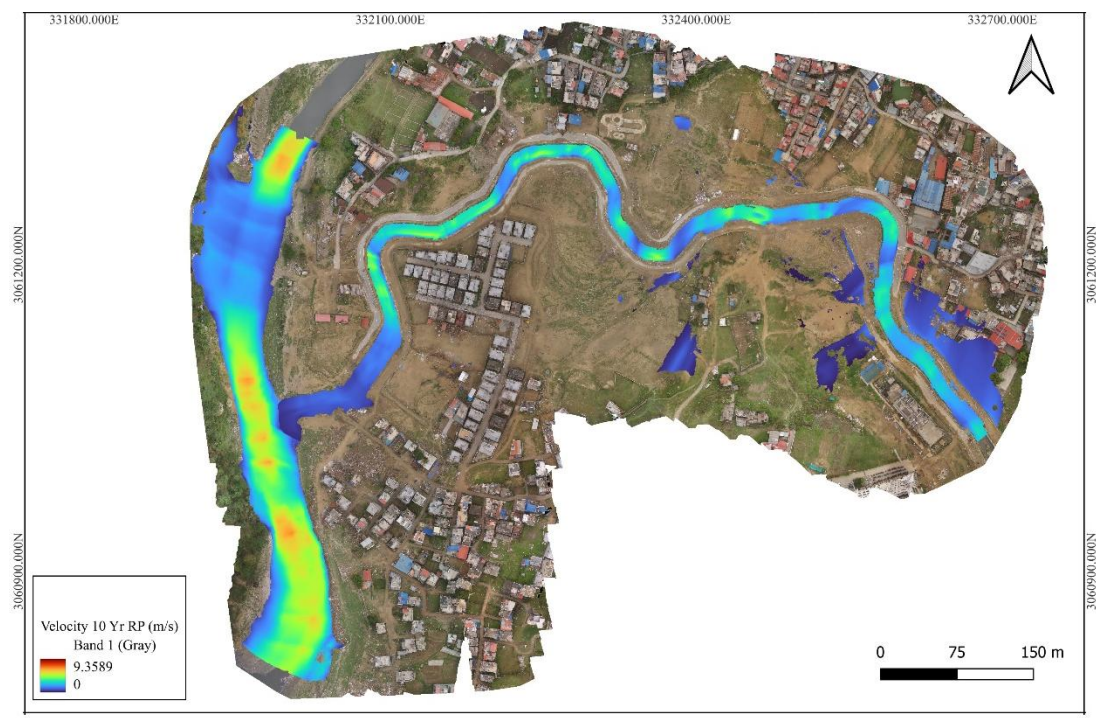
In the 5-year, 10-year and 25-year return period scenarios, velocity magnitudes in both rivers remain relatively low and stable with the velocity of around 2-3 m/s around the confluence. The Nakkhu River merges smoothly with the Bagmati, and there is no significant hydraulic obstruction or reversal. As a result, no backwater effects are observed, and inundation is mostly confined to upstream bare lands, with minimal risk to settlements.

In the 5-year, 10-year and 25-year return period scenarios, velocity magnitudes in both rivers remain relatively low and stable with the velocity of around 2-3 m/s around the confluence. The Nakkhu River merges smoothly with the Bagmati, and there is no significant hydraulic obstruction or reversal. As a result, no backwater effects are observed, and inundation is mostly confined to upstream bare lands, with minimal risk to settlements.



INUNDATION MODELLING AND FLOOD HAZARD MAPPING : A CASE STUDY OF BAGMATI-NAKKHU CONFLUENCE P. Baral, R. Khatiwada, S. Kharel, S. Nepal, A. Chand, R. Maskey, R. Shrestha

Figure 62: Flood Velocity map for 5 year return period



INUNDATION MODELLING AND FLOOD HAZARD MAPPING : A CASE STUDY OF BAGMATI-NAKKHU CONFLUENCE P. Baral, R. Khatiwada, S. Kharel, S. Nepal, A. Chand, R. Maskey, R. Shrestha

Figure 63: Flood Velocity map for 10 year return perio

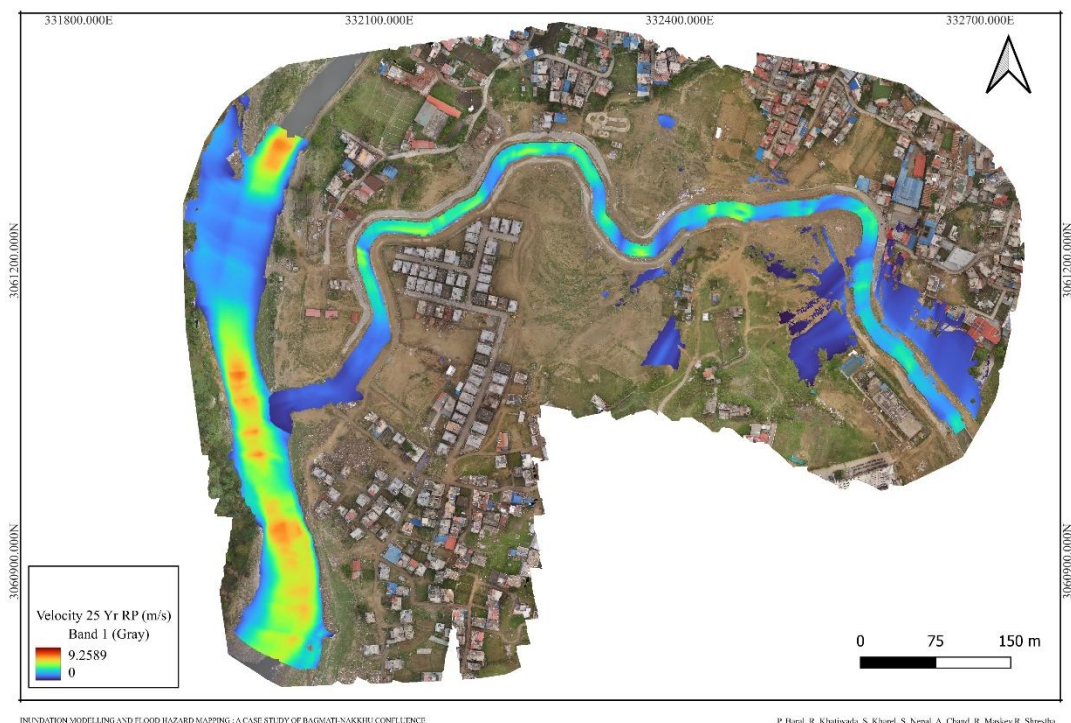


Figure 64: Flood Velocity map for 25 year return period

At the 50-year return period, early signs of hydraulic resistance at the confluence begin to emerge. The velocity in the Bagmati River increases significantly, while the Nakkhu River's flow begins to slow down near the junction with the velocity around 0.5-1 m/s, indicating initial flow impedance. This causes water to accumulate along the Nakkhu's banks increasing the flood extent slightly and posing a potential threat to nearby settlement areas, especially if flow rates surge beyond the simulated discharge.

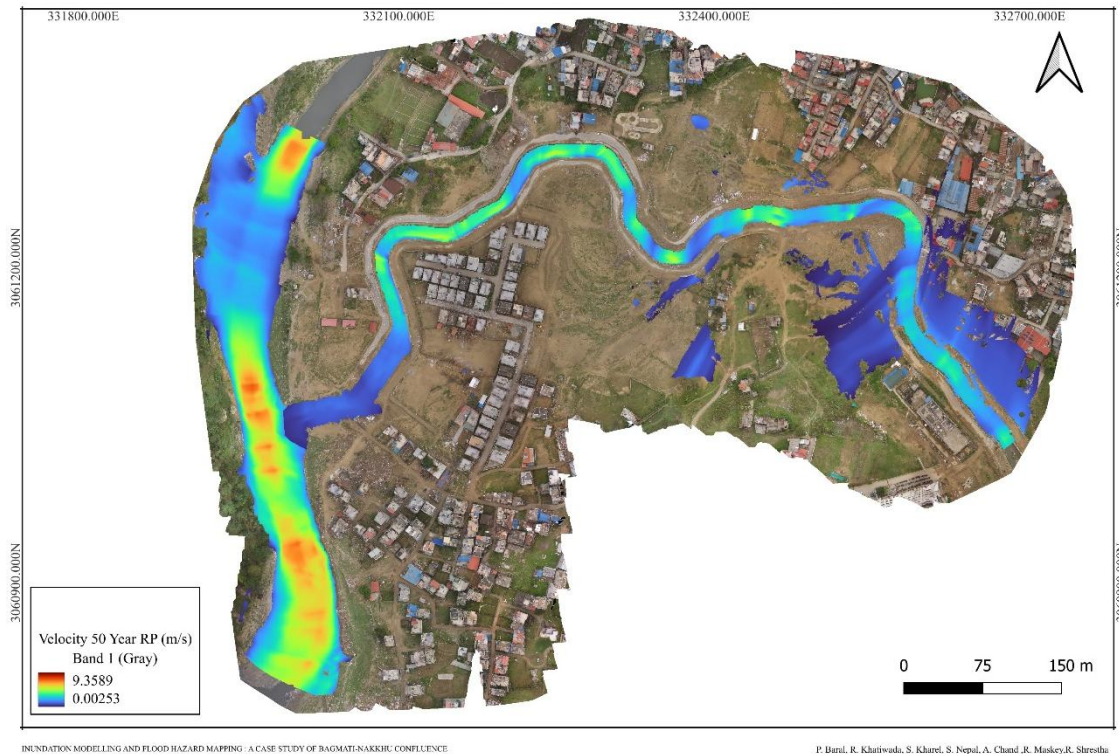


Figure 65: Flood Velocity map for 50 year return period

In the 100-year and 150-year return period scenarios the backwater effect becomes pronounced. The Bagmati River's high velocity and flow volume exert significant hydraulic resistance causing the Nakkhu River's water to back up before merging. This is visible in the velocity map where a sharp velocity gradient forms near the confluence and flow direction vectors on the Nakkhu side become erratic or stagnated. This hydraulic condition leads to elevated water levels upstream and significantly contributes to high hazard zones forming near settlements, particularly on the Nakkhu side.

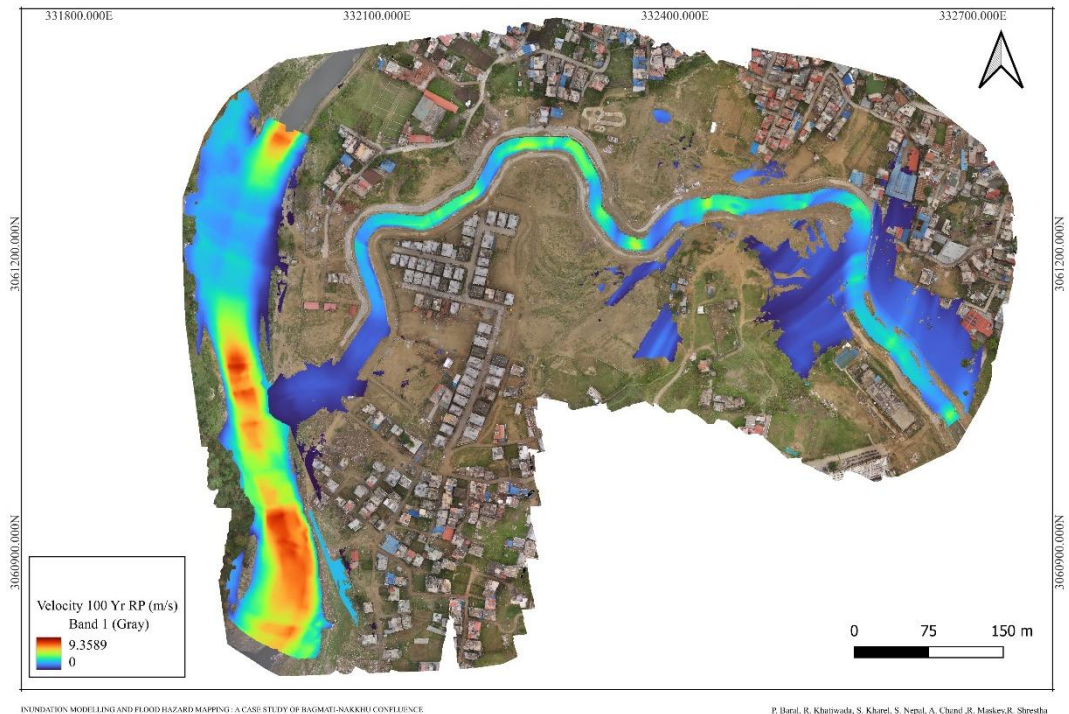


Figure 66: Flood Velocity map for 100 year return period

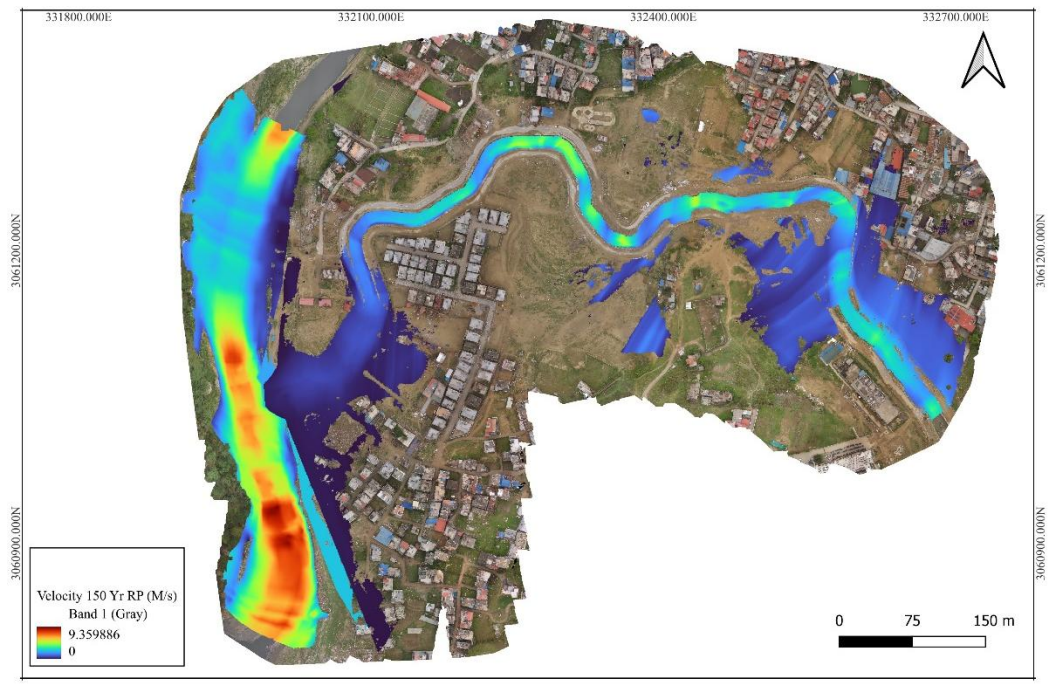


Figure 67: Flood Velocity map for 150 year return period

These backwater-induced inundation patterns align closely with observations from the September 27, 2024 flood which caused severe damage in the confluence area. Model calibration for that event required increasing the discharge to match the observed flood extent, further indicating its

intensity was greater than a typical 100-year event. The flood marks, local briefings, and velocity-based simulation all support the conclusion that the backwater effect was a primary cause of hazard escalation during the September flood.

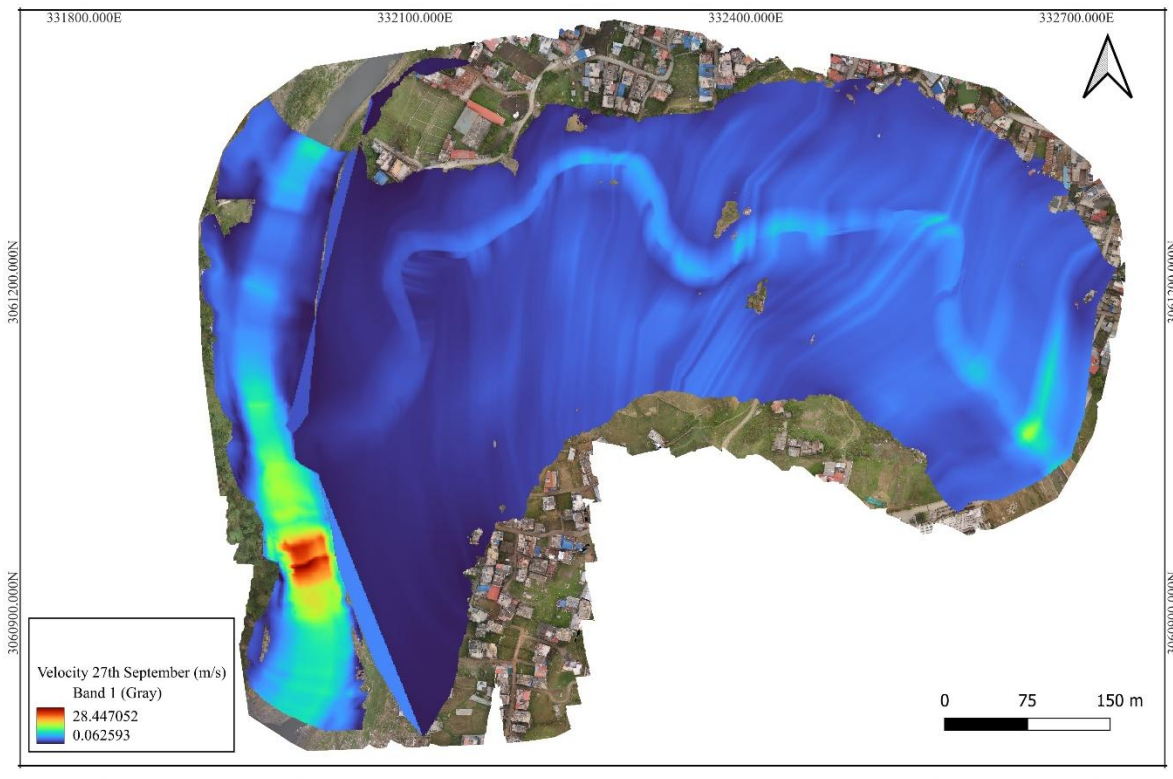


Figure 68: Flood Velocity map for 27 September 2024

6.2 Flood Hazard Mapping

6.2.1 5 Years Return Period

In the 5-year return period flood scenario, the reclassified flood height raster indicates that most of the flooded area is classified as low hazard (< 2 m) which is approximately 0.5109 km². The moderate hazard (2–4 m) and high hazard (4–8 m) classes are approximately 0.0180 km² and 0.0133 km². The results suggest that for frequent flood events, the inundation depth is shallow and there are only a few small areas that are experiencing moderate to high flood hazard. Importantly, the flood hazard map shows that moderate and high hazard areas do not intersect with any residential settlements, suggesting that frequent, lower-magnitude flood events do not pose a significant threat to populated areas in the study region.

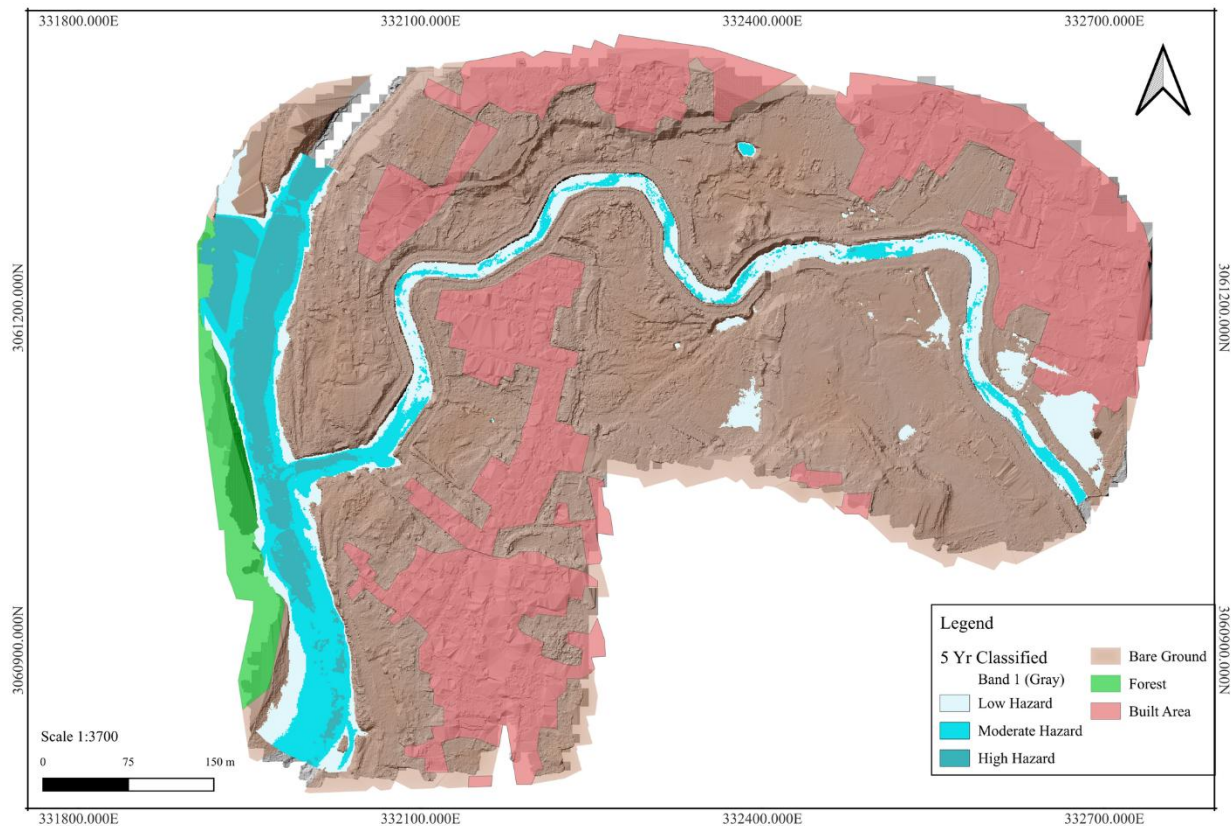


Figure 69: Flood Hazard Map for 5 year return period

6.2.2 10 Years Return Period

In the 10-year return period flood scenario, the reclassified flood depth raster shows that most of the inundated area has been classified as low hazard (<2 m) encompassing approximately 0.5061 km². The moderate (2–4 m) and high (4–8 m) hazard classes are approximately 0.0185 km² and 0.0177 km² respectively. The results suggest shallow flooding as the primary impact of moderate flood events while moderate and high flood hazard areas are smaller portions of inundation. Similar to the 5-year scenario, moderate (2–4 m) and high (4–8 m) hazard areas are minimal in extent and do not affect any residential settlements. This suggests that under a 10-year flood event

the risk to populated areas remains negligible. However low hazard is largely constrained to open areas on the upstream side.

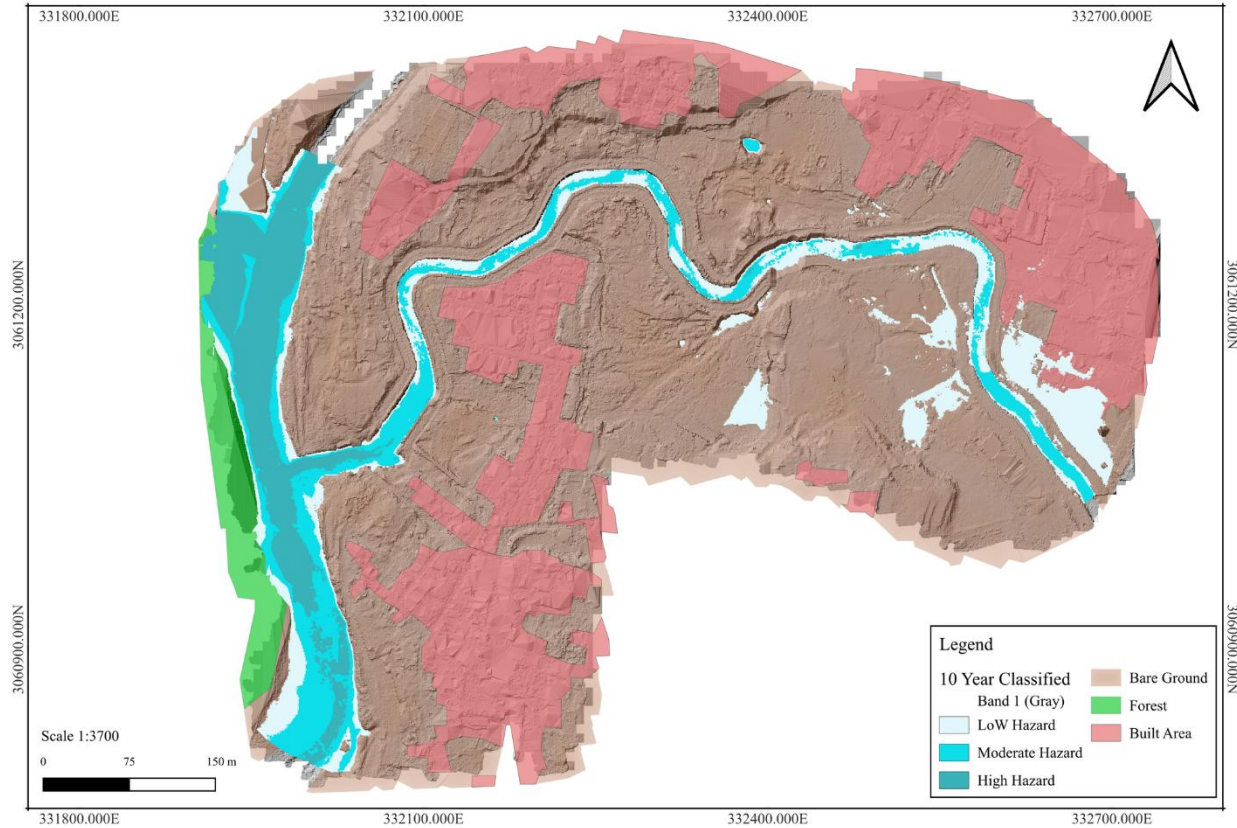


Figure 70: Flood Hazard Map for 10 year return period

6.2.3 25 Years Return Period

The majority of the flooded region, or roughly 0.5020 km², is classed as low hazard (<2 m), according to the flood depth raster reclassified by hazard classification for the flood event that occurred during the 25-year return period. A small area of the extremely high danger class (8-12 m) represents only 0.0004 km², while the areas classed as moderate (2-4 m) and high (4-8 m) represent 0.0181 km² and 0.0217 km², respectively. According to these results, the extent of moderate to high flood threats somewhat increases with an increase in return period, with shallow flooding continuing to be the most common. The reclassified flood height raster continues to show that low hazard zones dominate the inundated area, particularly affecting bare ground in the upstream part of the Nakkhu region. The spatial extent of moderate and high hazard zones slightly increases compared to lower return periods, but these zones are still limited in distribution and do not extend into residential settlements. Consequently, the risk to populated areas remains low and the hazard is primarily confined to non-residential open areas. This suggests that even under a 25-year flood event, while the low hazard footprint expands to bare ground settlements do not yet face significant flood hazard exposure.

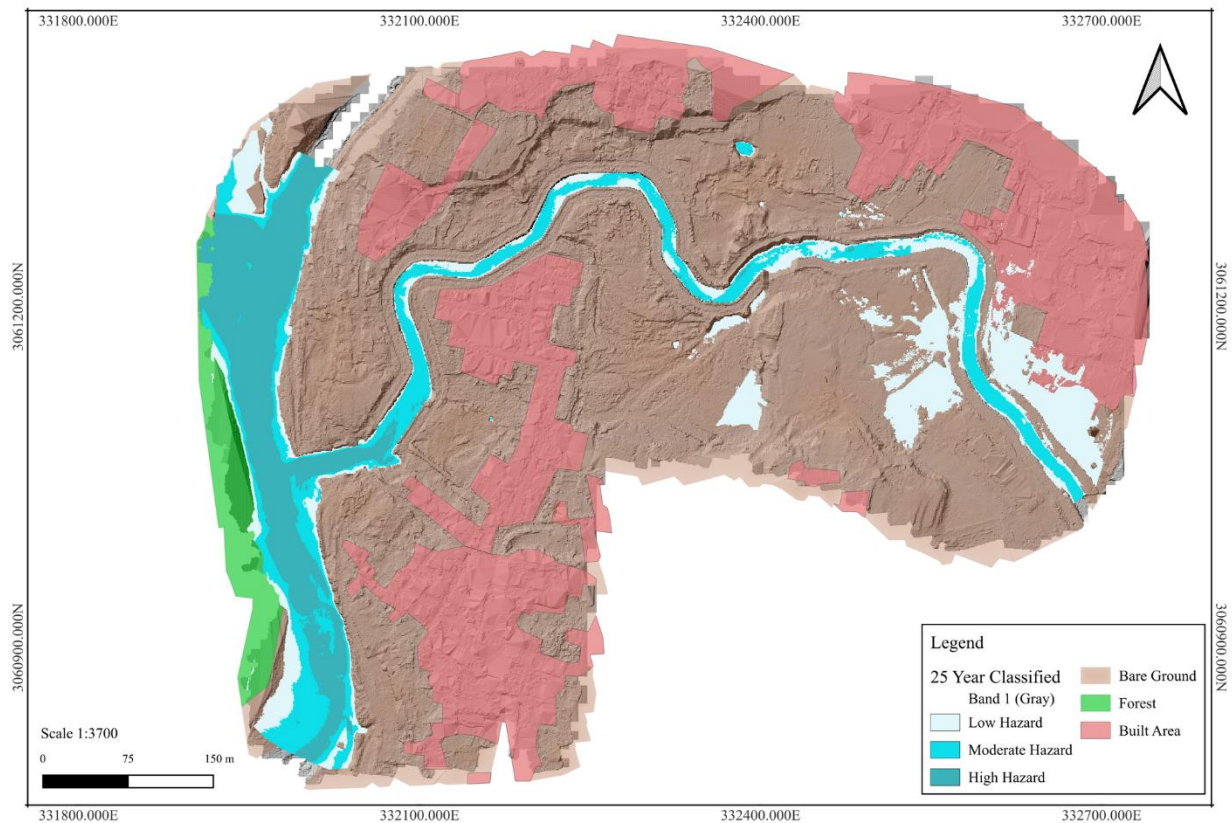


Figure 71: Flood Hazard Map for 25 year return period

6.2.4 50 Years Return Period

The flood depth raster for the 50-year return period flood scenario suggests that most of the inundated area fell within the low hazard class (<2 m), approximately 0.4994 km². The areas of moderate hazard (2–4 m) and high hazard (4–8 m) area were found to be 0.0183 km² and 0.0238 km², respectively, and a very small area (<0.0008 km²) was accounted for the very high hazard levels (8–12 m). Overall, the results indicate that as return period flood hazards became less frequent (longer return period flood scenario), moderate to high flood hazard areas increased in extent, and generally increased in water depth, although the low-depth flooding was proving to be the majority presence of the flood hazard areas. In the 50-year return period scenario low hazard flooding continues to affect bare ground in the upstream Nakkhu area. Moderate hazard zones emerge along the riverbanks and while they do not yet inundate settlements, their proximity to residential areas suggests a potential risk of spillover. This indicates increasing flood exposure near the banklines and highlights the need for preventive measures in adjacent settlements.

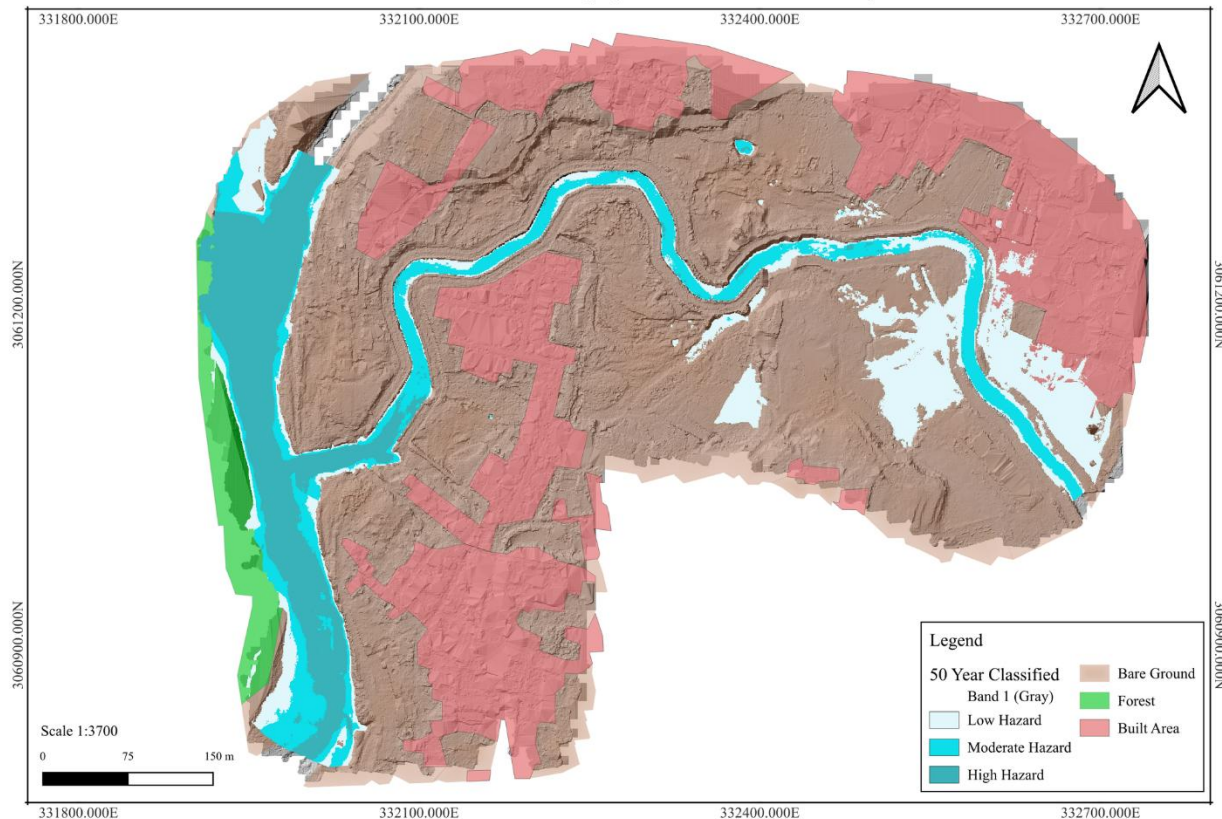


Figure 72: Flood Hazard Map for 50 year return period

6.2.5 100 Years Return Period

The reclassified flood depth raster for the 100-year return period flood scenario shows that a large proportion of the inundated area falls within the low hazard category (<2 m) with a size of roughly 0.4928 km². The moderate (2–4 m) and high hazard (4–8 m) classes are very limited in size, with areas of 0.0160 km² and of 0.0225 km², respectively, while the very high hazard class (8–12 m) is only an area of 0.0110 km². These results suggest that although the area affected by severe flooding is quite limited, a large proportion of the area is within the moderate to high flood hazard classes.

In the 100-year return period scenario, significant inundation is observed with the potential for backwater effects near the Bagmati-Nakkhu confluence. This hydraulic condition can cause increased water levels and flow resistance posing a severe flood risk to nearby settlements. Notably a high hazard zone is identified approximately 40 meters upstream of the confluence along the Nakkhu River indicating a critical spill-prone area. If overtopping occurs here it could lead to floodwaters spilling into adjacent residential zones, potentially causing severe damage to infrastructure and communities.

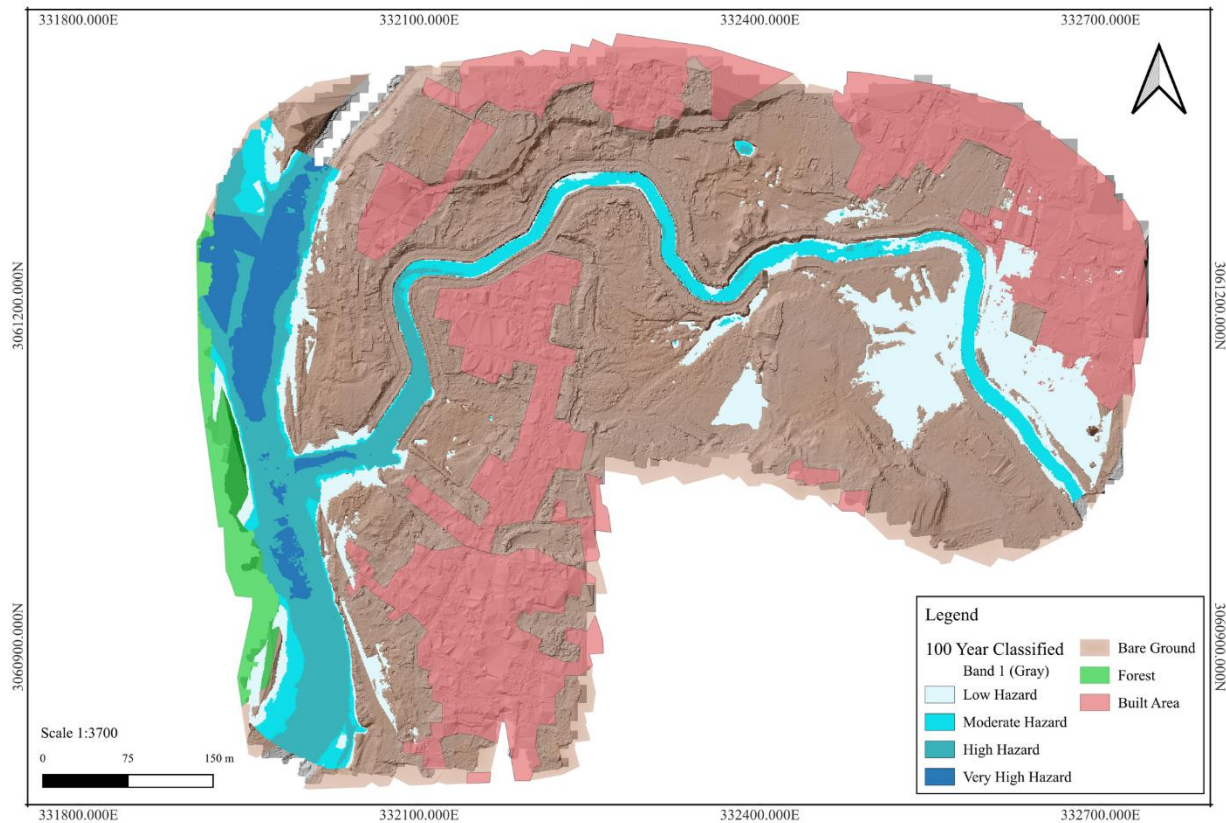


Figure 73: Flood Hazard Map for 100 year return period

6.2.6 150 Years Return Period

For the 150-year return period flood scenario, the reclassified flood depth raster shows that the majority of the total inundated area falls within the Low hazard (<2 m) area of about 0.4887 km², while the Moderate (2-4 m) hazard levels come in at only about 0.0151 km² and the High (4-8 m) hazard levels covering 0.0203 km². The Very High (8-12 m) hazard levels come in at just over around 0.0180 km² and the delineated Extreme hazard levels (>12 m) were very small making up a very small area of around 0.0002 km². Overall, the majority of flooded areas represent shallow depths but are still subjected to significant Moderate to Very High Flood hazards during more extreme events.

In this flood scenario, areas with low flood hazard are seen near the settlements close to the Bagmati-Nakkhu confluence. While these areas are currently considered low-risk, their closeness to the river and the way the two rivers meet means that flooding could become more serious during heavy flows, possibly leading to moderate or even high hazard levels. Upstream along the Nakkhu River, the flooding mostly affects open land with bare soil, showing that floods still reach non-residential areas in this part.

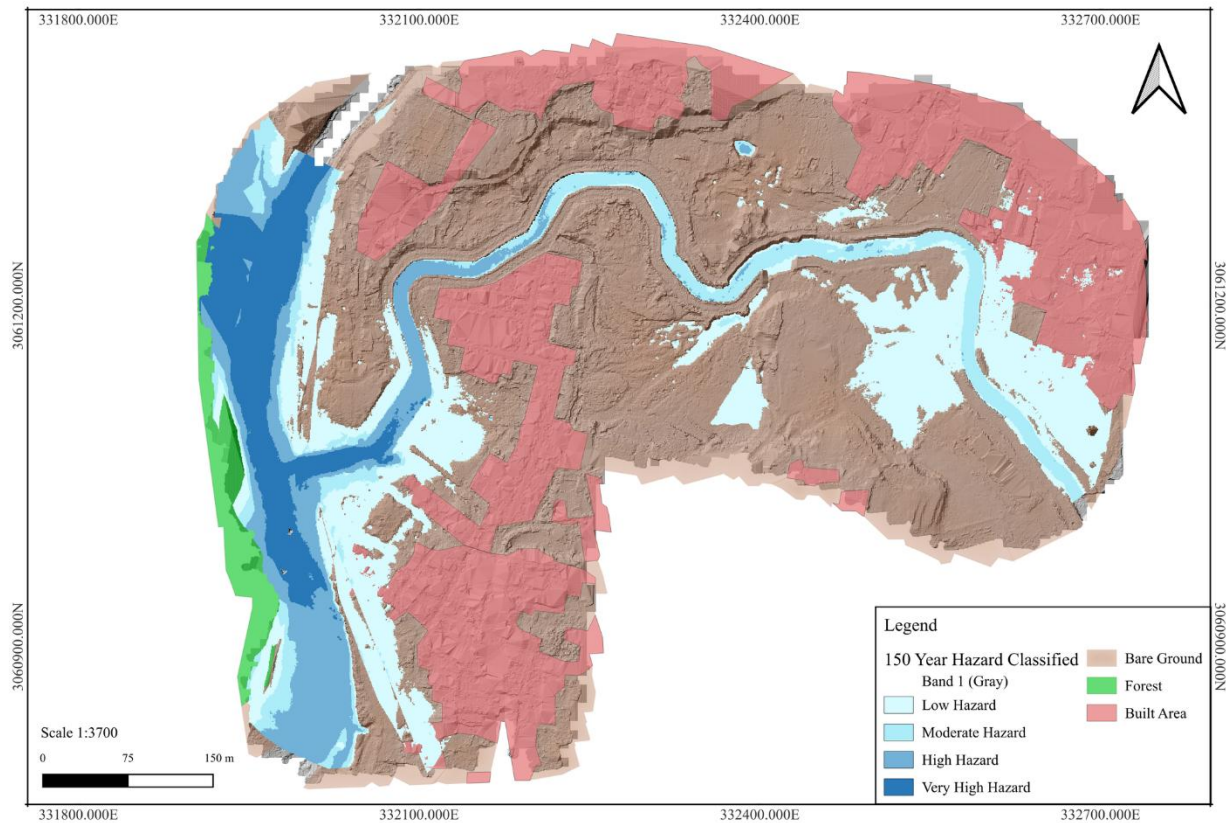


Figure 74: Flood Hazard Map for 150 year return period

6.2.7 27th September Flood Hazard Map

The assessment of flood hazards for the 27 September 2024 event show that bare soil and residential land cover types were where the greatest inundation occurred. Bare soil was by far the land cover type under low hazard (0.319 km^2 flooded), moderate hazard (0.206 km^2 flooded), and high hazard (0.158 km^2 flooded). Residential land cover areas were also inundated significant amounts with 0.110 km^2 under low hazard, 0.060 km^2 under moderate hazard, and slightly smaller surface areas under higher hazard levels. Forests, however, had little flooding with only 0.014 km^2 flooded under low hazard levels and negligible amounts flooded under the remaining higher classes.

Table 18: Area Covered by different land cover in 27th september flood

Landcover	Area covered in m ²				
	Low (<2m)	Moderate (2–4m)	High (4–8m)	Very High (8–12m)	Extreme (>12m)
Bare soil	318925	205571.25	157731.25	48981	37312
Forest	13853.5	399	399	1769.75	15129.5
Residential Area	109885.25	59849.5	59849.5	47520	2492.5

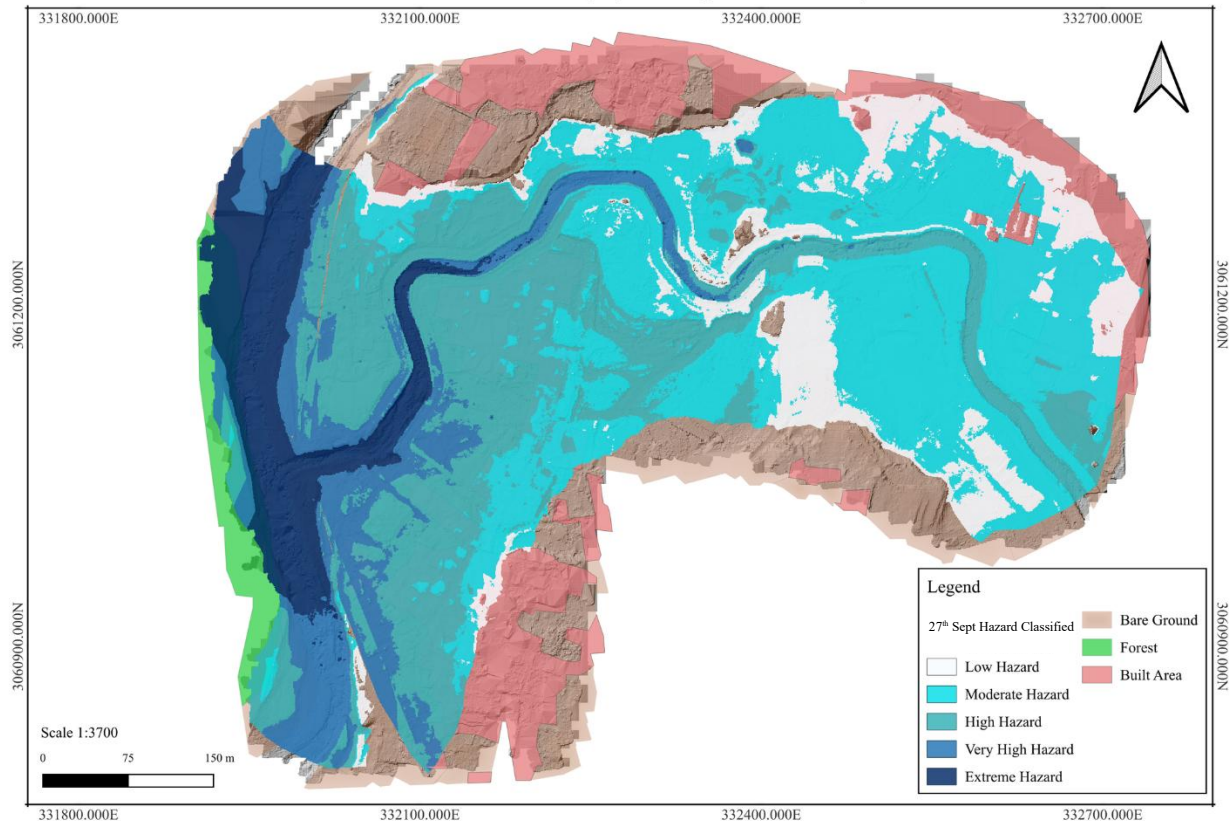


Figure 75: Flood Hazard Map of 27th September

6.3 Validation

6.3.1 Validation of HEC-RAS Flood Simulation Using Supervised Classification of Sentinel-2 Imagery

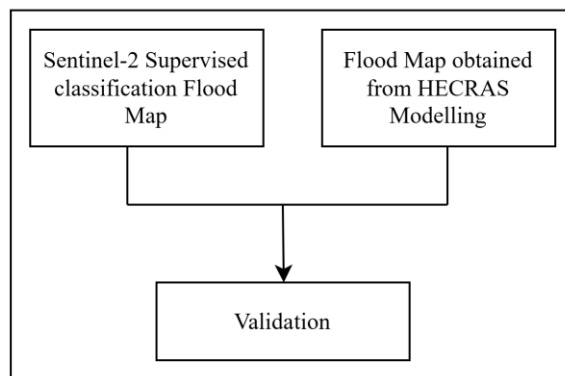


Figure 76: Validation Flowchart

The flood extent was obtained via supervised classification of a post-flood Sentinel-2 satellite imagery, while the raster of flood extent and depth was generated via the HEC-RAS hydraulic model. A comparison of the spatial analyses by the extents of the two datasets showed that the area occupied by the result of supervised classification for flood extent is approximately 0.51 km²,

while the raster's area is 0.54 km². The overlap area between the two areas is 0.50 km², and the union area is 0.55 km². This translates into an overlap percentage of 90.79%, showing a high spatial agreement between the observed satellite-based flood extent and the simulated hydraulic model-based flood extent.

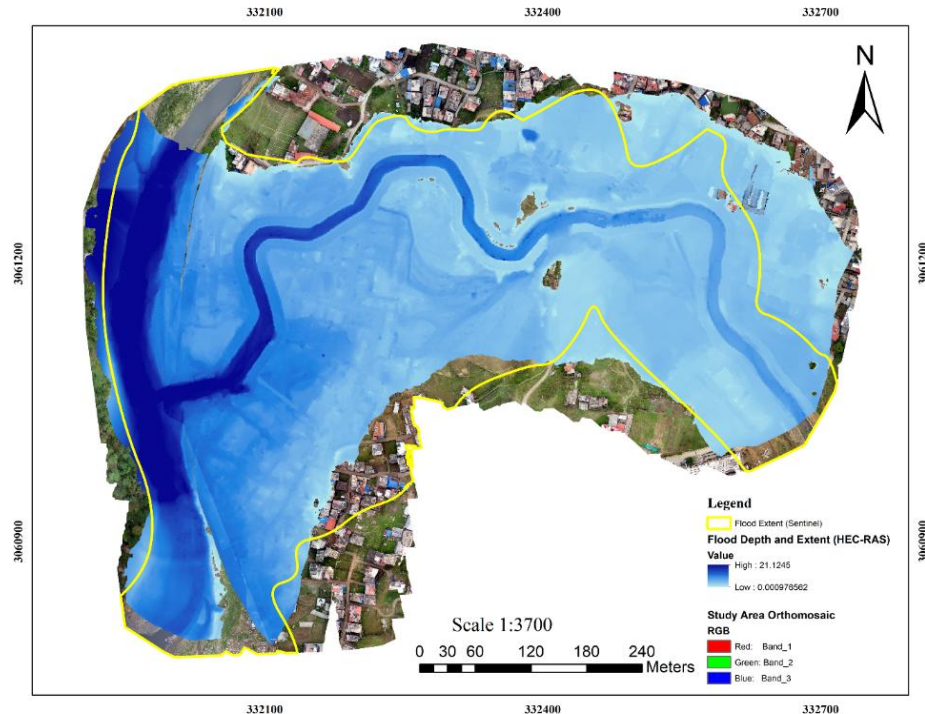


Figure 77: HEC-RAS Simulation overlayed over Supervised Classification Map

7 LIMITATIONS AND RECOMMENDATIONS

7.1 Limitations

1. The assumption of consistent watershed conditions such as soil absorption and channel roughness may not hold under intensified rainfall or land-use changes caused by climate shifts.
2. Excluding the Chobhar gorge limited the model's ability to capture backwater effects, reducing accuracy in simulating flood extent.
3. Although the Nakkhu river discharge was estimated using a calibrated HEC-HMS model, the lack of actual measured discharge data, unlike for the Bagmati River, limits the consistency of the results.
4. The time gap between the flood event on 27th September and the Sentinel-2 image on 1st October may have led to an underestimation of the actual flood extent due to receding waters.
5. HEC-RAS has technical limitations, as it excludes dynamic factors like sediment transport, debris flow, and flooded vegetation which can significantly influence flood behavior and extent.
6. HEC-HMS accuracy depends on input data quality, and low-resolution rainfall data like NASA POWER can cause errors in runoff and flood predictions.

7.2 Policy Recommendations

1. Enforce zoning laws in flood-prone areas, as hazard maps show residential zones face high inundation in 50- and 100-year floods.
2. Monitor and manage sediment buildup to maintain river capacity and reduce backwater-induced flooding like the September 27 event.
3. Design infrastructure for 100-year plus flood events, as hydraulic results reveal the September 27 flood exceeded Gumbel-predicted discharges.

7.3 Future Works

1. Inclusion of Chobhar gorge in the study area to better simulate backwater effects and improve accuracy of flood inundation mapping.
2. Validate the calibrated roughness values (Manning's Coefficient) by collecting actual ground material data.
3. Apply the same modeling approach to other rivers in Kathmandu Valley, like Karmasana, Mananati, and Manohara.
4. Further studies can be conducted to investigate the underlying causes of the extreme flooding events.

8 CONCLUSION

The aim of this research was to explore and model flood inundation and experience during events at the Bagmati-Nakkhu confluence, using a geospatial-hydrological merger approach. We created flood hazard maps following different return periods using UAV-derived high resolution DEMs, hydrological modelling with HEC-HMS, hydraulic modelling with HEC-RAS, and land cover classification from a Sentinel-2 imagery database. Results demonstrate that flood hazard risk is greatest in residential areas and that flood behavior is significantly impacted by terrain features and hydraulic interactions (backwater and obstructed flow downstream). These results reaffirm the importance of using data-driven and field calibrated approaches to assess flood risk, particularly in rapidly urbanizing, complex terrain regions like the Kathmandu Valley. There is a strong overlap between observed flood extents and the outputs from simulation, which demonstrates that our approach is useful for similar urban watersheds with flood hazards.

Revisiting the question posed at the onset, this project addressed the problem of the lack of high-resolution, field-informed flood hazard maps within Nepal, by presenting a scalable, repeatable process. This project adds to the academic conversation and provides actionable research outputs for urban planners, disaster risk managers, and policymakers.

9 REFERENCES

- Abbaspour, K. C., Vaghefi, S. A., & Srinivasan, R. (2017). A Guideline for Successful Calibration and Uncertainty Analysis for Soil and Water Assessment: A Review of Papers from the 2016 International SWAT Conference. *Water 2018, Vol. 10, Page 6, 10(1), 6.* <https://doi.org/10.3390/W10010006>
- Acharya, B., & Joshi, B. (2020). Flood frequency analysis for an ungauged Himalayan river basin using different methods: a case study of Modi Khola, Parbat, Nepal. *Meteorology Hydrology and Water Management, 8(2), 46–51.* <https://doi.org/10.26491/mhw/131092>
- Acharya, S., Hori, T., & Karki, S. (2023). Assessing the spatio-temporal impact of landuse landcover change on water yield dynamics of rapidly urbanizing Kathmandu valley watershed of Nepal. *Journal of Hydrology: Regional Studies, 50.* <https://doi.org/10.1016/J.EJRH.2023.101562>
- Adhikari, T. R., Baniya, B., Tang, Q., Talchabhadel, R., Gouli, M. R., Budhathoki, B. R., & Awasthi, R. P. (2023). Evaluation of post extreme floods in high mountain region: A case study of the Melamchi flood 2021 at the Koshi River Basin in Nepal. *Natural Hazards Research, 3(3), 437–446.* <https://doi.org/10.1016/J.NHRES.2023.07.001>
- Adhikari, T. R., & Panthee, S. (2020). Application of Hydrodynamic (HEC–RAS) Model for Extreme Flood Analysis in Far-West Province: A Case Study of Chamelia River Basin, Darchula District, Nepal. *Journal on Geoinformatics, Nepal, 9–15.* <https://doi.org/10.3126/NJG.V19I1.50961>
- Aduah, M., & Mantey, S. (2012). Remote sensing for mapping wetland floods in Kafue Flats, Zambia. *Ghana Mining Journal, 13, 33–40.* <https://www.ajol.info/index.php/gm/article/view/74971>
- Afzal, M. A., Ali, S., Nazeer, A., Khan, M. I., Waqas, M. M., Aslam, R. A., Cheema, M. J. M., Nadeem, M., Saddique, N., Muzammil, M., & Shah, A. N. (2022a). Flood Inundation Modeling by Integrating HEC–RAS and Satellite Imagery: A Case Study of the Indus River Basin. *Water (Switzerland), 14(19), 2984.* <https://doi.org/10.3390/W14192984/S1>
- Afzal, M. A., Ali, S., Nazeer, A., Khan, M. I., Waqas, M. M., Aslam, R. A., Cheema, M. J. M., Nadeem, M., Saddique, N., Muzammil, M., & Shah, A. N. (2022b). Flood Inundation Modeling by Integrating HEC–RAS and Satellite Imagery: A Case Study of the Indus River Basin. *Water, 14(19), 2984.* <https://doi.org/10.3390/W14192984
- Ahmad, H. F., Alam, A., Sultan, M., Professor, B., & Ahmad, S. (2016). One Dimensional Steady Flow Analysis Using HEC-RAS-A case of River Jhelum, Jammu and Kashmir. *European Scientific Journal, 12(32), 1857–7881.* <https://doi.org/10.19044/esj.2016.v12n32p340>
- Al Kuisi, M., Al Azzam, N., Hyarat, T., & Farhan, I. (2024a). Flood Hazard and Risk Assessment of Flash Floods for Petra Catchment Area Using Hydrological and Analytical Hierarchy (AHP) Modeling. *Water 2024, Vol. 16, Page 2283, 16(16), 2283.* <https://doi.org/10.3390/W16162283>
- Al Kuisi, M., Al Azzam, N., Hyarat, T., & Farhan, I. (2024b). Flood Hazard and Risk Assessment of Flash Floods for Petra Catchment Area Using Hydrological and Analytical Hierarchy (AHP) Modeling. *Water 2024, Vol. 16, Page 2283, 16(16), 2283.* <https://doi.org/10.3390/W16162283>
- Albertini, C., Gioia, A., Iacobellis, V., Manfreda, S., & Petropoulos, G. P. (2024). Exploring the use of random forest classifier with Sentinel-2 imagery in flooded area mapping. *Geographical Information Science: Case Studies in Earth and Environmental Monitoring, 521–542.* <https://doi.org/10.1016/B978-0-443-13605-4.00017-5>

- Al-Mukhtar, M., & Al-Yaseen, F. (2019a). Application of HEC-HMS Model for Flow Simulation in the Lake Tana Basin: The Case of Gilgel Abay Catchment, Upper Blue Nile Basin, Ethiopia. *Hydrology* 2019, Vol. 6, Page 21, 6(1), 21. <https://doi.org/10.3390/HYDROLOGY6010021>
- Al-Mukhtar, M., & Al-Yaseen, F. (2019b). Modeling water quality parameters using data-driven models, a case study Abu-Ziriq marsh in south of Iraq. *Hydrology*, 6(1). <https://doi.org/10.3390/hydrology6010021>
- Alves, P. B. R., Amanguah, E., McNally, D., Espinoza, M., Ghaedi, H., Reilly, A. C., & Hendricks, M. D. (2024). Navigating the definition of urban flooding: A conceptual and systematic review of the literature. *Water Science and Technology*, 90(10), 2796–2812. <https://doi.org/10.2166/WST.2024.351>
- Amitrano, D., Di Martino, G., Di Simone, A., & Imperatore, P. (2024). Flood Detection with SAR: A Review of Techniques and Datasets. In *Remote Sensing* (Vol. 16, Issue 4). Multidisciplinary Digital Publishing Institute (MDPI). <https://doi.org/10.3390/rs16040656>
- Annis, A., Nardi, F., Petroselli, A., Apollonio, C., Arcangeletti, E., Tauro, F., Belli, C., Bianconi, R., & Grimaldi, S. (2020a). UAV-DEM for Small-Scale Flood Hazard Mapping. *Water 2020*, Vol. 12, Page 1717, 12(6), 1717. <https://doi.org/10.3390/W12061717>
- Annis, A., Nardi, F., Petroselli, A., Apollonio, C., Arcangeletti, E., Tauro, F., Belli, C., Bianconi, R., & Grimaldi, S. (2020b). UAV-DEM for Small-Scale Flood Hazard Mapping. *Water 2020*, Vol. 12, Page 1717, 12(6), 1717. <https://doi.org/10.3390/W12061717>
- Arcement, G. J., & Schneider, V. R. (1989). *Guide for Selecting Manning's Roughness Coefficients for Natural Channels and Flood Plains*.
- Aryal, A., Bhatta, K. P., Adhikari, S., & Baral, H. (2022). Scrutinizing Urbanization in Kathmandu Using Google Earth Engine Together with Proximity-Based Scenario Modelling. *Land 2023*, Vol. 12, Page 25, 12(1), 25. <https://doi.org/10.3390/LAND12010025>
- Aryal, D., Wang, L., Adhikari, T. R., Zhou, J., Li, X., Shrestha, M., Wang, Y., & Chen, D. (2020). A model-based flood hazard mapping on the southern slope of Himalaya. *Water (Switzerland)*, 12(2). <https://doi.org/10.3390/w12020540>
- Aryal, K., & Regmi, M. (2022). *Proceedings of 11 th IOE Graduate Conference Flood Map Delineation of Narayani River Using HEC-RAS, HEC-GEORAS and ARC-GIS*.
- Asadi, A., & Boostani, F. (2013). Application of HEC-HMS for Flood Forecasting in Kabkian Basin and Delibajak Subbasin in Iran. *IOSR Journal of Engineering*, 3(9), 3–10. www.iosrjen.org
- Ata, F. M., Toriman, M. E., Desa, S. M., San, L. Y., & Kamarudin, M. K. A. (2023). DEVELOPMENT OF HYDROLOGICAL MODELLING USING HEC-HMS AND HEC-RAS FOR FLOOD HAZARD MAPPING AT JUNJUNG RIVER CATCHMENT. *Planning Malaysia*, 21(6), 116–129. <https://doi.org/10.21837/PM.V21I30.1390>
- Balta, B. B. (2024). *ANALYSIS OF FLOW, ROUGHNESS AND DOWNSTREAM BOUNDARY CONDITION UNCERTAINTIES WITHIN HEC-RAS 1-D MODELING A THESIS SUBMITTED TO THE GRADUATE SCHOOL OF NATURAL AND APPLIED SCIENCES OF MIDDLE EAST TECHNICAL UNIVERSITY*.

- Basnet, K., Baniya, U., & Karki, S. (2018). Comparative Study of Design Discharge Calculation Approaches, a Case study of Padhu Khola, Kaski, Nepal. <https://www.researchgate.net/publication/332548356>
- Belay, H., Melesse, A. M., Tegegne, G., & Kassaye, S. M. (2025). Flood Inundation Mapping Using the Google Earth Engine and HEC-RAS Under Land Use/Land Cover and Climate Changes in the Gumara Watershed, Upper Blue Nile Basin, Ethiopia. *Remote Sensing 2025, Vol. 17, Page 1283, 17(7), 1283.* <https://doi.org/10.3390/RS17071283>
- Ben Khélifa, W., & Mosbahi, M. (2022). Modeling of rainfall-runoff process using HEC-HMS model for an urban ungauged watershed in Tunisia. *Modeling Earth Systems and Environment, 8(2), 1749–1758.* <https://doi.org/10.1007/s40808-021-01177-6>
- Bennett, N. D., Croke, B. F. W., Guariso, G., Guillaume, J. H. A., Hamilton, S. H., Jakeman, A. J., Marsili-Libelli, S., Newham, L. T. H., Norton, J. P., Perrin, C., Pierce, S. A., Robson, B., Seppelt, R., Voinov, A. A., Fath, B. D., & Andreassian, V. (2013). Characterising performance of environmental models. *Environmental Modelling and Software, 40, 1–20.* <https://doi.org/10.1016/J.ENVSOFT.2012.09.011>
- Bhagat, N. (2017). Flood Frequency Analysis Using Gumbel's Distribution Method: A Case Study of Lower Mahi Basin, India. *Journal of Water Resources and Ocean Science, 6(4), 51.* <https://doi.org/10.11648/J.WROS.20170604.11>
- Bhargav, A., & R.Suresh. (2025). Exploring River's Flood Dynamics: Integrating HEC-RAS 1-D Modelling and Geospatial Techniques for the Karjan River in Gujarat's Narmada Basin, India. *International Journal of Environment and Climate Change, 15(1), 140–155.* <https://doi.org/10.9734/ijecc/2025/v15i14681>
- Bohara, B., Tamrakar, N. K., & Sharma, D. R. (2024). 1D-Flood Hazard Mapping and Analysis Using HEC-RAS Modelling, A case study of the Seti River, West Central Nepal. *International Journal of Latest Engineering and Management Research (IJLEMR), 9(8), 61–69.* <https://doi.org/10.56581/ijlemr.9.08.61-69>
- Brue, P. (2022). *HEC-RAS Boundary Conditions.* <https://www.paigebrue.com/hec-ras-boundary-conditions/>
- Cerri, M. (2017). Flood simulation using HEC-RAS model calibrated with remotely sensed water mask: a case study of Mulde River, Germany.
- Chaulagain, D., Ram Rimal, P., Ngando, S. N., Nsafon, B. E. K., Suh, D., & Huh, J. S. (2023a). Flood susceptibility mapping of Kathmandu metropolitan city using GIS-based multi-criteria decision analysis. *Ecological Indicators, 154, 110653.* <https://doi.org/10.1016/j.ecolind.2023.110653>
- Chaulagain, D., Ram Rimal, P., Ngando, S. N., Nsafon, B. E. K., Suh, D., & Huh, J. S. (2023b). Flood susceptibility mapping of Kathmandu metropolitan city using GIS-based multi-criteria decision analysis. *Ecological Indicators, 154.* <https://doi.org/10.1016/j.ecolind.2023.110653>
- Chow, V. Te. (1959). *Open Channel Hydraulics.* McGraw Hill, New York.
- Clasing, R., Muñoz, E., Arumí, J. L., & Parra, V. (2023). Remote Sensing with UAVs for Flood Modeling: A Validation with Actual Flood Records. *Water 2023, Vol. 15, Page 3813, 15(21), 3813.* <https://doi.org/10.3390/W15213813>

- Dahal, R. K. (2012). Rainfall-induced Landslides in Nepal. *International Journal of Erosion Control Engineering*, 5(1), 1–8. <https://doi.org/10.13101/IJECE.5.1>
- Danegulu, A., Karki, S., Bhattacharai, P. K., & Pandey, V. P. (2024). Characterizing urban flooding in the Kathmandu Valley, Nepal: the influence of urbanization and river encroachment. *Natural Hazards: Journal of the International Society for the Prevention and Mitigation of Natural Hazards*, 120(12), 10923–10947. <https://doi.org/10.1007/S11069-024-06650-W>
- Dangol, N. (2021). Flood Modeling Assessment: A Case of Bishnumati River. *Journal on Geoinformatics, Nepal*, 20(1), 31–37. <https://doi.org/10.3126/NJG.V20I1.39474>
- Dangol, S., & Bormudoi, A. (2015). Flood Hazard Mapping and Vulnerability Analysis of Bishnumati River, Nepal. *Journal on Geoinformatics, Nepal*, 14, 20–24. <https://doi.org/10.3126/NJG.V14I0.16969>
- Darji, K., Patel, D., Prakash, I., & Altuwajri, H. A. (2024). Hydrodynamic modeling of dam breach floods for predicting downstream inundation scenarios using integrated approach of satellite data, unmanned aerial vehicles (UAVs), and Google Earth Engine (GEE). *Applied Water Science*, 14(9). <https://doi.org/10.1007/S13201-024-02253-9>
- Dev Acharya, T., Banjara, S., & Deuja, S. (2011). *Flood Risk Mapping of Upper Bagmati Basin*. <https://doi.org/10.13140/RG.2.2.12449.10087>
- Diedhiou, R., Sambou, S., Kane, S., Leye, I., Diatta, S., Sane, M. L., & Ndione, D. M. (2020). Calibration of HEC-RAS Model for One Dimensional Steady Flow Analysis—A Case of Senegal River Estuary Downstream Diama Dam. *Open Journal of Modern Hydrology*, 10(03), 45–64. <https://doi.org/10.4236/OJMH.2020.103004>
- Dwivedi, P. D., Das, M., Kumar, S., & Verma, A. K. (2020). Safety assessment of food derived from genetically modified crops. *Animal Biotechnology: Models in Discovery and Translation*, 655–673. <https://doi.org/10.1016/B978-0-12-811710-1.00025-2>
- Farhadi, H., Ebadi, H., Kiani, A., & Asgary, A. (2024). Near Real-Time Flood Monitoring Using Multi-Sensor Optical Imagery and Machine Learning by GEE: An Automatic Feature-Based Multi-Class Classification Approach. *Remote Sensing 2024, Vol. 16, Page 4454*, 16(23), 4454. <https://doi.org/10.3390/RS16234454>
- Fasipe, O. A., & Izinyon, O. C. (2021). Exponent determination in a poorly gauged basin system in Nigeria based on flow characteristics investigation and regionalization method. *SN Applied Sciences*, 3(3), 1–20. <https://doi.org/10.1007/S42452-021-04302-3/FIGURES/8>
- Foroughnia, F., Alfieri, S. M., Menenti, M., & Lindenbergh, R. (2022). Evaluation of SAR and Optical Data for Flood Delineation Using Supervised and Unsupervised Classification. *Remote Sensing*, 14(15). <https://doi.org/10.3390/rs14153718>
- Gauchan, K. (2023). *Nepal's Flooding Challenges: Understanding the Struggle for Effective Mitigation*.
- Gebre, S. L. (2015). Application of the HEC-HMS Model for Runoff Simulation of Upper Blue Nile River Basin. *Journal of Waste Water Treatment & Analysis*, 06(02). <https://doi.org/10.4172/2157-7587.1000199>

- Gebre SL, G. Y. (2015). Flood Hazard Assessment and Mapping of Flood Inundation Area of the Awash River Basin in Ethiopia using GIS and HEC-GeoRAS/HEC-RAS Model. *Journal of Civil & Environmental Engineering*, 05(04). <https://doi.org/10.4172/2165-784X.1000179>
- Ghanbarpour, M. R., Salimi, S., Saravi, M. M., & Zarei, M. (2011). Calibration of River Hydraulic Model Combined with GIS Analysis using Ground-Based Observation Data. *Research Journal of Applied Sciences, Engineering and Technology*, 3(5), 456–463.
- Ghayour, L., Neshat, A., Paryani, S., Shahabi, H., Shirzadi, A., Chen, W., Al-Ansari, N., Geertsema, M., Amiri, M. P., Gholamnia, M., Dou, J., & Ahmad, A. (2021). Performance evaluation of sentinel-2 and landsat 8 OLI data for land cover/use classification using a comparison between machine learning algorithms. *Remote Sensing*, 13(7), 1349. <https://doi.org/10.3390/RS13071349/S1>
- Gholami, V. (2022). Prediction of flood discharge and flood flow depth using a hydraulic model and flood marks on the trees in ungauged forested watersheds. *Original Paper Journal of Forest Science*, 68(5), 190–198. <https://doi.org/10.17221/6/2022-JFS>
- Gill, M. A. (1978). Flood routing by the Muskingum method. *Journal of Hydrology*, 36(3–4), 353–363. [https://doi.org/10.1016/0022-1694\(78\)90153-1](https://doi.org/10.1016/0022-1694(78)90153-1)
- Gupta, H. V., Kling, H., Yilmaz, K. K., & Martinez, G. F. (2009). Decomposition of the mean squared error and NSE performance criteria: Implications for improving hydrological modelling. *Journal of Hydrology*, 377(1–2), 80–91. <https://doi.org/10.1016/J.JHYDROL.2009.08.003>
- Halwatura, D., & Najim, M. M. M. (2013). Application of the HEC-HMS model for runoff simulation in a tropical catchment. *Environmental Modelling and Software*, 46, 155–162. <https://doi.org/10.1016/j.envsoft.2013.03.006>
- Hejazi, N. (2023). *FIRM 2D: A New Methodology for Using HEC-RAS 2D Models in Flood Insurance Maps*. <https://www.floods.org/news-views/research-and-reports/firm-2d-a-new-methodology-for-using-hec-ras-2d-models-in-flood-insurance-maps/>
- Herbei, M. V., Bădăluță-Minda, C., Popescu, C. A., Horablagă, A., Dragomir, L. O., Popescu, G., Kader, S., & Sestrăs, P. (2024). Rainfall-runoff modeling based on HEC-HMS model: a case study in an area with increased groundwater discharge potential. *Frontiers in Water*, 6, 1474990. <https://doi.org/10.3389/FWATER.2024.1474990/TEXT>
- Hu, X., Wang, C., Zhu, D., & Li, D. (2025). *Harmonizing Sentinel-1/2 Imagery for Extreme Flood Mapping: Breaking Cloud and Historical Water Data Constraints*. <https://doi.org/10.2139/SSRN.5178733>
- Huang, M., & Jin, S. (2020). Rapid flood mapping and evaluation with a supervised classifier and change detection in Shouguang using Sentinel-1 SAR and Sentinel-2 optical data. *Remote Sensing*, 12(13). <https://doi.org/10.3390/rs12132073>
- Hutana, E., Mihu-Pintilie, A., Urzica, A., Paveluc, L. E., Stoleriu, C. C., & Grozavu, A. (2020a). Using 1D HEC-RAS Modeling and LiDAR Data to Improve Flood Hazard Maps Accuracy: A Case Study from Jijia Floodplain (NE Romania). *Water 2020*, Vol. 12, Page 1624, 12(6), 1624. <https://doi.org/10.3390/W12061624>
- Hutana, E., Mihu-Pintilie, A., Urzica, A., Paveluc, L. E., Stoleriu, C. C., & Grozavu, A. (2020b). Using 1D HEC-RAS modeling and LiDAR data to improve flood hazard maps accuracy: A case study from Jijia Floodplain (NE Romania). *Water (Switzerland)*, 12(6). <https://doi.org/10.3390/W12061624>

- ICIMOD. (2009). *National Disaster Preparedness*. <https://lib.icimod.org/records/ypj5g-kwd98>
- Iosub, M., Elena Chelariu, O., Marina, I., & Oana, H. (2015). *THE USE OF HEC-RAS MODELLING IN FLOOD RISK ANALYSIS*. https://doi.org/10.17378/AWC2015_42
- Jaafar, H. H., Ahmad, F. A., & El Beyrouthy, N. (2019). GCN250, new global gridded curve numbers for hydrologic modeling and design. *Scientific Data*, 6(1). <https://doi.org/10.1038/s41597-019-0155-x>
- Jean-François, P., Salamon, P., Belay, H., Melesse, A. M., Tegegne, G., & Molla Kassaye, S. (2025). Flood Inundation Mapping Using the Google Earth Engine and HEC-RAS Under Land Use/Land Cover and Climate Changes in the Gumara Watershed, Upper Blue Nile Basin, Ethiopia. *Remote Sensing 2025*, Vol. 17, Page 1283, 17(7), 1283. <https://doi.org/10.3390/RS17071283>
- Jung, Y., & Ma, Q. (2024). Enhancing Regulatory Flood Hazard Products Through HEC-RAS 2D: A Comparative Analysis with SWMM. *AECOM*. <https://icwmm.org/Archive/2024-C033-13/enhancing-regulatory-flood-hazard-products-through-hec-ras-2d-a-comparative-analysis-with-swmm>
- KC, S., Shrestha, S., Ninsawat, S., & Chonwattana, S. (2021). Predicting flood events in Kathmandu Metropolitan City under climate change and urbanisation. *Journal of Environmental Management*, 281, 111894. <https://doi.org/10.1016/J.JENVMAN.2020.111894>
- Khaddor, I., Achab, M., Rida, M., Sciensano, S., & Alaoui, A. H. (2017). Rainfall-Runoff calibration for semi-arid ungauged basins based on the cumulative observed hyetograph and SCS Storm model: Application to the Boukhalef watershed (Tangier, North We. In *Article in Journal of Materials and Environmental Sciences* (Vol. 8, Issue 10). <http://www.jmaterenvironsci.com/>
- Khan, I. R., Elmahdy, S. I., Rustum, R., Khan, Q., & Mohamed, M. M. (2024). Floods modeling and analysis for Dubai using HEC-HMS model and remote sensing using GIS. *Scientific Reports*, 14(1), 1–12. <https://doi.org/10.1038/S41598-024-74736-3;SUBJMETA=172,4111,704;KWRD=ENVIRONMENTAL+SCIENCES,NATURAL+HAZARDS>
- Kim, V., Tantanee, S., & Suparta, W. (2020). GIS-BASED FLOOD HAZARD MAPPING USING HEC-RAS MODEL: A CASE STUDY OF LOWER MEKONG RIVER, CAMBODIA. *Geographia Technica*, 15, 26. https://doi.org/10.21163/GT_2020.151.02
- Knebl, M. R., Yang, Z. L., Hutchison, K., & Maidment, D. R. (2005). Regional scale flood modeling using NEXRAD rainfall, GIS, and HEC-HMS/RAS: A case study for the San Antonio River Basin Summer 2002 storm event. *Journal of Environmental Management*, 75(4 SPEC. ISS.), 325–336. <https://doi.org/10.1016/J.JENVMAN.2004.11.024>,
- Konapala, G., Kumar, S. V, & Ahmad, S. K. (2021). *Exploring Sentinel-1 and Sentinel-2 diversity for Flood inundation mapping using deep learning*.
- Koneti, S., Sunkara, S. L., & Roy, P. S. (2018). Hydrological Modeling with Respect to Impact of Land-Use and Land-Cover Change on the Runoff Dynamics in Godavari River Basin Using the HEC-HMS Model. *ISPRS International Journal of Geo-Information* 2018, Vol. 7, Page 206, 7(6), 206. <https://doi.org/10.3390/IJGI7060206>
- Krause, P., Boyle, D. P., & Bäse, F. (2005). Comparison of different efficiency criteria for hydrological model assessment. *Advances in Geosciences*, 5, 89–97. <https://doi.org/10.5194/ADGEO-5-89-2005>,

- Kulkarni, A., & Kale, G. (2022). Identifying best combination of methodologies for event-based hydrological modeling using HEC-HMS software: a case study on the Panchganga River basin, India. *Sustainable Water Resources Management*, 8(4). <https://doi.org/10.1007/S40899-022-00691-4>
- Kumar, S., & Singh, K. K. (2021). Rain garden infiltration rate modeling using gradient boosting machine and deep learning techniques. *Water Science and Technology*, 84(9), 2366–2379. <https://doi.org/10.2166/WST.2021.444>
- Lad, A., & Shah, J. (2021). Flood Hazard Mapping and 1 D Hydraulic Module for Damanganga River, Valsad district, Gujarat, India. *International Journal of Civil Engineering*, 8(5), 45–51. <https://doi.org/10.14445/23488352/ijce-v8i5p105>
- Lamichhane, S., & Shakya, N. M. (2021). Land Use Land Cover (LULC) Change Projection in Kathmandu Valley using the CLUE-S Model. *Journal of Advanced College of Engineering and Management*, 6, 221–233. <https://doi.org/10.3126/JACEM.V6I0.38361>
- Li, Q., Peng, Y., Wang, G., Wang, H., Xue, B., & Hu, X. (2019). A combined method for estimating continuous runoff by parameter transfer and drainage area ratio method in ungauged catchments. *Water (Switzerland)*, 11(5). <https://doi.org/10.3390/w11051104>
- Li, Z., Xu, S., & Weng, Q. (2024). Beyond clouds: Seamless flood mapping using Harmonized Landsat and Sentinel-2 time series imagery and water occurrence data. *ISPRS Journal of Photogrammetry and Remote Sensing*, 216, 185–199. <https://doi.org/10.1016/J.ISPRSJPRS.2024.07.022>
- Malik, A., & Abdalla, R. (2016). Geospatial modeling of the impact of sea level rise on coastal communities: application of Richmond, British Columbia, Canada. *Modeling Earth Systems and Environment*, 2(3), 1–17. <https://doi.org/10.1007/S40808-016-0199-2/FIGURES/12>
- Malik, S., & Pal, S. C. (2021). Potential flood frequency analysis and susceptibility mapping using CMIP5 of MIROC5 and HEC-RAS model: a case study of lower Dwarkeswar River, Eastern India. *SN Applied Sciences*, 3(1). <https://doi.org/10.1007/s42452-020-04104-z>
- Malla, S. B., Dahal, R. K., & Hasegawa, S. (2020). Analyzing the disaster response competency of the local government official and the elected representative in Nepal. *Geoenvironmental Disasters*, 7(1). <https://doi.org/10.1186/S40677-020-00153-Z>
- Marina, I., & Oana, H. (2015). *THE USE OF HEC-RAS MODELLING IN FLOOD RISK ANALYSIS*.
- Martin, O., Rugumayo, A., & Ovcharovichova, J. (2012). *APPLICATION OF HEC HMS/RAS AND GIS TOOLS IN FLOOD MODELING: A CASE STUDY FOR RIVER SIRONKO-UGANDA*. 1(2), 19–31. <http://wwwrcamnl.wr.usgs.gov/sws/fieldmethods/Indirects/nvalues/index.htm>
- Minywach, L. T., Lohani, T. K., & Ayalew, A. T. (2024). Inundation Mapping and Flood Frequency Analysis using HEC-RAS Hydraulic Model and EasyFit Software. *Journal of Water Management Modeling*, 32. <https://doi.org/10.14796/JWMM.C513>
- MoHA. (2004). *Disaster Study and Research Section- Ministry of Home Affairs*. <https://moha.gov.np/en/office-layout/744>
- Mondal, A., Kundu, S., Chandniha, S. K., Shukla, R., & Mishra, P. K. (2012). Comparison of Support Vector Machine and Maximum Likelihood Classification Technique using Satellite Imagery. *Int Ernat Ional Journal of Rem Ot e Sensing and GIS*, 1, 116–123.

- Moriasi, D. N., Arnold, J. G., Liew, M. W. Van, Bingner, R. L., Harmel, R. D., & Veith, T. L. (1983). MODEL EVALUATION GUIDELINES FOR SYSTEMATIC QUANTIFICATION OF ACCURACY IN WATERSHED SIMULATIONS. *Transactions of the ASABE*, 50(3).
- Mustafa, A., Szydłowski, M., Veysipanah, M., & Hameed, H. M. (2023). GIS-based hydrodynamic modeling for urban flood mitigation in fast-growing regions: a case study of Erbil, Kurdistan Region of Iraq. *Scientific Reports* 2023 13:1, 13(1), 1–18. <https://doi.org/10.1038/s41598-023-36138-9>
- Nash, J. E., & Sutcliffe, J. V. (1970). River flow forecasting through conceptual models part I — A discussion of principles. *Journal of Hydrology*, 10(3), 282–290. [https://doi.org/10.1016/0022-1694\(70\)90255-6](https://doi.org/10.1016/0022-1694(70)90255-6)
- NDDRMA. (2024). *2024 September Floods and Landslides National Disaster Risk Reduction and Management Authority*. www.bipad.gov.np
- Nepal, P., Khanal, N. R., & Sharma, B. P. P. (2018). Policies and Institutions for Disaster Risk Management in Nepal: A Review. *Geographical Journal of Nepal*, 11, 1–24. <https://doi.org/10.3126/GJN.V11I0.19546>
- Niraula, S., & Shakya, N. M. (2020). Proceedings of 8 th IOE Graduate Conference Study on flood inundation mapping for Ratuwa River catchment using HECRAS 2D. *Month*, 8, 2350–8906. <https://earthexplorer.usgs.gov/>.
- Notti, D., Giordan, D., Calò, F., Pepe, A., Zucca, F., & Galve, J. P. (2019). Low-cost flood mapping using free satellite data from Sentinels constellation. *Geophysical Research Abstracts*, 21, 2019–14773.
- Oleyiblo, J. O., & Li, Z. J. (2010). Application of HEC-HMS for flood forecasting in Misai and Wan'an catchments in China. *Water Science and Engineering*, 3(1), 14–22. <https://doi.org/10.3882/J.ISSN.1674-2370.2010.01.002>
- Oucherif, A., & Benmamar, S. (2017). *FLOOD RISK MAPPING AND ANALYSIS OF THE M'ZAB VALLEY, ALGERIA*. <https://doi.org/10.2495/RBM170081>
- Palomba, G., Farasin, A., & Rossi, C. (2020). *Sentinel-1 Flood Delineation with Supervised Machine Learning* *Sentinel-1 Flood Delineation with Supervised Machine Learning*.
- Parhi, P. K. (2018a). Flood Management in Mahanadi Basin using HEC-RAS and Gumbel's Extreme Value Distribution. *Journal of The Institution of Engineers (India): Series A*, 99(4), 751–755. <https://doi.org/10.1007/S40030-018-0317-4>
- Parhi, P. K. (2018b). Flood Management in Mahanadi Basin using HEC-RAS and Gumbel's Extreme Value Distribution. *Journal of The Institution of Engineers (India): Series A*, 99(4), 751–755. <https://doi.org/10.1007/s40030-018-0317-4>
- Parizi, E., Khojeh, S., Hosseini, S. M., & Moghadam, Y. J. (2022a). Application of Unmanned Aerial Vehicle DEM in flood modeling and comparison with global DEMs: Case study of Atrak River Basin, Iran. *Journal of Environmental Management*, 317, 115492. <https://doi.org/10.1016/J.JENVMAN.2022.115492>
- Parizi, E., Khojeh, S., Hosseini, S. M., & Moghadam, Y. J. (2022b). Application of Unmanned Aerial Vehicle DEM in flood modeling and comparison with global DEMs: Case study of Atrak River Basin, Iran. *Journal of Environmental Management*, 317. <https://doi.org/10.1016/j.jenvman.2022.115492>

- Patel, D. P., & Srivastava, P. K. (2013). Flood Hazards Mitigation Analysis Using Remote Sensing and GIS: Correspondence with Town Planning Scheme. *Water Resources Management*, 27(7), 2353–2368. [https://doi.org/10.1007/S11269-013-0291-6/METRICS](https://doi.org/10.1007/S11269-013-0291-6)
- Pathan, A. I., & Agnihotri, P. G. (2019). A Combined Approach for 1-D Hydrodynamic Flood Modeling by using Arc-Gis, Hec-Georas, Hec-Ras Interface-A Case Study on Purna River of Navsari City, Gujarat. *International Journal of Recent Technology and Engineering (IJRTE)*, 8(1). www.ijrte.org
- Paudel, R. C., Basnet, K., & Sherchan, B. (2019). *Application of HEC-HMS Model for Runoff Simulation: A Case Study of Marshyangdi River Basin in Nepal*.
- Peker, İ. B., Gülbaz, S., Demir, V., Orhan, O., & Beden, N. (2024a). Integration of HEC-RAS and HEC-HMS with GIS in Flood Modeling and Flood Hazard Mapping. *Sustainability 2024*, Vol. 16, Page 1226, 16(3), 1226. <https://doi.org/10.3390/SU16031226>
- Peker, İ. B., Gülbaz, S., Demir, V., Orhan, O., & Beden, N. (2024b). Integration of HEC-RAS and HEC-HMS with GIS in Flood Modeling and Flood Hazard Mapping. *Sustainability 2024*, Vol. 16, Page 1226, 16(3), 1226. <https://doi.org/10.3390/SU16031226>
- Peker, İ. B., Gülbaz, S., Demir, V., Orhan, O., & Beden, N. (2024c). Integration of HEC-RAS and HEC-HMS with GIS in Flood Modeling and Flood Hazard Mapping. *Sustainability (Switzerland)*, 16(3). <https://doi.org/10.3390/SU16031226>
- Petropoulos, G. P., Georgiadi, A., & Kalogeropoulos, K. (2024). Leveraging Sentinel-2 and Geographical Information Systems in Mapping Flooded Regions around the Sesia River, Piedmont, Italy. *GeoHazards*, 5(2), 485–503. <https://doi.org/10.3390/geohazards5020025>
- Prafulkumar V., T., Prem Lal, P., & Prakash D., P. (2011). Calibration of HEC-RAS Model on Prediction of Flood for Lower Tapi River, India. *Journal of Water Resource and Protection*, 2011(11), 805–811. <https://doi.org/10.4236/JWARP.2011.311090>
- Psomiadis, E., Diakakis, M., & Soulis, K. X. (2020). Combining SAR and Optical Earth Observation with Hydraulic Simulation for Flood Mapping and Impact Assessment. *Remote Sensing 2020*, Vol. 12, Page 3980, 12(23), 3980. <https://doi.org/10.3390/RS12233980>
- Pushpalatha, R., Perrin, C., Moine, N. Le, & Andréassian, V. (2012). A review of efficiency criteria suitable for evaluating low-flow simulations. *Journal of Hydrology*, 420–421, 171–182. <https://doi.org/10.1016/J.JHYDROL.2011.11.055>
- Qaiser-Yuan. (2011). *Floodplain Modeling in the Kansas River Basin Using Hydrologic Engineering Center (HEC) Models Impacts of Urbanization and Wetlands for Mitigation R E S E A R C H A N D D E V E L O P M E N T*. www.epa.gov
- Rangari, V. A., Umamahesh, N. V., & Bhatt, C. M. (2019). Assessment of inundation risk in urban floods using HEC RAS 2D. *Modeling Earth Systems and Environment*, 5(4), 1839–1851. [https://doi.org/10.1007/S40808-019-00641-8/METRICS](https://doi.org/10.1007/S40808-019-00641-8)
- Richards, J. A. (2022). Remote sensing digital image analysis. *Remote Sensing Digital Image Analysis*, 1–567. [https://doi.org/10.1007/978-3-030-82327-6/COVER](https://doi.org/10.1007/978-3-030-82327-6)

- Ritter, A., & Muñoz-Carpena, R. (2013). Performance evaluation of hydrological models: Statistical significance for reducing subjectivity in goodness-of-fit assessments. *Journal of Hydrology*, 480, 33–45. <https://doi.org/10.1016/J.JHYDROL.2012.12.004>
- Sahu, S., Krishi, J. N., Vidyalaya, V., Jawaharlal, S. K. P., Krishi, N., Galkate, R. V., Pyasi, S. K., & Galkate, & R. V. (2020). A REVIEW ON THE HEC-HMS RAINFALL-RUNOFF SIMULATION MODEL. In *Article in International Journal of Agricultural Science and Research*. www.tjprc.org
- Salas, E. B. (2024). *Flood deaths per year worldwide 2023*| Statista. <https://www.statista.com/statistics/1293207/global-number-of-deaths-due-to-flood/>
- Saliya Sampath, D., Weerakoon, S. B., Sampath, D. S., & Herath, S. (2015). *HEC-HMS Model for Runoff Simulation in a Tropical Catchment with Intra-Basin Diversions Case Study of the Deduru Oya River Basin, Sri Lanka Bio-shield for Tsunami View project Climate change View project HEC-HMS Model for Runoff Simulation in a Tropical Catchment with Intra-Basin Diversions Case Study of the Deduru Oya River Basin, Sri Lanka*. XLVIII(01), 2015. <https://doi.org/10.4038/engineer.v48i1.6843>
- Shreevastav, B. B. (2019). Flood Scenario and its Risk Management, Policy, Practices in Nepal. *International Journal of Scientific & Engineering Research*, 10(4), 571–581. <https://doi.org/10.14299/IJSER.2019.04.07>
- Shreevastav, B. B., Tiwari, K. R., Mandal, R. A., & Singh, B. (2022). “Flood risk modeling in southern Bagmati corridor, Nepal” (a study from Sarlahi and Rautahat, Nepal). *Progress in Disaster Science*, 16. <https://doi.org/10.1016/J.PDISAS.2022.100260>
- Shrestha, A., Niraula, R. R., Kafle, K. R., Shrestha, A., Shrestha, A., Niraula, R. R., Kafle, K. R., & Shrestha, A. (2023). Multi Hazard Assessment and Vulnerability Mapping of Sindhupalchok District. *AGUFM*, 2023(83), NH43D-083. <https://ui.adsabs.harvard.edu/abs/2023AGUFMNH43D08.3S/abstract>
- Souley Tangam, I., Yonaba, R., Niang, D., Adamou, M. M., Keïta, A., & Karambiri, H. (2024). Daily Simulation of the Rainfall–Runoff Relationship in the Sirba River Basin in West Africa: Insights from the HEC-HMS Model. *Hydrology* 2024, Vol. 11, Page 34, 11(3), 34. <https://doi.org/10.3390/HYDROLOGY11030034>
- Tahmasbinejad, H., Feyzolahpour, M., Mumipour, M., & Zakerhoseini, F. (2015). *Rainfall-Runoff Simulation and Modeling of Karun River using HEC-RAS and HEC-HMS models, Izeh district, Iran*.
- Tarpanelli, A., Mondini, A. C., & Camici, S. (2022). *Effectiveness of Sentinel-1 and Sentinel-2 for Flood Detection Assessment in Europe*. <https://doi.org/10.5194/nhess-2022-63>
- Tavus, B., Kocaman, S., Nefeslioglu, H. A., & Gokceoglu, C. (2020). A fusion approach for flood mapping using sentinel-1 and sentinel-2 datasets. *International Archives of the Photogrammetry, Remote Sensing and Spatial Information Sciences - ISPRS Archives*, 43(B3), 641–648. <https://doi.org/10.5194/isprs-archives-XLIII-B3-2020-641-2020>
- Thakur, B., Parajuli, R., Kalra, A., Ahmad, S., & Gupta, R. (2017). Coupling HEC-RAS and HEC-HMS in Precipitation Runoff Modelling and Evaluating Flood Plain Inundation Map. *Civil and Environmental Engineering and Construction Faculty Research*, 240. https://digitalscholarship.unlv.edu/fac_articles/450

- Thapa, P., Manandhar, S., Poudel, S., Shrestha, S., Tamang, S. P., Shrestha, R., & Devkota, N. (2024). Flood Modelling of Madi River Using HEC-RAS by Rain on Grid Approach. In *KEC Journal of Science and Engineering* (Vol. 8, Issue 1). <https://doi.org/10.1016/J.PROENG.2012.01.1233>
- Tingsanchali, T. (2012). Urban flood disaster management. *Procedia Engineering*, 32, 25–37. <https://doi.org/10.1016/J.PROENG.2012.01.1233>
- UN-SPIDER. (2010). *Step-by-Step: Flood Hazard Assessment | UN-SPIDER Knowledge Portal*. <https://www.un-spider.org/advisory-support/recommended-practices/recommended-practice-flood-hazard-assessment/step-by-step>
- Upadhyaya, B. R., Gajurel, A. P., Thapa, P. B., Bhattacharai, R. R., & Dhital, M. R. (2023). Flood hazard modelling using HEC-RAS in the Pathariya Khola, Far-western Nepal. *Journal of Nepal Geological Society*, 66, 119–130. <https://doi.org/10.3126/JNGS.V66I01.57957>
- USDA NRCS. (2004). *Hydrology National Engineering Handbook*.
- Vashist, K., & Singh, K. K. (2023). HEC-RAS 2D modeling for flood inundation mapping: a case study of the Krishna River Basin. *Water Practice and Technology*, 18(4), 831–844. <https://doi.org/10.2166/wpt.2023.048>
- Wang, W., Ma, M., Feng, Z., Yu, X., & Zhang, J. (2023). The Application and Applicability of HEC-HMS Model in Flood Simulation under the Condition of River Basin Urbanization. *Water 2023, Vol. 15, Page 2249*, 15(12), 2249. <https://doi.org/10.3390/W15122249>
- Wang, X., Liu, T., Shang, S., Yang, D., & Melesse, A. M. (2010). Estimation of design discharge for an ungauged overflow-receiving watershed using one-dimensional hydrodynamic model. *Intl. J. River Basin Management*, 8(1), 79–92. <https://doi.org/10.1080/15715121003714886>
- Watson, C. S., Gyawali, J., Creed, M., & Elliott, J. R. (2024). *Geocarto International ISSN: (Print) (Online) Journal homepage: www.tandfonline.com/journals/tgei20 City-scale high-resolution flood models and the role of topographic data: a case study of Kathmandu, Nepal City-scale high-resolution flood models and the role of topographic data: a case study of Kathmandu, Nepal*. <https://doi.org/10.1080/10106049.2024.2387073>
- Woodward, D. E., Hawkins, R. H., Jiang, R., Hjelmfelt, A. T., Van Mullem, J. A., & Quan, Q. D. (2003). Runoff Curve Number Method: Examination of the Initial Abstraction Ratio. *World Water and Environmental Resources Congress*, 1–10. [https://doi.org/10.1061/40685\(2003\)308](https://doi.org/10.1061/40685(2003)308)
- Wyżga, B., Radecki-Pawlak, A., Galia, T., Plesiński, K., Škarpich, V., & Dušek, R. (2020). Use of high-water marks and effective discharge calculation to optimize the height of bank revetments in an incised river channel. *Geomorphology*, 356. <https://doi.org/10.1016/J.GEOMORPH.2020.107098>
- Yang, S., Wang, P., Lou, H., Wang, J., Zhao, C., & Gong, T. (2019). Estimating river discharges in ungauged catchments using the slope-area method and unmanned aerial vehicle. *Water (Switzerland)*, 11(11). <https://doi.org/10.3390/w11112361>
- Zainalfikry, M. K., Ab Ghani, A., Zakaria, N. A., & Chan, N. W. (2020a). HEC-RAS One-Dimensional Hydrodynamic Modelling for Recent Major Flood Events in Pahang River. *Lecture Notes in Civil Engineering*, 53, 1099–1115. https://doi.org/10.1007/978-3-030-32816-0_83

Zainalfikry, M. K., Ab Ghani, A., Zakaria, N. A., & Chan, N. W. (2020b). HEC-RAS One-Dimensional Hydrodynamic Modelling for Recent Major Flood Events in Pahang River. *Lecture Notes in Civil Engineering*, 53, 1099–1115. https://doi.org/10.1007/978-3-030-32816-0_83

Zum Zwecke, A., Chini, M., Matgen, P., Hostache, R., Zhao, J., & Sc, M. (2005). *Large-scale flood mapping using microwave remote sensing data.*

10 ANNEX

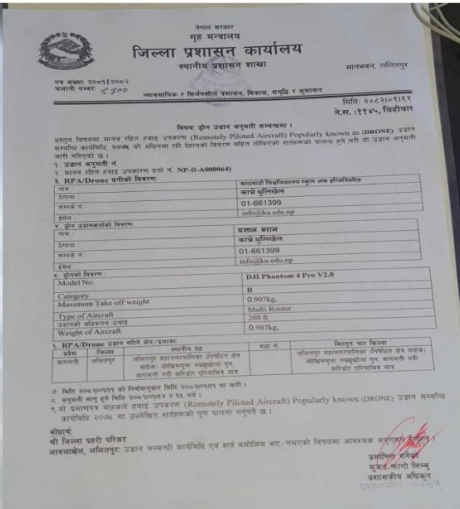
ANNEX 1



Conducting Drone Flight in Study Area



Drone Flight Permission



Drone Flight Permission

ANNEX 2



Reference Flood Image of Sep 27 from Locals

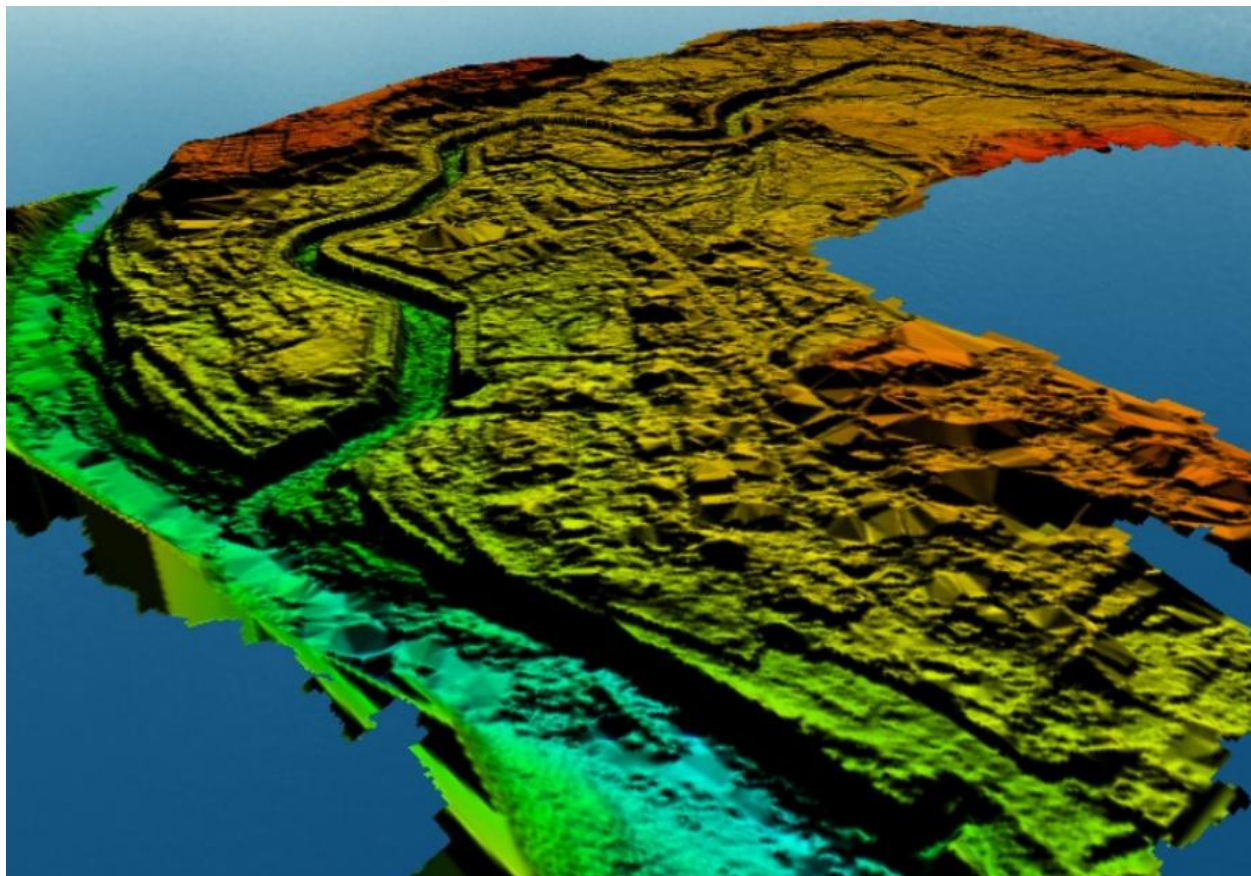


Getting Flood Validation Markers Using RTK GNSS



Setting Up Base for RTK Survey

ANNEX 3



DEM of Study Area

ANNEX 4

Points nakku							
FID	Shape *	Name	Code	Easting	Northing	Elevation	Desc
0	Point ZM	N_FM_6		333137.757	3060803.307	1232.891	Nakkhu HFL
1	Point ZM	N_FM_7		333137.748	3060803.358	1232.041	Nakkhu HFL
2	Point ZM	N_FM_8		333200.329	3060522.413	1232.938	Nakkhu HFL
3	Point ZM	N_FM_9		333372.601	3060296.979	1232.441	Nakkhu HFL
4	Point ZM	N_FM_10		333550.549	3060155.664	1232.001	Nakkhu HFL
5	Point ZM	N_FM_11		333544.733	3059671.386	1232.538	Nakkhu HFL
6	Point ZM	N_FM_12		333737.284	3059376.503	1232.976	Nakkhu HFL
7	Point ZM	N_FM_13		333449.498	3059152.636	1232.458	Nakkhu HFL
8	Point ZM	N_FM_14		333484.753	3058730.665	1232.793	Nakkhu HFL
9	Point ZM	N_FM_15		333289.652	3058437.121	1232.221	Nakkhu HFL

Attribute Data of Sample High Flood Level Points

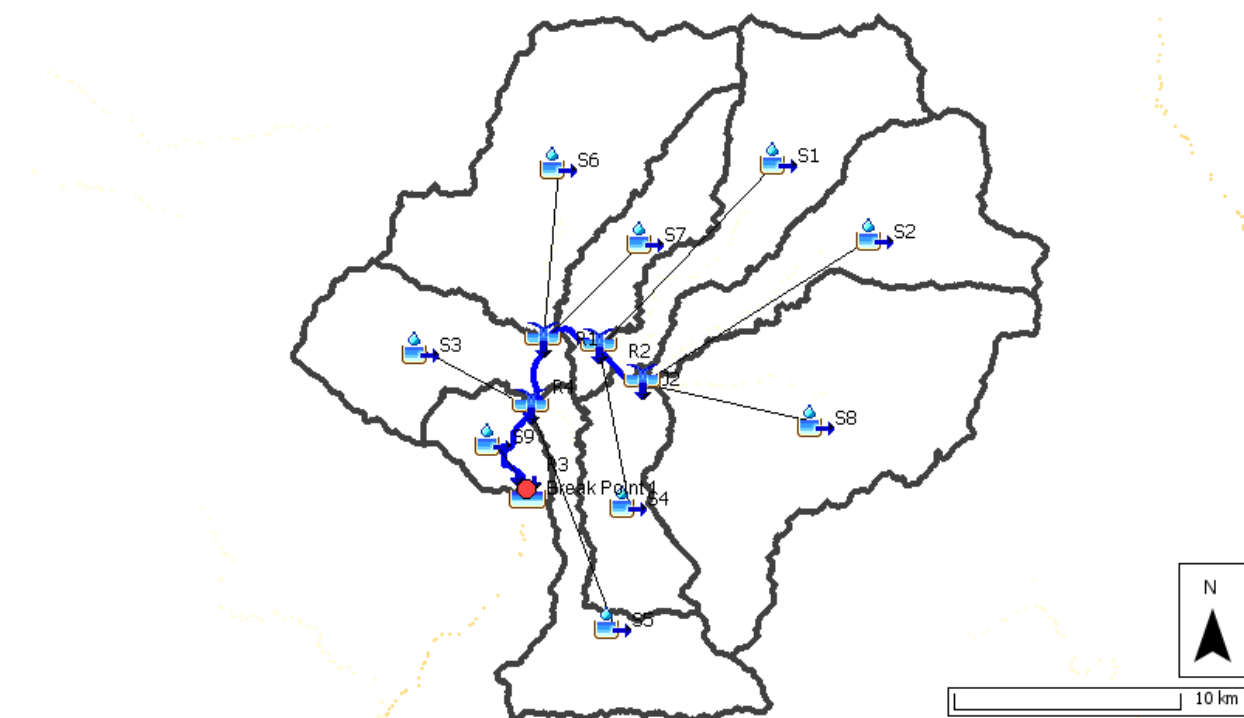
ANNEX 5

Table

	FID	Shape *	Name	Code	Easting	Northing	Elevation	Desc
	0	Point ZM	N_FM_4		331998.243	3060741.141	1212.460	GTP
	1	Point ZM	B_GS_1		332014.170	3060802.722	1210.338	GTP
	2	Point ZM	B_ST_1		332037.354	3060809.826	1211.942	GTP
	3	Point ZM	B_FM_2		332091.670	3060816.607	1217.750	GTP
	4	Point ZM	B_FM_3		332113.897	3061015.068	1218.042	GTP
	5	Point ZM	N_FM_1		332156.670	3061209.202	1218.525	GTP
	6	Point ZM	N_FM_2		332063.202	3061173.720	1213.954	GTP
	7	Point ZM	N_ST_2		332045.499	3061149.796	1214.264	GTP
	8	Point ZM	N_ST_1		332046.563	3061158.297	1214.358	GTP
	9	Point ZM	CN_NB_1		331971.682	3061058.445	1208.544	GTP
	10	Point ZM	E_N_1		332060.776	3061102.593	1213.511	GTP
	11	Point ZM	D_N_1		332080.083	3061126.232	1261.846	GTP

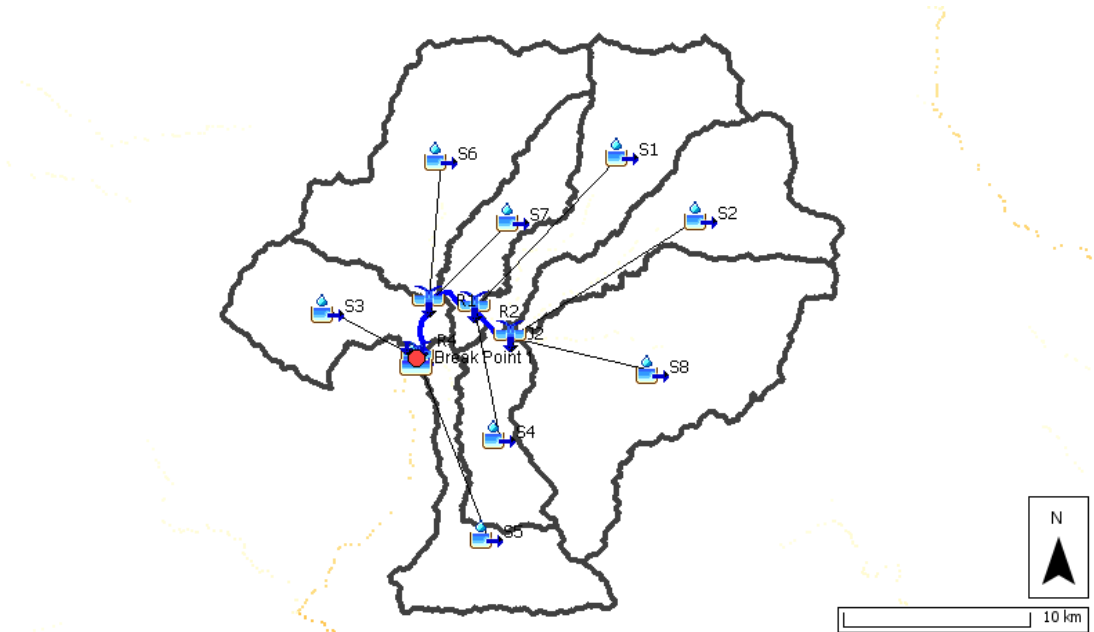
Attribute Data of Sample Ground Truth Points

ANNEX 6



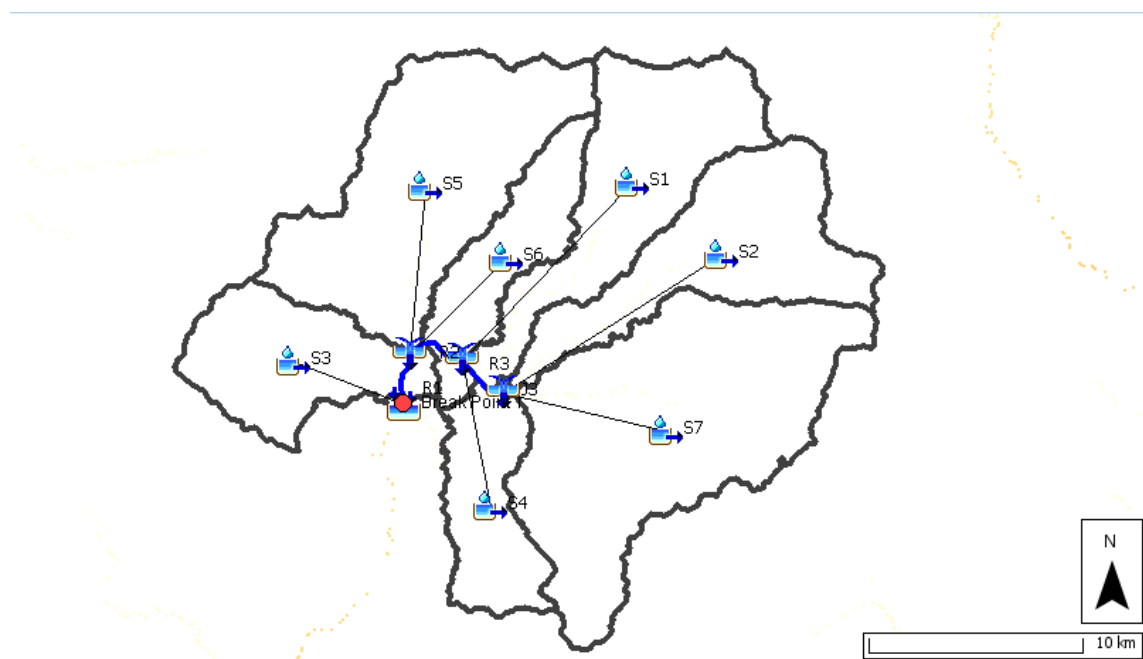
Catchment Area of Bagmati River at Khokana Station

ANNEX 7



Catchment Area of Bagmati River (Confluence Downstream Point)

ANNEX 8



Catchment Area of Bagmati River (Confluence Upstream Point)

